ALMA MATER STUDIORUM

UNIVERSITÀ DI BOLOGNA

DOTTORATO DI RICERCA IN

ASTROFISICA

Ciclo XXXIV

UNVEILING THE UNKNOWN OF COOL STARS WITH HIGH-RESOLUTION SPECTROSCOPY

Presentata da: **Cristiano Fanelli**

Coordinatore Dottorato: Supervisore:

Chiar.mo Prof. **A. Miglio**   Dr. **L. Origlia**

Co-supervisori:

Chiar.mo Prof. **A. Mucciarelli**

Dr. **D. Romano**

Esame finale anno 2022

Questo lavoro è frutto non solo di studio e di fatica individuale,
ma di collaborazioni ed interazioni con tante persone,
dentro e fuori l'ambito accademico.
A tutti e tutte voi, Grazie.

I'd like to share a revelation that I've had during my time here. It came to me when I tried to classify your species and I realized that you're not actually mammals. Every mammal on this planet instinctively develops a natural equilibrium with the surrounding environment but you humans do not. You move to an area and you multiply and multiply until every natural resource is consumed and the only way you can survive is to spread to another area. There is another organism on this planet that follows the same pattern. Do you know what it is? A virus. Human beings are a disease, a cancer of this planet. You're a plague and we are the cure.

Agent Smith, The Matrix

Abstract

Cool giant and supergiant stars are among the brightest populations in any stellar system and they are easily observable out to large distances, especially at infrared wavelengths. These stars also dominate the integrated light of star clusters in a wide range of ages, making them powerful tracers of stellar populations in more distant galaxies.

High-resolution near-IR spectroscopy is a key tool for quantitatively investigating their kinematic, evolutionary and chemical properties. However, the systematic exploration and calibration of the NIR spectral diagnostics to study these cool stellar populations based on high-resolution spectroscopy is still in its pioneering stage. Any effort to make progress in the field is innovative and of impact on stellar archaeology and stellar evolution.

This PhD project takes the challenge of exploring that new parameter space and characterizing the physical properties, the chemical content and the kinematics of cool giants and supergiants in selected disc fields and clusters of our Galaxy, with the ultimate goal of tracing their past and recent star formation and chemical enrichment history. By using optical HARPS-N and near-infrared GIANO-B high-resolution stellar spectra in the context of the large program *SPA-Stellar Population Astrophysics: the detailed, age-resolved chemistry of the Milky Way disk"* (PI L. Origlia), an extensive study of Arcturus, a standard calibrator for red giant stars, has been performed. New diagnostics of stellar parameters as well as optimal linelists for chemical analysis have been provided.

Then, such diagnostics have been used to determine evolutionary properties, detailed chemical abundances of almost 30 different elements and mixing processes of a homogeneous sample of red supergiant stars in the Perseus complex.

Contents

Chapter *1*

Introduction

The Ph.D. project titled *FRONTIERA: High resolution spectroscopy of stellar populations in the era of extreme large telescopes* fits into the broad contest of studying the formation and evolution of stellar systems and their hosts, providing new, original tools for an exhaustive physical, chemical and kinematic characterization of cool stars and stellar populations, in a critical but poorly explored space of physical and environmental parameters.

This Ph.D. project has been funded by the *Premiale FRONTIERA* (Fostering high ResolutiON Technology and Innovation for Exoplanets and Research in Astrophysics, PI I. Pagano), an INAF strategic project funded by the Italian Ministry of Education, Universities and Research (MIUR), and aimed at maintaining and consolidating the the Italian scientific and technological excellence in the domain of high spectral and spatial resolution, in collaboration with national and international universities, including the Department of Physics and Astronomy of Bologna, as well as in training students and young researchers.

This Ph.D. project has been also granted a *Marco Polo* fellowship to spend a period of three months (reduced to two months because of the pandemic, October and November 2021) at the Observatoire de la Cote d'Azur in Nice, under the supervision of Prof. M. Schultheis, and contribute to the preparatory work for the upcoming spectroscopic VLT-MOONS Galactic survey of the cool stellar populations in the inner Galaxy and its satellites.

C. Fanelli has been also visiting astronomer at the Telescopio Nazionale Galileo (TNG) for an observing run of 8 nights in July 2019 within the large program *SPA-*

Stellar Population Astrophysics: the detailed, age-resolved chemistry of the Milky Way disk" (PI:Origlia), during which GIANO-B high-resolution YJHK spectra of red supergiants, carbon-enhanced, metal-poor giants (CEMP) and magnetic Ap stars have been acquired.

1.1   The astrophysical context

Red giants and supergiants are luminous, cool stars, tracing the latest stages of stellar evolution for a wide range of masses, from about 1 to 40 Solar masses. Hence, they also trace stellar populations over a wide range of ages, from a few million years when massive stars evolve as red supergiants (RSG), to the oldest ages in the Universe when low mass stars evolve as red giants (RG).

These luminous, evolved stars are observed in any galactic component and environment, hence they also probe stellar populations over the full range of ages and metallicities and out to large distances, dominating the integrated stellar luminosity of their host galaxies.

Spectroscopic studies are crucial to constrain chemistry and line-of-sight kinematics of stellar populations. The coupling of chemical and kinematic information is fundamental to disentangle sub-structures and constrain formation and evolution scenarios in complex stellar systems as galaxies are, including the Milky Way.

Different chemical elements are synthesized in stars with different mass progenitors and thus released to the interstellar medium with different time delays with respect to the onset of the star formation event. Hence the measurement of suitable chemical abundances and abundance ratios in statistical significant samples of stars can be efficiently used for quantitative studies of stellar nucleosynthesis and to constrain modes and timescales of formation and chemical enrichment of the host stellar systems. Observations at very high spectral resolution and signal-to-noise can also constrain stellar 3D structure, mixing processes in the stellar interiors, surface activity, stellar magnetic fields, winds, and mass loss.

Systematic ground-based spectroscopic studies at medium-high resolution in the optical spectral range of warm, intermediate-old giants in the Milky Way halo/disc and in the associated star clusters are routinely performed. These studies are crucial to reconstruct the early history of galaxy formation and evolution. However, in order to probe the most recent events of star formation and chemical enrichment in the galaxy disc, quantitative spectroscopy and chemical abundance analysis of younger and cooler giant and supergiant stars is needed. This is a quite recent field of investigation, on the learning curve, and it presents challenges over a wide

parameter space.

Observationally, red/IR spectroscopy is often needed because of the intrinsic low temperatures of these stars and the likely high reddening of their environments, if for example located in the inner disk/bulge and/or in star-forming regions. Also high spectral resolution and simultaneously wide spectral coverage are highly desirable for a complete line diagnostics and an exhaustive screening of their surface chemical abundances.

From the spectral modeling perspective, spectral and chemical abundance analysis of cool giants and supergiants require state-of-the-art model atmospheres, linelists and molecular chemistry to properly account for line and continuum opacity as well as to compute reliable molecular equilibria.

Finally, a lot of understanding of the physics, nucleosynthesis and overall late evolution of massive stars is still missed, in particular in the RSG stage. RSGs are evolved stars with masses ranging from 9 to 40 $M_\odot$. They are very luminous, characterized by $\approx 10^{4-5}$ $L_\odot$ (Humphreys & Davidson, 1979) and late spectral types (K and M), with typical temperatures between 3500 and 4500 K. RSGs are also very important as they are the progenitors of type II supernova (Groh et al., 2013; Smartt, 2015). The RSG evolutionary phase is quite rapid and mostly characterized by He-core burning at temperatures close to the Hayashi limit (Levesque, 2010). The modeling of the RSG phase is very complex and it depends on the assumed molecular opacities, geometry of the atmospheres and on the used recipes for the treatment of convection, mass loss, etc. as a function of the stellar mass and metallicity. A good treatment of convection is necessary, but it is still out of reach of 1D stellar-evolution codes (Ekström et al., 2012). Also the modelling of mass loss, is very challenging and modality and rates are still quite debated in the literature. For example, it is unclear whether the mass loss occurs continuously and regularly (Mauron & Josselin, 2011) or in episodic bursts (Humphreys et al., 2005; Moriya et al., 2011; Smith et al., 2009).

In the last few years, a new generation of medium-high resolution spectrographs working in the near-infrared (NIR) spectral range has been developed by consortia involving Italian researchers. Some of these instruments are already available (e.g. TNG-GIANO-B and VLT-CRIRES+), other facilities will be available in the next years (e.g. VLT-MOONS, ELT-ANDES). These new IR spectrographs are ideal to study the physics, chemistry and kinematics of intrinsically red (i.e. cool) and/or reddened (by dust extinction) giant and supergiant stars in galaxy fields as well as in star clusters.

1.2   The Ph.D. project outline

The systematic exploration and calibration of the NIR spectral diagnostics to study cool stellar populations, based on quantitative, high resolution spectroscopy is still in its pioneering stage. Any effort to make progress in the field is innovative and of impact for stellar archaeology.

This PhD project takes the challenge of exploring this new parameter space and characterizing the physical properties, the chemical content and the kinematics of cool giants and young red supergiants in selected disc fields and clusters of our Galaxy, with the ultimate goal of tracing their past and recent star formation and chemical enrichment history.

The project makes use of high resolution spectra acquired with the TNG GIANO-B (Oliva et al., 2012a,b; Origlia et al., 2014) NIR spectrograph, and occasionally, when reddening was not too severe, also simultaneously with the HARPS-N (Cosentino et al., 2014) optical spectrograph, in the context of the SPA large program, during several runs between 2018 and 2021. Observations and data reduction are described in Chapter 2, while spectral and chemical abundance analysis are described in Chapter 3.

Complementary photometric, astrometric and kinematic information from Gaia early data release 3 (EDR3) (Gaia Collaboration et al., 2021) and 2MASS (Skrutskie et al., 2006) and suitable evolutionary models have been used to derive stellar ages, luminosities, distances and proper motions.

This Ph.D. project allows to do many tests on the poorly studied parameter space of echelle high-resolution NIR spectra, as well as Optical spectra, by developing optimized numerical codes: some of these are published on my `GitHub` website[*], others will be published soon. The main scientific results obtained within this Ph.D. project are described in Chapters 4, and 5 and can be summarized as follows.

1) The identification and calibration of the main atomic and molecular lines to be used for the determination of the photospheric parameters (temperature, gravity, microturbulence and other velocity broadening) and chemical abundances in the NIR high resolution spectra of the Arcturus standard star, already extensively studied with optical spectroscopy. Within this activity, all the necessary software tools for data reduction, spectral synthesis and chemical analysis have been implemented, different codes and model atmospheres for the spectral synthesis, have been widely tested and the results have been compared with those obtained from optical spectra. The spectral analysis of Arcturus and the obtained results are detailed in

---

[*]https://github.com/CrisWat

Chapter 4 and published in the refereed paper:

Stellar population astrophysics (SPA) with the TNG. The Arcturus Lab, by **C. Fanelli**, L. Origlia, E. Oliva, A. Mucciarelli, N. Sanna, E. Dalessandro, and D. Romano; 2021, A&A.

2) exploiting such a diagnostics and suitable high resolution spectra obtained at the TNG to determine accurate line-of-sight kinematics, stellar parameters and chemical abundances of Galactic cool giants and supergiants stars in star clusters and associations, thus probing formation, evolution and chemical enrichment of their host.

In particular, the kinematic and chemical study of the young stellar populations in the Perseus complex is detailed in Chapter 5 and published in the following refereed papers:

First Phase Space Portrait of a Hierarchical Stellar Structure in the Milky Way, by E. Dalessandro , A. L. Varri, M. Tiongco, E. Vesperini, **C. Fanelli**, A. Mucciarelli, L. Origlia, M. Bellazzini, S. Saracino, E. Oliva, N. Sanna, M. Fabrizio, and A. Livernois; 2021, ApJ.

Stellar population astrophysics (SPA) with the TNG – The chemical content of the red supergiant population in the Perseus complex, by **C. Fanelli**, L. Origlia, E. Oliva, E. Dalessandro, A. Mucciarelli and N. Sanna; 2022, A&A.

The ePoster *High resolution IR spectroscopy of red supergiants: tracing Galactic young cluster formation and early evolution* by C. Fanelli has been presented at the online EAS 2021 conference in the SS33 session entitled *Star clusters to the next scale: reading the Local and high-z Universe with new giant eyes.*

Stellar population astrophysics (SPA) with the TNG – Lithium detection in red supergiant stars of the Perseus complex, by **C. Fanelli**, L. Origlia, A. Mucciarelli, N. Sanna, E. Oliva and E. Dalessandro (accepted for publication, in press, ApJ.)

During the Marco Polo fellowship at the Observatoire de la Cote d'Azur in Nice (Chapter 6), several simulations have been run for the optimal allocation of the one thousand MOONS fibers to stellar targets in the nuclear star cluster and in the molecular zone, an environment poorly explored so far, because of the huge stellar density and reddening and the lack of efficient multi-object spectrographs with

medium-high resolution capabilities in the NIR. Optimal linelists for the chemical analysis of MOONS spectra in the various grating/resolution configurations have been also compiled, starting from those obtained from the *Arcturus Lab* work. Finally, concluding remarks are reported in Chapter 7.

High-resolution echelle spectroscopy at the TNG

The TNG provides a formidable high resolution spectroscopic capability with the unique combination of HARPS-N and GIANO-B echelle spectrographs, covering the full optical and near IR range out to the K band. The HARPS-N spectrograph (Cosentino et al., 2014) covers the $378 - 691$ nm optical spectral range at a resolution R~115,000, while the GIANO-B spectrograph (Oliva et al., 2012a,b; Origlia et al., 2014) covers the $950 - 2450$ nm near IR spectral range at a resolution R~ $50,000$.

2.1 Observation of Arcturus

Arcturus is an ultra-bright target, thus, its observation with medium-large telescopes may request ad-hoc instrument setups to avoid saturation of the detector and the consequent loss of astrophysical information.

Arcturus was observed on July, 2th, 2018, with GIANO-B. Spectra were collected by using a gray filter, that attenuates the light by about 5 magnitudes. Nodding was used to optimise the subtraction of the background and other detector patterns: we collected several pairs of exposures with the star alternatively positioned at 1/4 (position A) and 3/4 (position B) of the slit length. The integration time was 60 seconds per A,B position, with a mean seeing of ~ 0.7".

The GIANO-B spectra can be reduced using the data reduction pipeline software GOFIO (Rainer et al., 2018), which processes calibration (darks, flats, and U-Ne

lamps taken in daytime) and scientific frames. The main feature of GOFIO is the optimal spectral extraction and wavelength calibration based on a physical model of the spectrometer that accurately matches instrumental effects such as variable slit tilt and order curvature over the echellogram (Oliva et al., 2018). The data reduction package also includes bad pixel and cosmic removal, sky and dark subtraction, flat-field and blaze correction. Arcturus spectrum was corrected for telluric absorption using the spectra of an O-type standard star taken at different air masses during the same night. The normalised spectra of the telluric standard taken at low and high air-mass values are combined with different weights to match the depth of the telluric lines in the target spectra.

The spectral regions with telluric transmission lower than 90% were normally excluded from the analysis, and the few intrinsic features of the O-stars used as telluric standards are broad lines of H and He that are easily recognizable and corrected using a Voigt fit. Fig. 2.1, 2.2, 2.3 and 2.4 show the rest-frame, normalised spectra corrected for telluric absorption. The average signal-to-noise ratio of the reduced and telluric-corrected spectrum is about 150 per pixel.

We also analysed two optical spectra of Arcturus retrieved by the ESO archive, in order to cross-check chemical abundances over the widest possible spectral range. These optical spectra were collected with the high-resolution spectrograph UVES at the ESO-VLT, at a resolution of R$\sim$ 80000, using the CD3 Red Arm 580 and CD4 Red Arm 860, that cover the 4800 - 6800 Å and 6700 - 10400 Å wavelengths ranges, respectively.
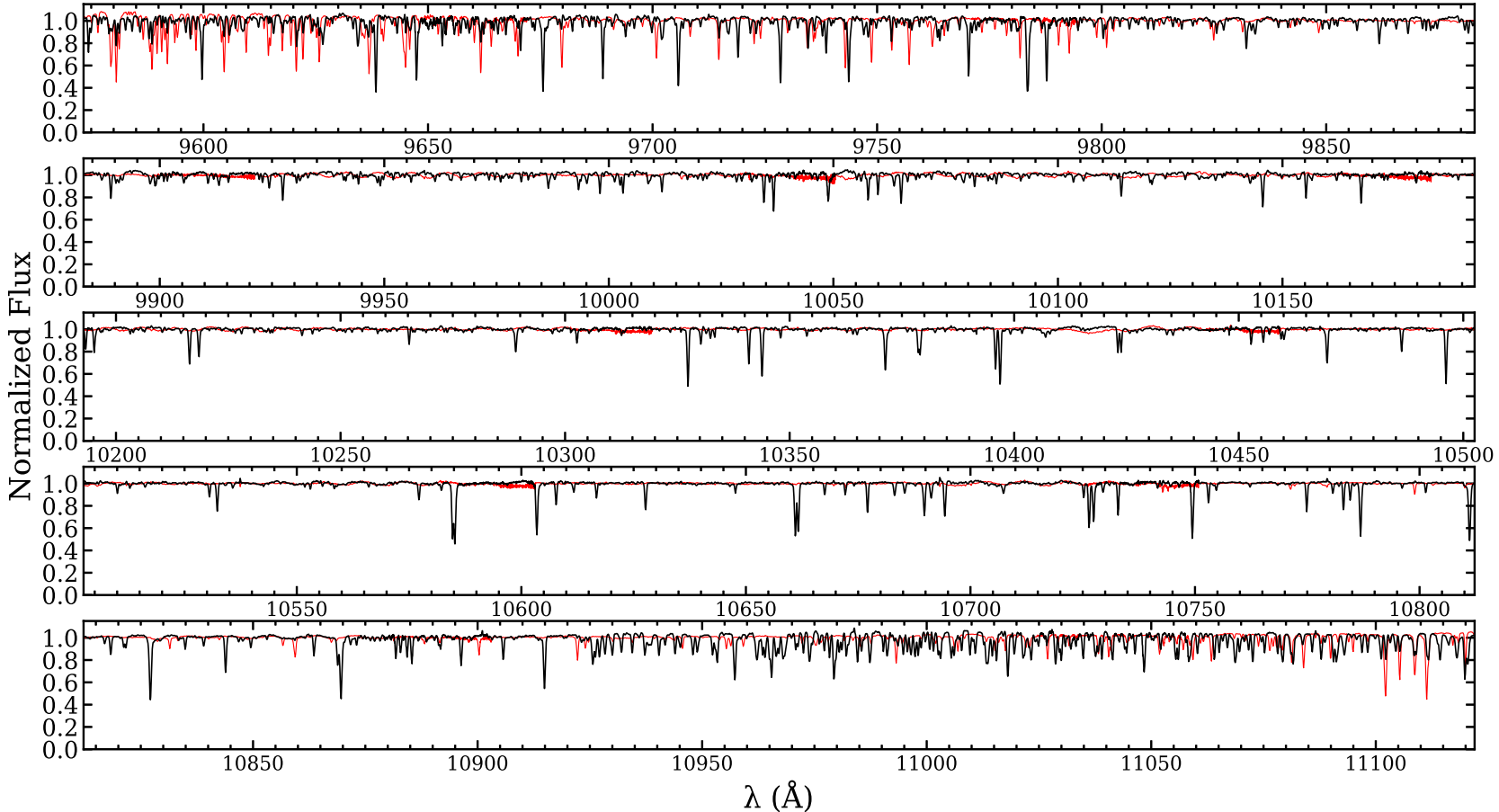
Figure 2.1: Observed Y-band Arcturus spectrum (black line) with the telluric correction (red line)
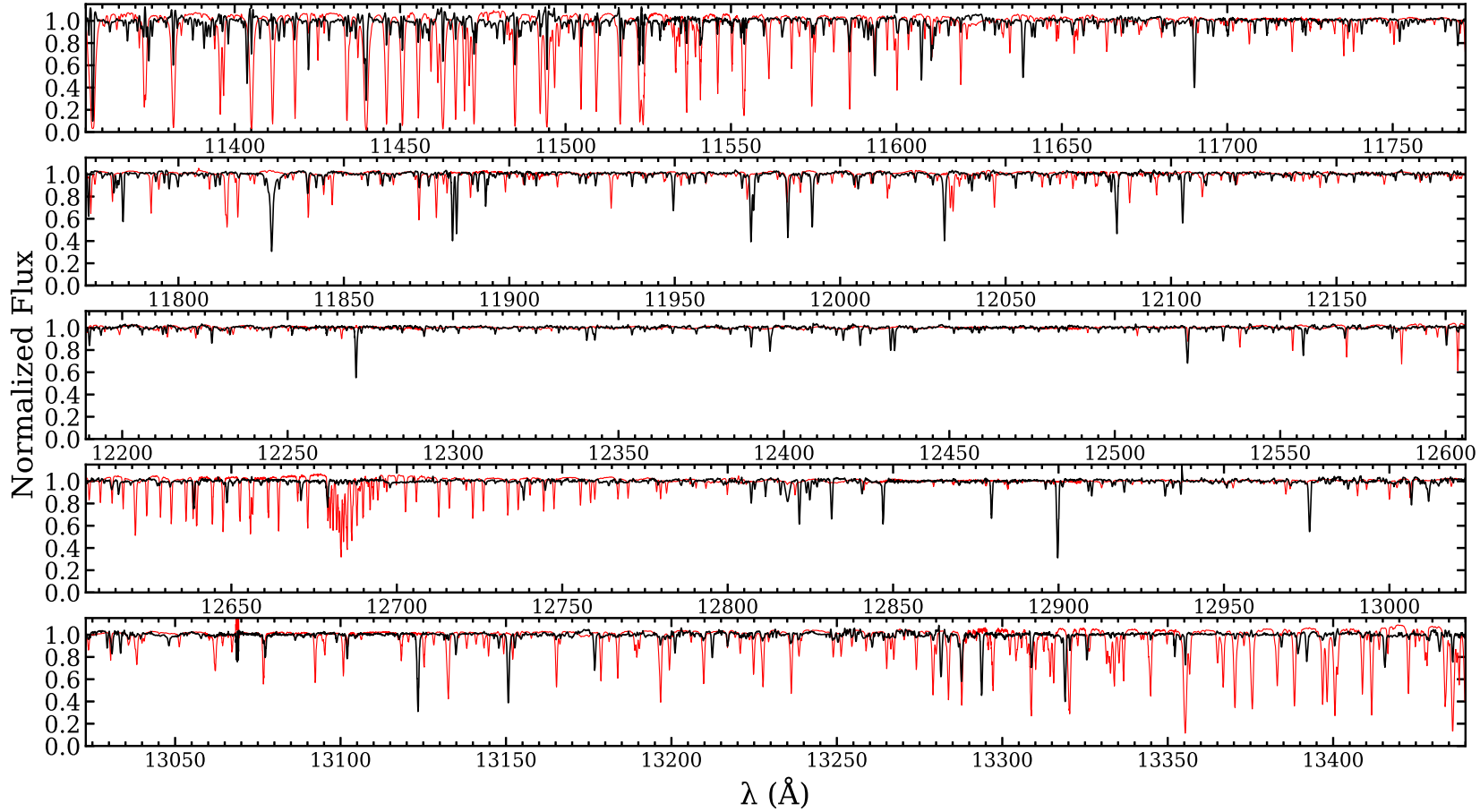
Figure 2.2: Observed J-band Arcturus spectrum (black line) with the telluric correction (red line)
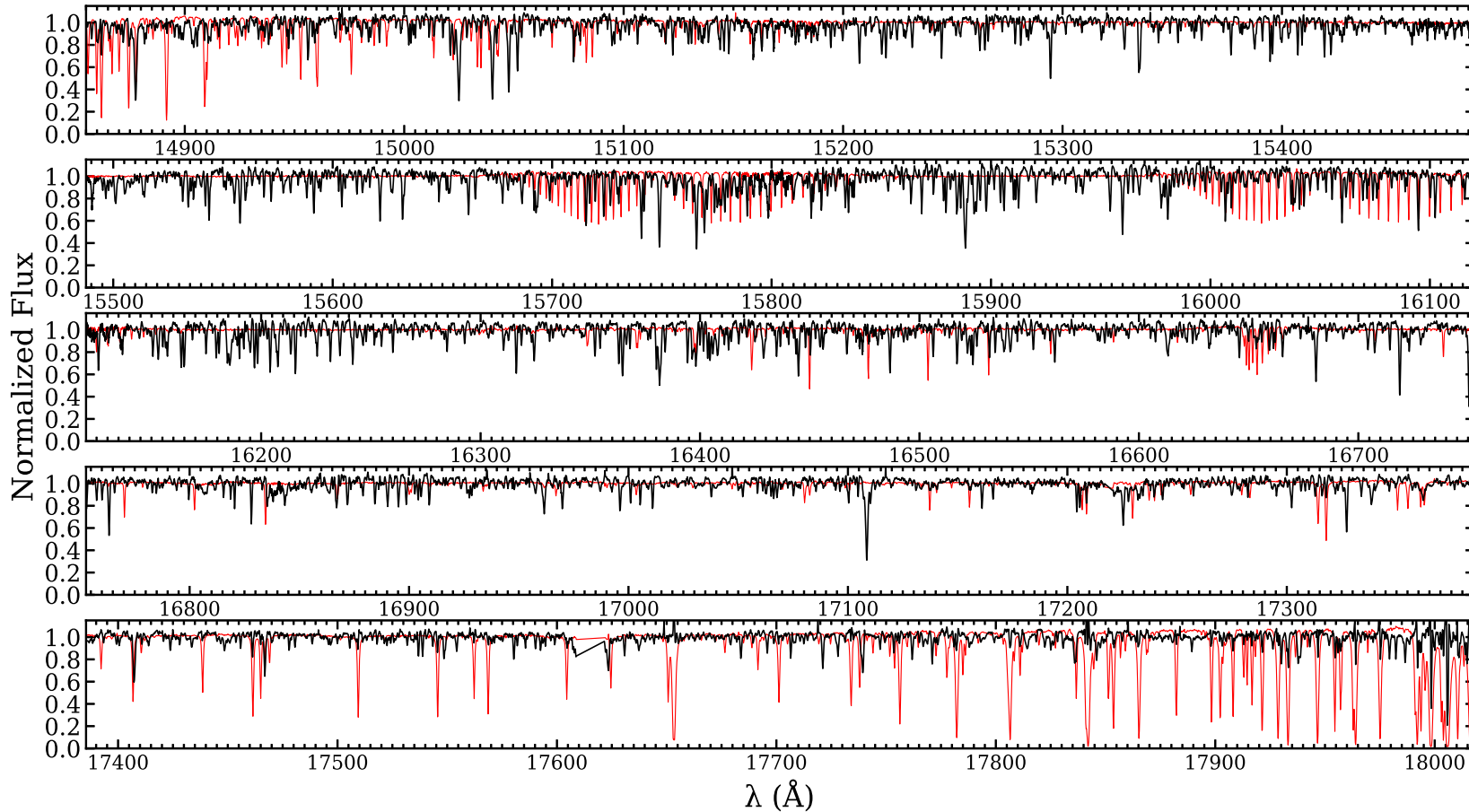
Figure 2.3: Observed H-band Arcturus spectrum (black line) with the telluric correction (red line)
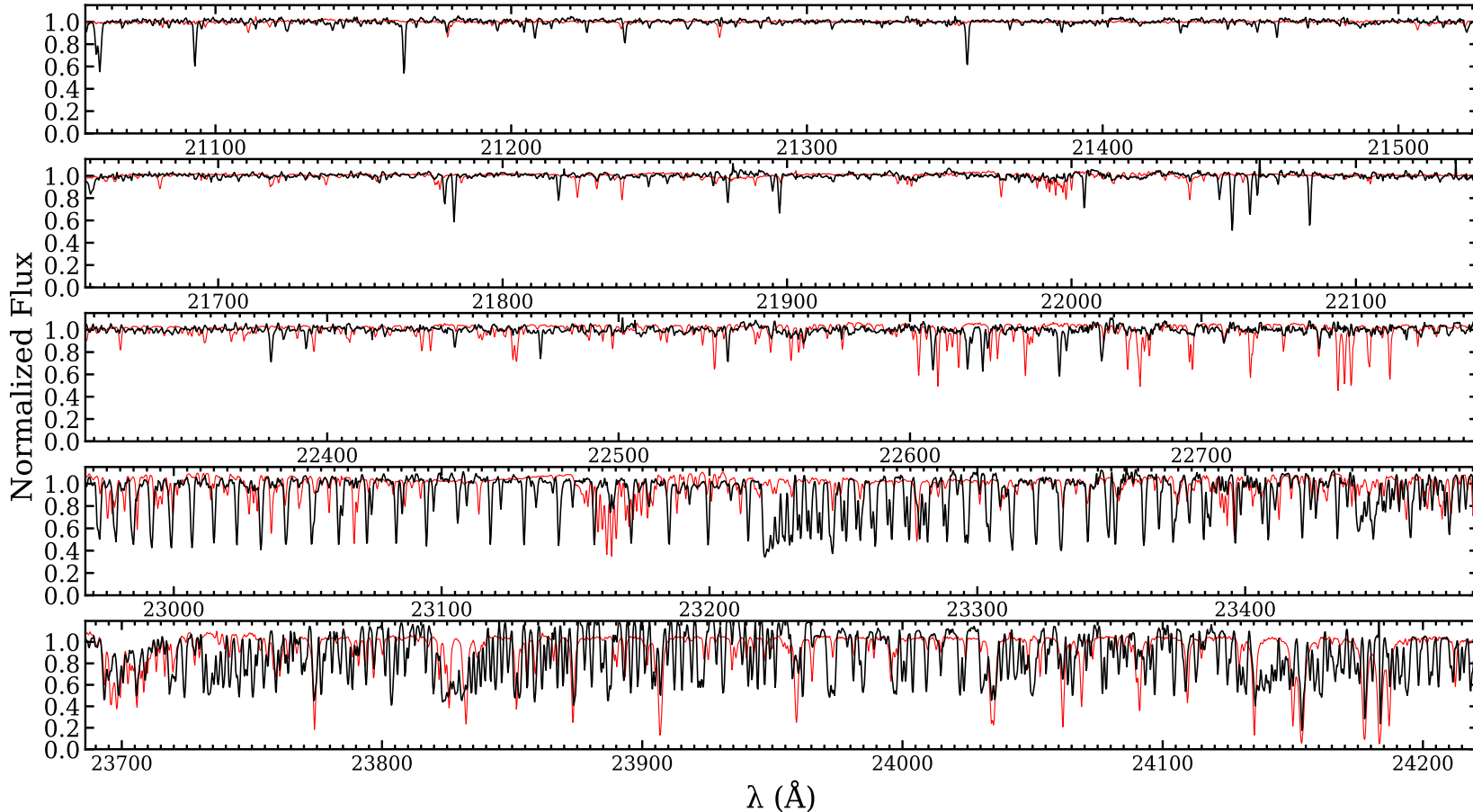
Figure 2.4: Observed K-band Arcturus spectrum (black line) with the telluric correction (red line)

2.2   Observations of RSGs in the Perseus complex

High resolution spectra for 84 young stars in the Persues complex have been simultaneously acquired with the TNG HARPS-N (Cosentino et al., 2014) and GIANO-B (Oliva et al., 2012a,b; Origlia et al., 2014) optical and NIR spectrographs, respectively, on November 3-5, 2018 and on November 6-12, 2019.

The RA-Dec map for the stars in the young stellar systems of the Perseus complex within a projected area of about 10 degrees on sky are shown in Fig. 2.5. Stars spectroscopically observed within the SPA Large Program are also highlighted. Stars have been selected with distances and proper motions consistent to those of the young clusters and associations in the area. HARPS-N covers the optical spectral
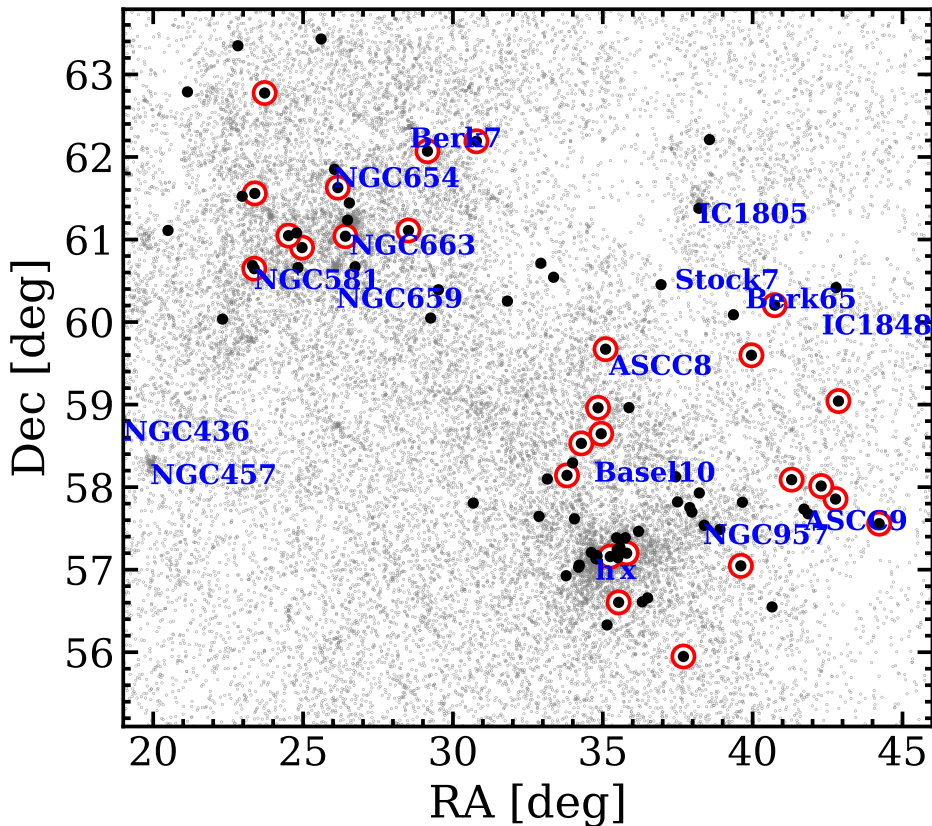
Figure 2.5: RA-Dec map of the stars likely members of the Perseus complex young clusters and associations (grey dots), based on their distances and proper motions, within a projected area of about 10 degrees on sky. Black dots mark the 84 stars spectroscopically observed within the TNG-SPA Large Program, while red circles mark the 27 RSGs studied in this work. For reference, we also marked in blue the main clusters in the region.

range (3780 − 6910 Å) at a resolution R∼115,000, while GIANO-B covers the NIR

spectral range ($9500 - 24500$ Å) at a resolution R$\sim$50,000. The simultaneous observation with HARPS-N and GIANO-B (named the GIARPS configuration) uses a dycroic that splits the optical and NIR light, thus allowing the simultaneous feeding of the two spectrographs (Claudi et al., 2017; Tozzi et al., 2016). On-source integration times between 700s and 3600s, depending on the target brightness, have been set to ensure signal-to-noise ratio >50 over the entire spectral range. GIANO-B spectra are actually the sum of pairs of sub-exposures of 300s obtained by nodding-on-slit, for an optimal subtraction of the background and other instrumental effects. HARPS-N spectra were reduced by the instrument Data Reduction Software pipeline and they were normalized using the code `RASSINE`* (Cretignier et al., 2020). The GIANO-B spectra were reduced using the data reduction pipeline software GOFIO (Rainer et al., 2018), which processes calibration (darks, flats, and U-Ne lamps taken in daytime) and scientific frames. The main feature of GOFIO is the optimal spectral extraction and wavelength calibration based on a physical model of the spectrometer that accurately matches instrumental effects such as variable slit tilt and order curvature over the echellogram (Oliva et al., 2018). The data reduction package also includes bad pixel and cosmic removal, sky and dark subtraction, flat-field and blaze correction. The GIANO-B spectra were also corrected for telluric absorption using the spectra of an O-type standard star taken at different air masses during the same night. The normalised spectra of the telluric standard taken at low and high air mass values were combined with different weights to match the depth of the telluric lines in the target spectra. The spectral regions with telluric transmission lower than 90% were normally excluded from the analysis, and the few intrinsic features of the O-stars used as telluric standards are broad lines of H and He that are easily recognisable and corrected using a Voigt fit.

Among the 84 observed stars, we classified as "genuine" RSGs the 27 reddest stars in the sample, with $M_G < -3$ or equivalently $L_{bol} > 3.9$ $L_\odot$. Three and seven RSGs in our sample are in common with Gazak et al. (2014) and de Burgos et al. (2020) samples, respectively. The other red stars in their samples were not first priority targets in our list since significantly closer and/or extremely bright in the NIR to be at risk of saturation with GIANO-B (depending on the seeing/cloud conditions) or extremely red.

Fig. 2.6 shows portions of the observed HARPS-N and the GIANO-B spectra for three representative RSGs analyzed, while Fig. 2.7 shows portions of the observed spectra for three representative blue-yellow stars in our sample.

---

*https://ascl.net/2102.022
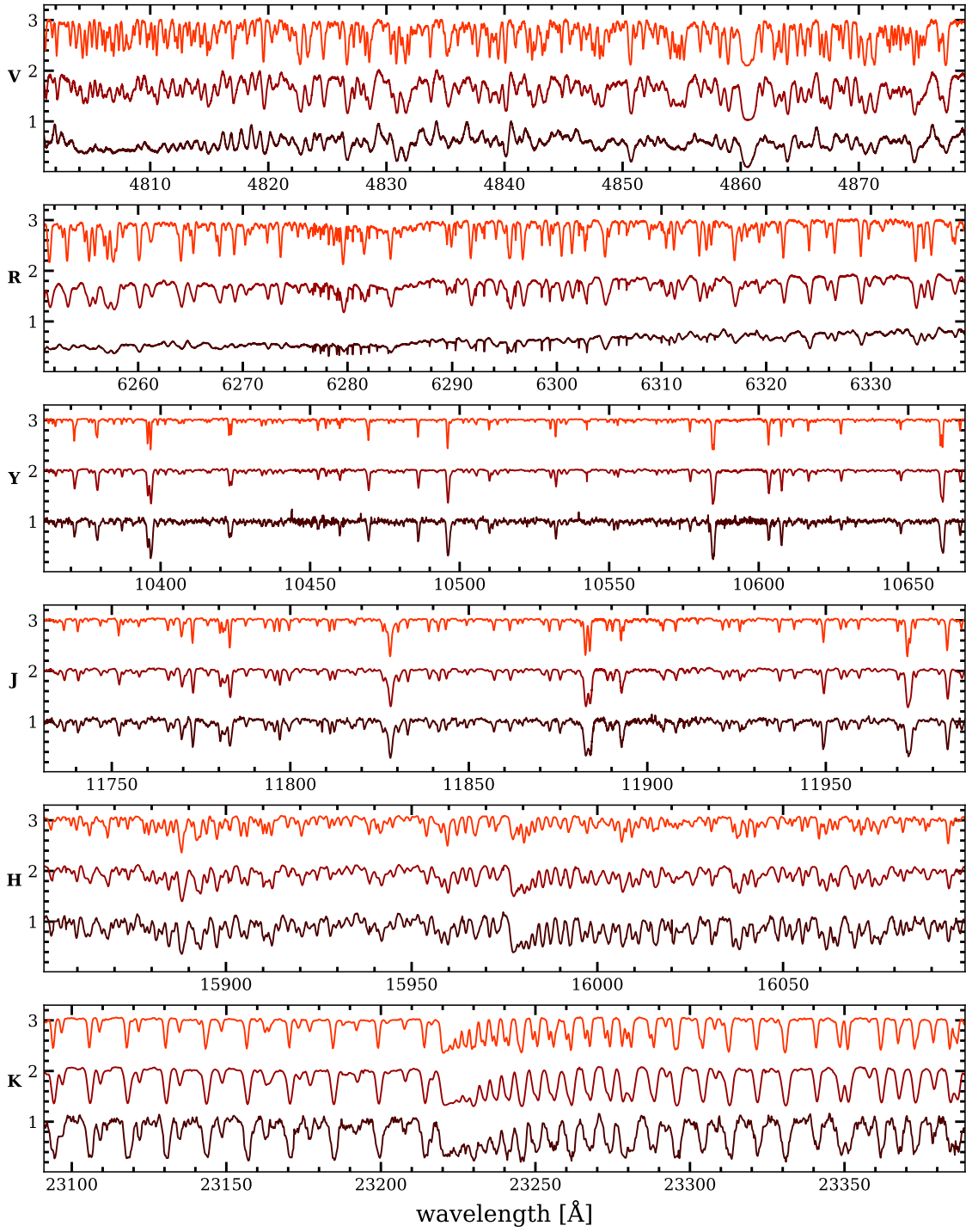
Figure 2.6: Portion of the HARPS-N and GIANO-B spectra in the V, R, Y, J, H and K bands for three representative RSGs observed in the Perseus complex. Spectra are corrected for telluric contamination and RV and they are plotted in order of increasing stellar temperature ($T_{eff} \approx 3500, 3700, 4100$ K) from the bottom to the top. In each panel the normalized spectra of the three stars are shifted by a constant.
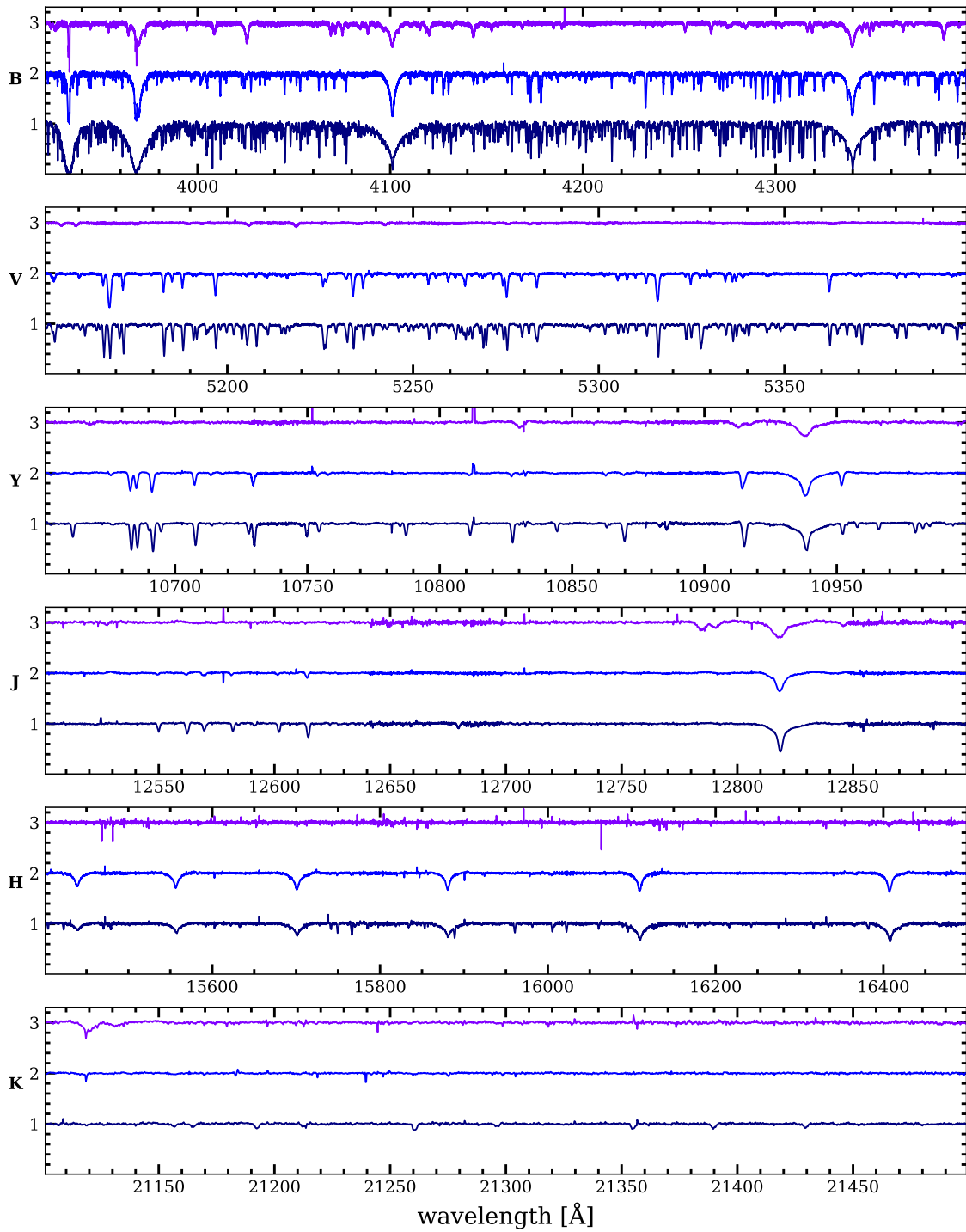
Figure 2.7: Portion of the HARPS-N and GIANO-B spectra in the B, V, Y, J, H and K bands for three representative blue-yellow stars observed in the Perseus complex. Spectra are corrected for telluric contamination and RV and they are plotted in order of increasing stellar temperature (T_{eff}=7000, 8000, 15000 K) from the bottom to the top. In each panel the normalized spectra of the three stars are shifted by a constant.

<div style="text-align: right">

Chapter **3**

</div>

Spectral analysis

High resolution spectra over a wide optical and NIR spectral range provide a unique tool to derive very accurate and precise radial and rotational velocities, stellar parameters and chemical abundances for the observed stars.

3.1 Measurement of radial and rotational velocities

A code in `Python` was developed to measure stellar radial and rotational velocities, named `StarVelox`[2].

Accurate (at better than 1 km s^{-1}) heliocentric radial velocities for the observed stars have been obtained by means of a standard cross-correlation technique (Tonry & Davis, 1979) between observed and synthetic spectra with stellar parameters similar to those of the observed stars over the full observed spectral range. To this purpose the `StarVelox`[2] code can use the entire observed spectrum or selected wavelength regions, and it also enables visually inspection of the cross-match between observed and synthetic spectra, if needed.

Accurate projected rotational velocities have been measured by using the Fourier transform (FT) method (Carroll, 1933; Carroll & Ingram, 1933; Collins & Truax, 1995a; Royer et al., 2002). According to the classical rotating stellar model (Collins & Truax, 1995b), the observed star line profile D(λ) can be considered as the convolution of an intrinsic line profile F(λ) (which includes any broadening effect other than rotation, such as thermal broadening, microturbulence, damping and instrumental broadenings) and a rotational broadening function, including limb darken-

ing, G(λ), such that:

$$D(\lambda) = F(\lambda) * G(\lambda)$$

which in the Fourier domain, is simplified by

$$d(\sigma) = f(\sigma) \cdot g(\sigma)$$

where σ is the Fourier frequency expressed in s km^{-1} and $d(\sigma)$, $f(\sigma)$ and $g(\sigma)$ are the Fourier transforms of $D(\lambda)$, $F(\lambda)$ and $G(\lambda)$, respectively.

A basic assumption is that the line profiles are identical on the stellar surface (i.e. stellar spot effects and surface inhomogeneities are negligible). This assumption is reliable (Reiners & Schmitt, 2002) for stars where rotation is the dominant broadening effect (i.e. for stars whose rotation is >10 kms^{-1}, Díaz et al. 2011)

Under the assumption that the star is a rotating rigid body, the rotational profile of a spectral line centered at a wavelength λ_0 with a linear limb-darkening law :

$$I_\lambda(\theta)/I_\lambda(0) = 1 - \epsilon + \epsilon cos\theta,$$

where ϵ is the limb darkening coefficient, I$_\lambda(\theta)$ represent the intensity from a surface element, whose angle between its normal and the observer's line of sight is given by θ, the zeros in $g(\sigma)$ can be analytically calculated.

By using the prescriptions of Reiners & Schmitt (2002), we can derive the limb darkening dependent rotationally broadening profile in λ_0 (Böhm, 1952) as

$$g_\epsilon(\sigma) = \frac{2}{x(1 - \frac{\epsilon}{3})}\left[1 - \epsilon J_1(x) + \epsilon\left(\frac{sinx}{x^2} - \frac{cosx}{x}\right)\right]$$

where $\mid \lambda - \lambda_0 \mid < \delta$ and $\delta = (\lambda_0 vsini)/c$ (Gray, 1976) and imposing x=$2\pi\delta\sigma$. The ϵ dependent zeros of g_ϵ can be determined from the equation:

$$(1 - \epsilon)J_1(x) + \epsilon\left(\frac{sinx}{x^2} - \frac{cosx}{x}\right) = 0.$$

$g(\sigma)$ and its zero positions $g(\sigma)_n$ scale with *vsini* (Carroll, 1933; Carroll & Ingram, 1933); σ can be expressed as

$$\sigma_n = q_n(\epsilon)/vsini$$

Therefore, for a given ϵ, *vsini* can be directly determined from the zero positions of $d(\sigma)$; for the first zero (i.e. the projected rotational velocity), Dravins et al. (1990)

gave an approximation for q_1 as:

$$q_1 = 0.610 + 0.062 \cdot \epsilon + 0.027 \cdot \epsilon^2 + 0.012 \cdot \epsilon^3 + 0.004 \cdot \epsilon^4$$

Fig. 3.1 shows the case of a single synthetic line with all the broadening effects with the exception of rotation ($f(\sigma)$, dash-dotted line), a pure rotational profile for vsini=50 km s^{-1} ($g(\sigma)$, solid line) and the same line with all the broadening effects ($d(\sigma)$, dotted line): the first zero position (marked with an arrow) indicates the projected projected rotational velocity.
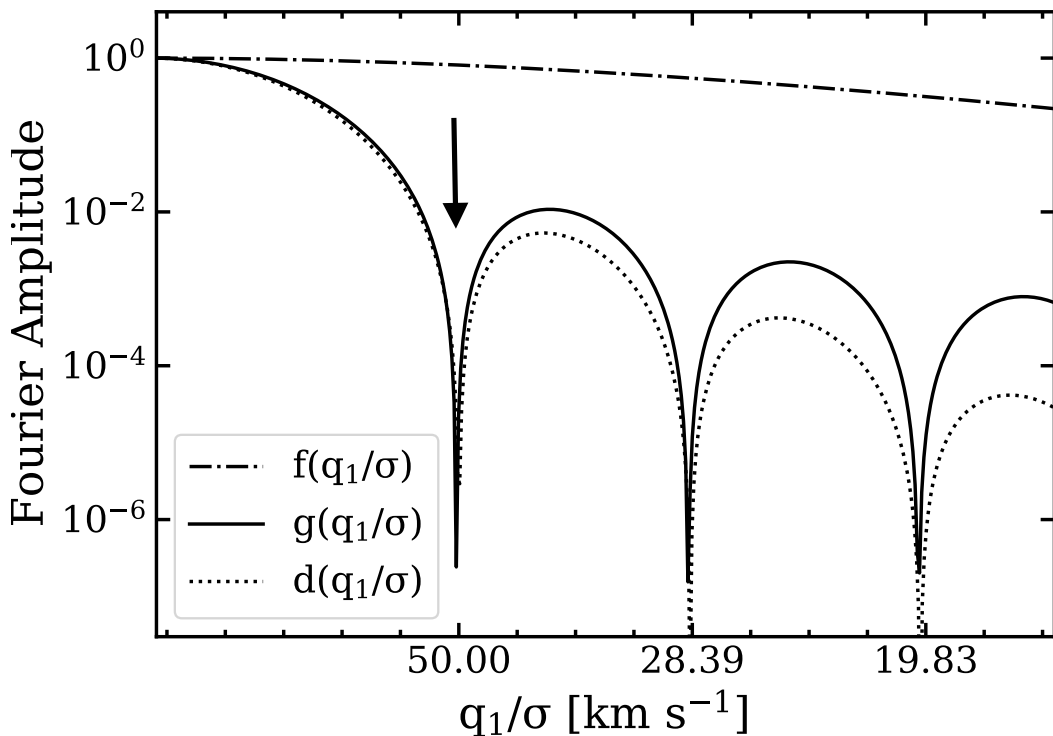
Figure 3.1: Power spectrum of the Fourier transform for the F (instrumental broadening v_{instr}=6 km s^{-1}; microturbulence broadening v_{micro}=2 km s^{-1}; radial-tangential broadening of v_{macro}=6 km s^{-1}; dash-dotted line), G (vsin(i)=50 km s^{-1}, solid line) and D (solid line) functions. The x-axis is in units of km s^{-1}. The arrow marks the position of the first zero, corresponding to the rotational velocity.

For measuring the projected rotational velocities we used a limb darkening coefficient of ϵ=0.6 (Reiners & Schmitt, 2002). A careful visual inspection of the results for all the unblended lines in each star spectrum was carried out.

3.2   Measurement of stellar parameters and chemical abundances

Accurate and precise stellar parameters and chemical abundances of red giant and supergiant stars can be determined by means of spectral synthesis techniques. A suitable grid of synthetic spectra spanning a comprehensive range of stellar parameters and chemical abundances is compared to high resolution observed spectra and a best fit solution is identified. Typically temperatures in the 3000-5000 K range, gravities log(g) in the -0.5-2.5 dex range, microturbulence in the 1-5 km s^{-1} range are explored.

For abundance analysis, synthetic spectra were computed by using the radiative transfer code `TURBOSPECTRUM` (Alvarez & Plez, 1998; Plez, 2012) under the Local Thermal Equilibrium (LTE) approximation, the MARCS models atmospheres (Gustafsson et al., 2008), the atomic data from VALD3 and the most updated molecular data from B. Plez website[*].

The synthetic spectra were then convoluted with a Gaussian function in order to reproduce the observed line profile. The line profiles of red giant and supergiant stars normally exceed the instrumental broadening (as determined from telluric lines) at R≥50,000 for GIANO-B spectra, and R≥115,000 for HARPS-N spectra. The additional broadening (typically a dozen km s^{-1}) is likely due to macroturbulence and it is normally modeled with a Gaussian profile, as for the instrumental broadening for cooler stars, while for the blue population is likely due to rotation, and it is modeled with a pure rotational profile.

Spectra of red giant and supergiant stars are quite crowded and at the lowest temperatures can be affected by severe molecular blending and blanketing effects. In order to obtain accurate and precise stellar parameters and chemical abundances, suitable sub-samples of un-contaminated and un-saturated atomic and molecular lines of the most important species, namely iron, iron-peak elements, CNO, alpha, Z-odd and neutron-capture elements need to be carefully selected. Tables in appendix A provide the complete list of optical and NIR atomic and molecular lines used for the abundance analysis of Arcturus and Tables in appendix B for the RSGs in the Perseus complex.

Lines have been checked against possible blending with close contaminants. To this purpose, I developed a `Python` code, named `TurboSLine`, that identifies as potential contaminants any atomic or molecular j-th line whose centroid λ_j is within one Full Width Half Maximum (FWHM) from the centroid λ_i of the analyzed i-th line.

---

[*]https://www.lupm.in2p3.fr/users/plez/

For each of these potential contaminant, we computed the theoretical line equivalent width (EW) and the amount of contamination, by using the following approximation:

$$C_j = EW_j \times \left(1 - \frac{|\lambda_i - \lambda_j|}{FWHM_j}\right)$$

If $\sum C_j > 0.1 \times EW_i$, the i-th line was classified as blended it was not normally used for abundance analysis.

Some other lines were also rejected because contaminated by the wings of nearby strong photospheric and/or by deep telluric lines by visual inspection. In our chemical analysis we also rejected strong lines because of the uncertainty in the modeling of their wings, and possible NLTE or chromospheric effects.

Effective temperatures have been obtained by minimizing the difference between carbon abundances derived from atomic C I and molecular CO lines, the so-called C-thermometer (see Sect. 4.1.1). These spectroscopic temperatures allow also the minimization of any trend between iron abundances and excitation potentials of both the optical and NIR lines.

Photometric estimates of the surface gravities can be obtained by assuming a stellar mass and using the standard formula

$$g = 4\pi G \sigma_{SF} \frac{MT_{eff}^4}{L_{Bol}} \tag{3.1}$$

where G is the gravitational constant, σ_{SF} is the Stefan-Boltzmann constant, M is the mass of the star and L_{Bol} is the bolometric luminosity.

For warmer stars spectroscopic estimates can be also obtained by comparing iron abundance from Fe I lines and from Fe II lines, since ionised lines are more sensitive to gravity than neutral ones.

For Arcturus we found a new spectroscopic diagnostic for deriving the surface gravity by balancing the O abundances derived from the forbidden transition [O I] at 6300.3 Å, and from the several OH lines measurable in the NIR spectrum (see Sect. 4.1.2).

Microturbulence has been derived by using the standard approach of minimizing the slope between the iron abundance and the reduced equivalent width (EW) of the measured lines, defined as $log_{10}(\text{EW}/\lambda)$.

For the computation of the chemical abundances we used `SALVADOR`, a tool developed by A. Mucciarelli (priv. comm.) that performs a χ^2 minimisation between observed and synthetic spectra, in correspondence of the selected lines, while the normalisation of the observed spectrum around each line is optimised interactively.

For a further check we also computed the line EWs and derived the corresponding abundances for the case of Arcturus. The latter were found to be practically coincident with those obtained from the spectral synthesis technique, with eventually only a slightly higher dispersion, likely due to the fact that with the EW method lines with some impurity provide slightly more uncertain abundances.

The Arcturus Lab

Detailed, high resolution optical and NIR spectroscopy of stellar calibrators is fundamental to define optimal diagnostics for atmospheric parameters and chemical analysis of stars and stellar populations with different ages, metallicities and evolutionary properties.

While diagnostic tools from high resolution optical spectroscopy are well established and calibrated since a longtime, those from NIR spectroscopy started to be explored only recently, thanks to the new generation of NIR echelle spectrographs with adequate performances for such quantitative studies.

We used Arcturus as a laboratory to explore optical and NIR spectroscopic diagnostics for chemical analysis over the full spectral range from 4800 to 24500. We then provided a comprehensive and self-consistent determination of Arcturus stellar parameters and chemical abundances.

Arcturus (α *Boo*, *HR5340*, *HIP69673*, *HD124897*) is a luminous, nearby K1.5 IIIp giant star, often used as a calibrator in chemical studies of cool stellar populations. Differential chemical analysis of giant stars relative to Arcturus can indeed largely minimise most of systematic errors due to atmospheric parameters (e.g. Alves-Brito et al., 2010; McWilliam & Rich, 1994; Ramírez & Allende Prieto, 2011; Worley et al., 2009).

Most of the chemical studies of Arcturus are based on optical high resolution spectroscopy. The reference Arcturus spectrum covering the entire spectral range from

the ultraviolet to the infrared is the one made available by Hinkle & Wallace (2005, and references therein). This spectrum has been built up by using three different instruments: Space Telescope Imaging Spectrograph (STIS) mounted on board of the Hubble Space Telescope in the 1000-3000 Å range, the echelle optical spectrograph in the 3100-9000 Å range and the Fourier transform spectrometer in the 0.9-5 μm range mounted at the Kitt Peak National Observatory (KPNO) 4 m telescope. Ryde et al. (2009) used a portion of the Hinkle & Wallace (2005) H-band spectrum, from 15326 to 15705 Å, to study several clean molecular lines of CO, CN, and OH and derive C, N, and O abundances. Ramírez & Allende Prieto (2011) provided atmospheric parameters and abundances for several metals by mostly using the Hinkle & Wallace (2005) optical spectrum and the line list by Asplund et al. (2009). Smith et al. (2013) and Shetrone et al. (2015) used the H-band portion of the Hinkle & Wallace (2005) spectrum and their detailed line list prepared for the Sloan Digital Sky Survey III Apache Point Galactic Evolution Experiment (APOGEE) (Majewski et al., 2007) to provide stellar parameters, Fe, CNO and other elemental abundances.

Arcturus was also studied by Fulbright et al. (2006) using an optical spectrum taken with the Hamilton spectrograph at the 0.6m CAT telescope of the Lick Observatory. Kondo et al. (2019) have analised a ZYJ spectrum of Arcturus at R$\simeq$ 28000 taken with the WINERED spectrograph at the 1.3 m Araki Telescope at Koyama Astronomical Observatory. They derived Fe I abundances and microturbolence using two different line list, namely the Vienna Atomic Line Database (VALD3) (Ryabchikova & Pakhomov, 2015) and the public line list provided by Meléndez & Barbuy (1999). Finally we mention the works by D'Orazi et al. (2011); Maas et al. (2017); Overbeek et al. (2016) who discussed the Arcturus abundances of P, Y and Dy, respectively. Table 4.1 lists stellar parameters and metallicity [Fe/H] of Arcturus as inferred from different optical and NIR studies.

In this chapter a comprehensive optical and NIR high resolution spectroscopic

Table 4.1: Stellar parameters and metallicity of Arcturus inferred from different optical and NIR studies.

T_{eff}	log(g)	ξ	[Fe/H]	Range	Res	References
K	dex	km s^{-1}	dex		$\lambda/\Delta\lambda$	
4283 ± 30	1.55	1.61 ± 0.03	-0.55 ± 0.07	$5370 - 7880$	45000	Fulbright et al. (2006)
4290	1.55	1.70	-0.50	$5000 - 7000$	50000	Ryde et al. (2009)
4286 ± 30	1.66 ± 0.05	1.74	-0.52 ± 0.02	$5000 - 9300$	100000	Ramírez & Allende Prieto (2011)
4275 ± 50	1.70 ± 0.10	1.85 ± 0.05	-0.52 ± 0.04	$15100 - 17000$	22300	Smith et al. (2013)
4286 ± 50	1.66 ± 0.10	1.70 ± 0.05	-0.57 ± 0.04	$15100 - 17000$	22300	Shetrone et al. (2015)
4286 ± 35	1.64 ± 0.06	1.22 ± 0.12	-0.69 ± 0.06	$9300 - 13100$	28000	Kondo et al. (2019) (VALD3 linelist)
4286 ± 35	1.64 ± 0.06	1.20 ± 0.11	-0.49 ± 0.04	$9300 - 13100$	28000	Kondo et al. (2019) (MB99 linelist)

study of Arcturus has been performed by using the echelle YJHK spectrum at

R=50000 obtained with the GIANO-B spectrograph at the TNG and archive optical spectra obtained with the UVES spectrograph at the VLT and suitable synthetic spectra computed as detailed in Chapter 3.

Figs. 2.1, 2.2, 2.3 and 2.4 show the observed rest-frame, normalised GIANO-B spectra of Arcturus corrected for telluric absorption and radial velocity. The average signal-to-noise ratio of the reduced and telluric-corrected spectrum is about 150 per pixel.

The synthetic spectra were convoluted with a Gaussian function in order to reproduce the observed broader profile that corresponds to an equivalent resolution of $32,000$. The extra broadening is mainly due to the macro-turbulence velocity ($\approx 6\,\mathrm{km\ s^{-1}}$), because the projected rotational velocity of Arcturus is negligible ($\xi_{rot} = 2.4\,\mathrm{km\ s^{-1}}$, Gray 1981).

By the combined NIR and optical analysis we defined a new thermometer and a new gravitometer for giant stars, based on the comparison of Carbon and Oxygen abundances, respectively, as derived from atomic and molecular lines. We then derived self-consistent stellar parameters and chemical abundances of iron, CNO, iron-group, alpha, Z-odd and neutron-capture elements over the full $4800 - 24500$ Å spectral range and we compared them with previous studies in the literature. We finally discussed a number of problematic lines, which can be affected by deviations from thermal equilibrium and/or chromospheric activity, as traced by the observed variability of He I at 10830 Å.

4.1   Standard and new methods to derive stellar parameters

Arcturus belongs to a kinematic group of several tens old stars (Eggen, 1971). Its metallicity ([Fe/H]$\simeq -0.5$ dex) and some enhancement of the alpha elements suggest that it likely formed in the thick disk of our Galaxy (Bensby et al., 2014; Ramírez & Allende Prieto, 2011), although an extragalactic origin has been also proposed (Navarro et al., 2004). From a kinematic perspective, Arcturus total velocity $v_t = \sqrt{(U^2 + V^2 + W^2)} = 106$ km s^{-1} and its location in the Toomre diagram (see Fig. 4.1), suggest that it should be a thick disk star (Bensby et al., 2014).

Previous determinations of Arcturus stellar parameters (cf. Table 4.1) suggested temperatures in the 4275-4290 K range, log(g) in the 1.55-1.70 dex range and microturbulence in the 1.20-1.85 km s^{-1} range.

By using the Dartmouth web-tool* (Dotter et al., 2008), we computed isochrones

---

*http://stellar.dartmouth.edu
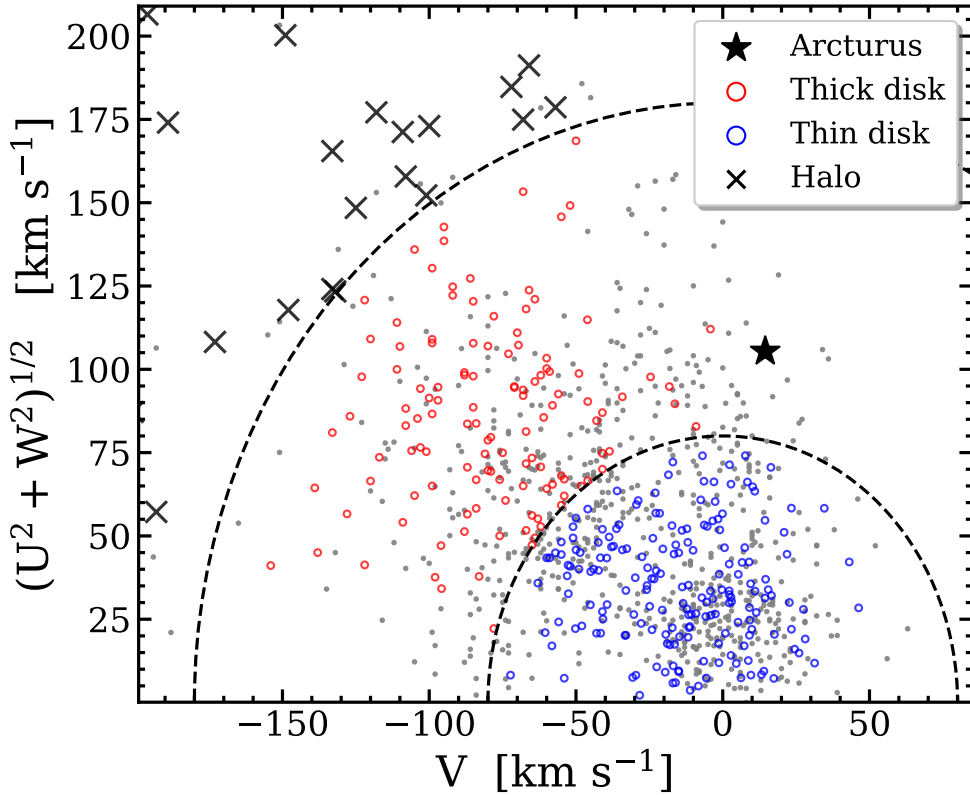
Figure 4.1: Toomre diagram for thin (blue dots), thick (red dots) disk and halo (black crosses) stars from Reddy et al. 2003 and Reddy et al. 2006 and for the disk stars of Bensby et al. 2014 (grey dots). The black star marks the position of Arcturus and the dashed lines delineate constant total space velocities with respect to the LSR of $V_{tot} = 80$ and 180 km s^{-1}, respectively (e.g. Nissen, 2004, and references therein).

with [Fe/H]$=-0.5$, [α/Fe]$=+0.20$ and different ages. At the bolometric luminosity of Arcturus ($L_{bol} = 174 \pm 7 \; L_{\odot}$, Smith et al. (2013), see also Ramírez & Allende Prieto (2011)) we found that old ($\geq$10 Gyrs) ages are consistent with effective temperature T_{eff} in the 4260-4310 K range and gravity log(g) in the 1.60-1.70 dex range.

We used these photometric ranges for T_{eff} and log(g) to also constrain the microturbulence velocity range, by using the standard approach of minimizing the slope between the iron abundance and the reduced equivalent widths (EW) of the measured lines $\log_{10}(EW/\lambda)$ (see the discussion in Mucciarelli, 2011). We find microturbulence velocities in the 1.50 and 1.70 km s^{-1} range. We finally adopted the value of $\xi = 1.60 \pm 0.05 \, \text{km s}^{-1}$, that best minimizes any trend between the abundances and the reduced equivalent width of about 400 Iron lines distributed over the

$4800 - 23400$ Å spectral range, as shown in Fig. 4.2. This value of microturbulence also minimizes the trend when the optical and the NIR lines are taken separately.

As described in the following, the photometric values of T_{eff} and $\log(g)$ were
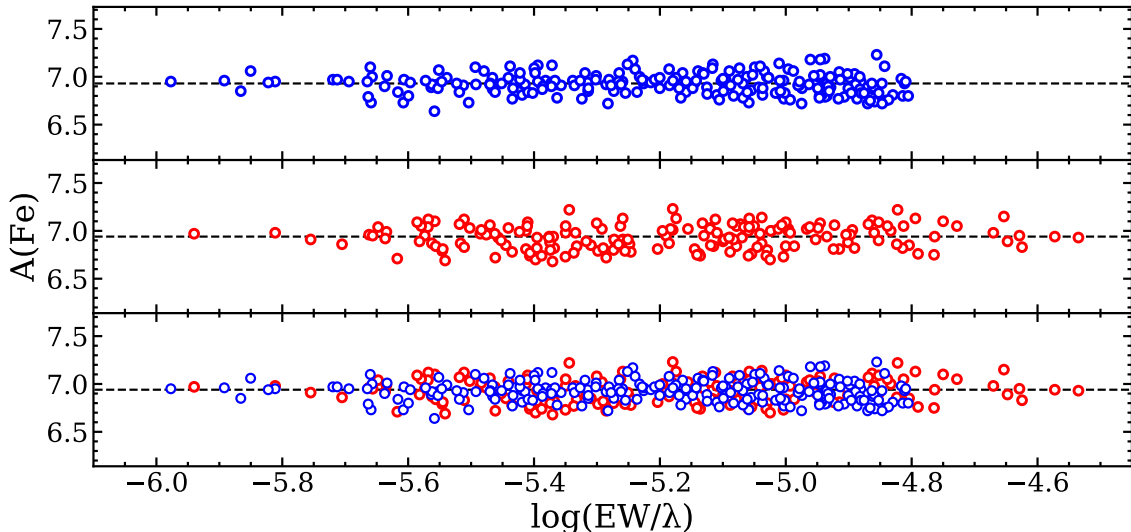
Figure 4.2: Iron abundances as a function of the reduced equivalent widths for all the measured optical (blue circles) lines in the UVES spectra and NIR (red circles) lines in the GIANO-B spectrum. The dotted line marks the best-fit median abundance.

fined-tuned using the spectroscopic data.

4.1.1 The C-thermometer

We defined a new, powerful diagnostic tool to derive T_{eff} in Oxygen-rich cool stars, based on the balance between the Carbon abundance, derived from atomic lines (see Table 4.2), and molecular CO roto-vibration transitions. Hereafter, we refer to this method as the C-thermometer.

The basic principle of such a thermometer follows from the very high dissociation potential of the CO molecule (11.1 eV). Thus the CO/C^0 relative abundance of carbon in molecular (CO) and atomic (C^0) form has a very strong exponential dependence on temperature. Alike other diatomic molecules, the abundance ratio also depends linearly on the gas pressure (i.e. on gravity); but this effect is much less important. Figure 4.3 shows the behaviour of the Saha-equilibrium abundances for gas temperatures and pressures relevant for this work.

When modeling the spectrum, CO and C I lines must provide the same abundances. If this does not happen it is because the model temperature is wrong and must be tuned until the two abundances are matched. However, the analysis is complicated

Table 4.2: Measurable atomic Carbon lines in the NIR spectrum of Arcturus.

λ_{air}	χ eV	log(gf)	Note
8727.140	1.26	-8.165	Forbidden
9658.435	7.49	-0.280	NLTE
10683.080	7.48	$+0.079$	NLTE
10685.340	7.48	-0.272	NLTE
10691.245	7.49	$+0.344$	NLTE
10707.320	7.48	-0.411	NLTE
10729.529	7.49	-0.420	NLTE
11748.220	8.64	$+0.375$	NLTE
11753.320	8.65	$+0.691$	NLTE
11754.760	8.64	$+0.542$	NLTE
17234.463	9.70	$+0.293$	LTE
17448.535	9.00	$+0.012$	LTE
17672.039	7.95	-1.974	LTE
17768.910	9.71	$+0.420$	LTE
17793.158	9.71	-0.045	LTE

by the fact that some C I lines may show significant departure from local thermodynamic equilibrium (NLTE, see e.g. Fabbian et al. 2006; Takeda & Takada-Hidai 2013); while CO lines form under LTE conditions (e.g. Hinkle & Lambert, 1975; Ryde et al., 2009). For example, Takeda & Takada-Hidai (2013) show that the 10683/10685/10691 Å multiplet in the Y-band requires NLTE correction for a star like Arcturus. In particular the 10691 Å line needs a correction of $\Delta A(C) = -0.23$ dex.

NLTE corrections are sensitive to the adopted stellar model and depend on temperature and gravity, hence they cannot be safely used to define a reliable thermometer. Hence, it is desirable to use only those C I lines that are not affected by NLTE effects. To this purpose, given that forbidden lines do not suffer from NLTE (e.g. Alexeeva & Mashonkina, 2015), we used the [C I] at 8727.14 Å measurable in our UVES red spectrum, to derive a proxy of the atomic Carbon abundance in LTE. Then, we computed LTE abundances for all the C I lines measurable in our GIANO-B spectrum (Table 4.2) and we checked their abundances against that from the [C I] line. We found that the C I lines in the H-band with excitation potentials above 9 eV provide similar C abundances; while the C I lines in the Y and J bands with lower excitation potentials give LTE abundances that are systematically (~ 0.3 dex) larger; most likely because of NLTE effects. Hence, we used only the C I lines in the H-band for the C-thermometer.
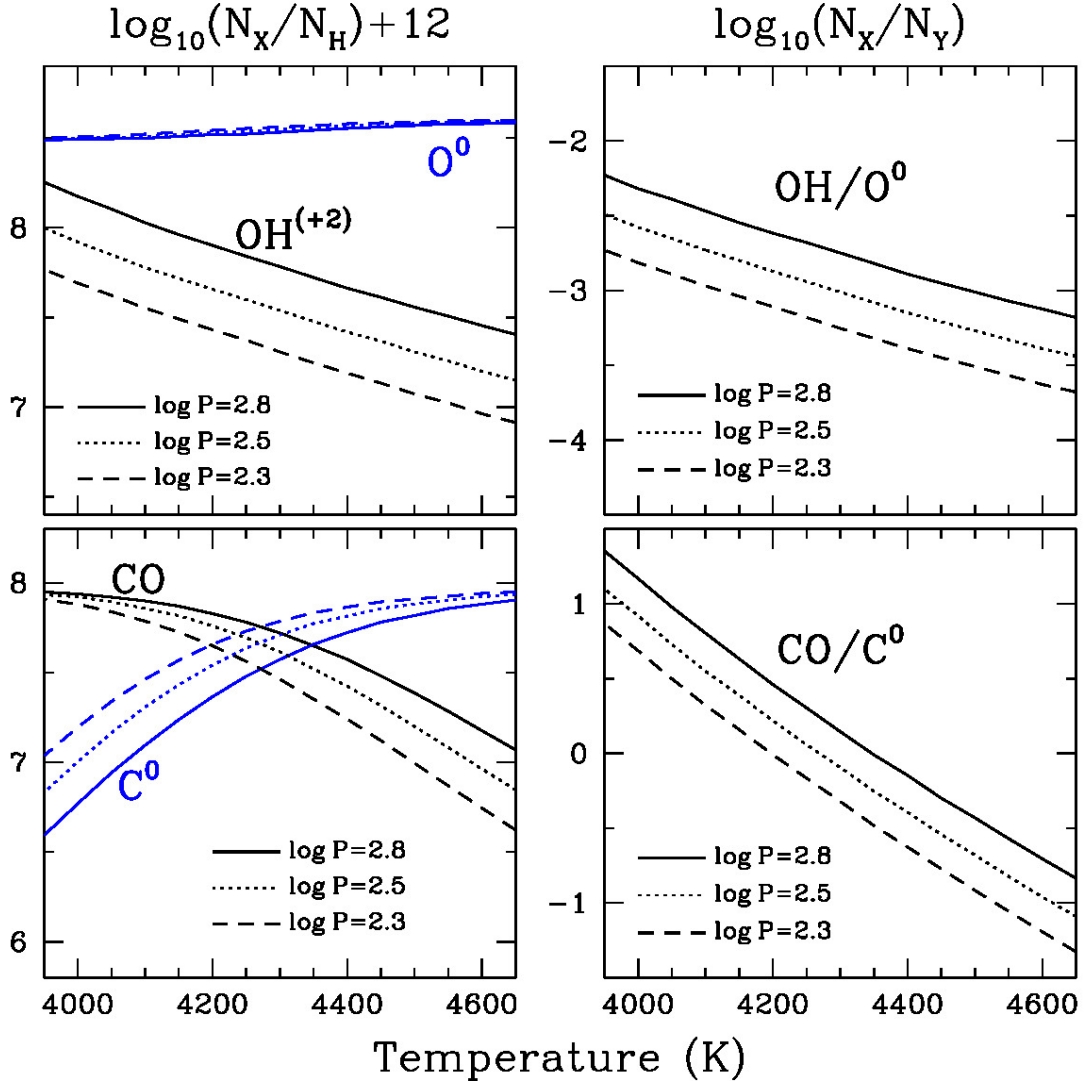
Figure 4.3: The selected values of pressure are representative of the line forming regions for surface gravities log(g)=2.0, 1.5 and 1.0

Fig. 4.4 shows the variation of Carbon abundance from C I and CO lines in the Arcturus GIANO-B spectrum as a function of T_{eff}. Both diagnostics are very sensitive to T_{eff} but with opposite trends. The intersection of the two curves occurs at $T_{eff} = 4283 \pm 33$ K. The quoted error of ± 33 K corresponds to a $\pm 1\sigma$ variation in the derived C abundances from C I and CO. The C-thermometer is virtually independent from the other parameters within the uncertainties. Indeed, variations of ± 0.05 km s^{-1} in microturbulence velocity or ± 0.06 dex in log(g) have a negligible impact both on temperature (≤ 15 K) and on C abundance (≤ 0.02 dex). Even for larger variation of log(g) (up to 0.2 dex) and ξ (up to 0.2 kms^{-1}) the corresponding variation in temperature turns out to be within the error. In-
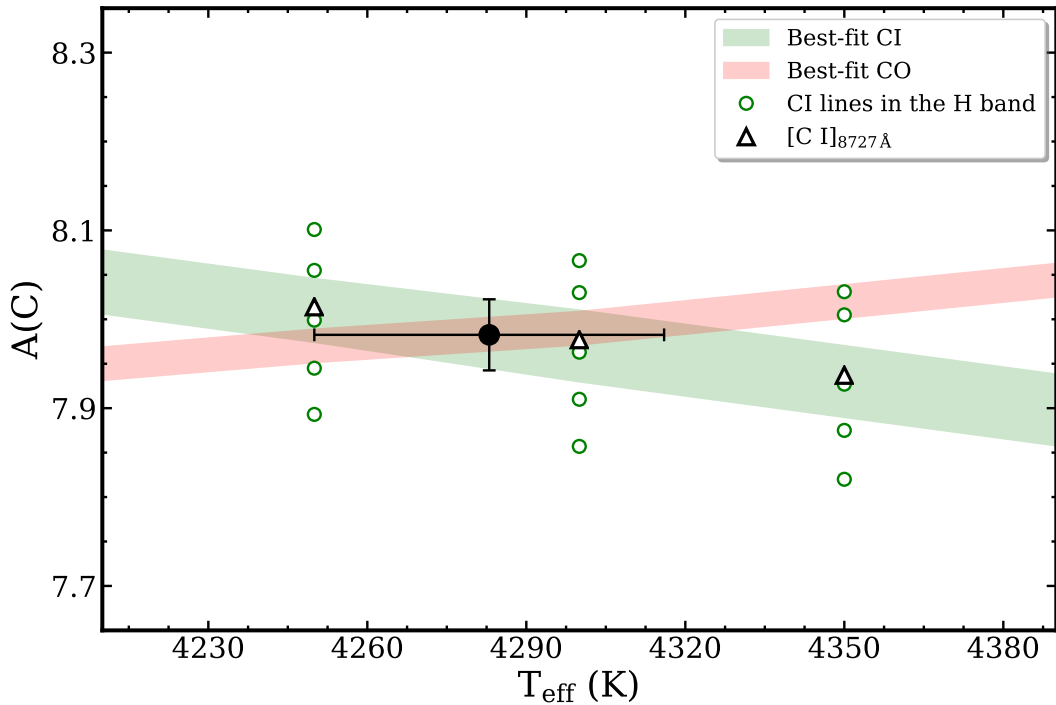
Figure 4.4: C abundances as a function of temperatures from the C I lines in the H band (green circles), the forbidden [C I] line at 8727.14 Å (empty triangle). The shaded green region is the corresponding best-fit $\pm 1\sigma$ trend of the C I lines, while the shaded red region is the best-fit $\pm 1\sigma$ trend of the CO lines. The big black dot marks the point of intersection of the two curves and its x-coordinate provides the best-fit temperature.

teresting ly, the C-thermometer also works if the molecular Carbon abundance is derived from spectral synthesis of the $\Delta v = 3$ CO band-heads in the H-band, since it is fully consistent with the one derived from individual CO roto-vibration lines (see Sect. 4.2.1). Noticeably, the temperature of 4283 $\pm$33 K derived from the C-thermometer also allows us to minimize, within the errors, any trend between Iron abundances from neutral lines and their excitation potential, as shown in Fig. 4.5, which is the standard spectroscopic method to infer the effective temperature.

4.1.2   The O-gravitometer

The relative abundance of OH and atomic Oxygen (O^0) depends linearly on the gas pressure (i.e. on gravity), while it has a weak dependence on temperature (see Figure 4.3) because of the low dissociation potential of the OH molecule (4.4 eV). Therefore, the OH/O^0 ratio can be used to estimate the gravity once the temperature is constrained.

After fixing the temperature at $T_{eff} = 4283$ K, as derived from the C-thermometer, one can fine-tune gravity by balancing the O abundances derived from the forbidden
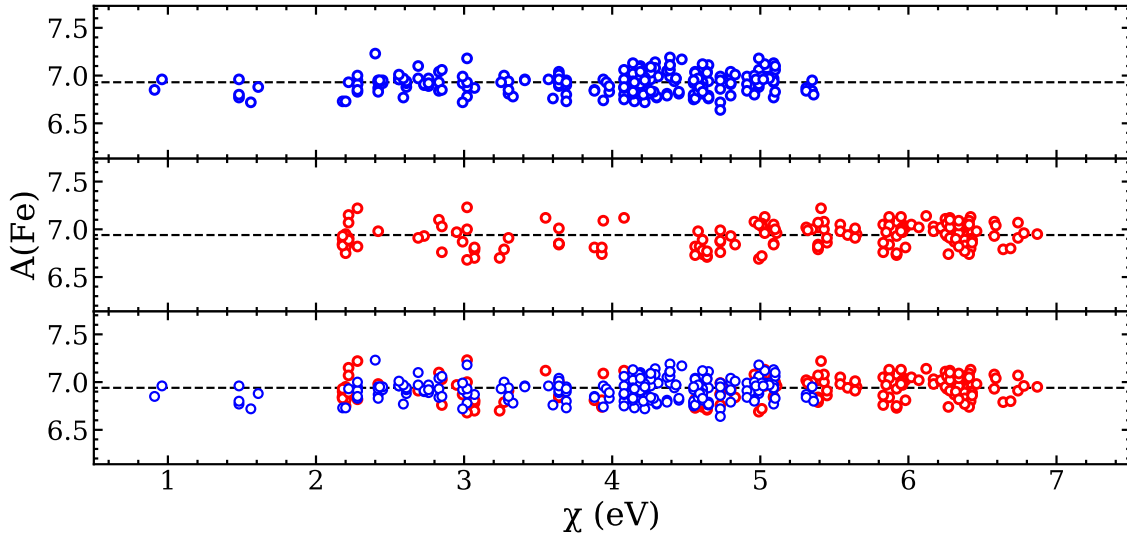
Figure 4.5: Iron abundances from neutral lines in the optical UVES spectra (blue circles) and in the NIR GIANO-B spectrum (red circles) as a function of their excitation potential. Dotted line marks the derived best-fit median Iron abundance.

transition [O I] at 6300.3 Å, and from the numerous OH lines measurable in the NIR spectrum. Fig. 4.6 (top panel) shows the variation of O abundance from the [O I] and OH lines in the Arcturus optical and NIR spectra, respectively, as a function of $\log(g)$. The intersection of the two curves occurs at $\log(g) = 1.67 \pm 0.06$ dex. The quoted error of ± 0.06 dex corresponds to a $\pm 1\sigma$ variation in the derived O abundances from [OI] and OH.

Variations of $\pm$ 33 K in temperature impact gravity by ± 0.10 dex, while variations of ± 0.05 km s^{-1} in microturbulence velocity impact $\log(g)$ by ∓ 0.02 dex. By using the standard method to infer spectroscopic $\log(g)$, i.e. minimizing the difference between the iron abundances from neutral and ionized optical lines, we obtained a very similar best-fit $\log(g)=1.68 \pm 0.10$ dex (see Fig. 4.6, bottom panel).
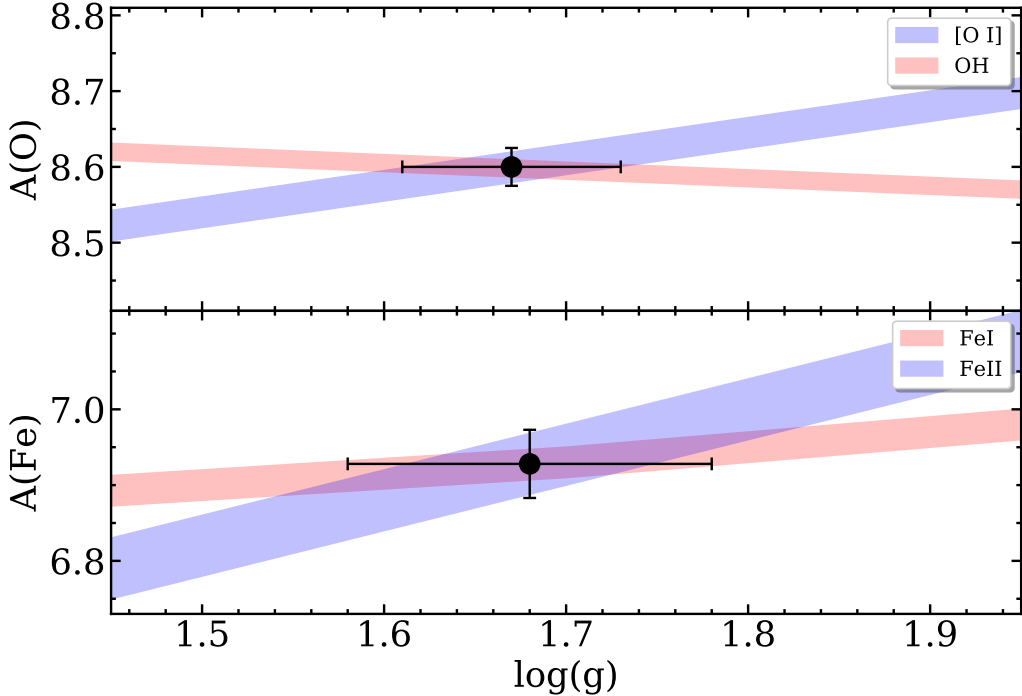
Figure 4.6: *Top panel*: Oxygen abundances as a function of gravity. The shaded blue region is the best-fit $\pm 1\sigma$ trend of the forbidden [O I] line, while the shaded red region is the best-fit $\pm 1\sigma$ trend of the OH lines. The black dot marks the point of intersection of the two curves and its x-coordinate provides the best-fit log(g)=1.67$\pm$0.06. *Bottom panel*: Iron abundances as a function of gravity. The shaded red region is the best-fit $\pm 1\sigma$ trend of the neutral Fe I lines, while the shaded blue region is the best-fit $\pm 1\sigma$ trend of the ionized Fe II lines. The black dot marks the point of intersection of the two curves and its x-coordinate provides the best-fit log(g)=1.68 $\pm$ 0.10.

4.2   Combined optical and NIR chemical analysis

The adopted stellar parameters for the chemical analysis of Arcturus are summarised in Table 4.3. Abundance errors from uncertainties in the stellar parameters

Table 4.3: Stellar parameters for Arcturus adopted in the present study.

Paramater	Value	Error
T_{eff}	4283 K	33 K
log(g)	1.67 dex	0.06 dex
ξ	1.60 kms^{-1}	0.05 kms^{-1}
$[Fe/H]$	-0.57 dex	0.01 dex

were estimated by computing elemental abundances with varying T_{eff} by ± 33 K, log(g) by ± 0.06 dex, and ξ by ± 0.05 km s^{-1} (see Table 4.3 and Fig. 4.8).

Table 4.4: Arcturus chemical abundances and associated measurement errors from NIR and optical lines.

X	Z	NIR							OPT							OPT+NIR					
		# lines	log(N)^a	[X/H] Gre98	[X/H] Aspl09	[X/Fe] Gre98	[X/Fe] Aspl09	ϵ	# lines	log(N)^a	[X/H] Gre98	[X/H] Aspl09	[X/Fe] Gre98	[X/Fe] Aspl09	ϵ	log(N)^a	[X/H] Gre98	[X/H] Aspl09	[X/Fe] Gre98	[X/Fe] Aspl09	ϵ
C	6	19^b	7.97	−0.55	−0.46	+0.01	+0.10	0.02	1	8.00	−0.52	−0.43	+0.05	+0.14	0.05	7.97	−0.55	−0.46	+0.02	+0.11	0.06
N^b	7	137	7.64	−0.28	−0.19	+0.28	+0.37	0.01	0	−	−	−	−	−	−	−	−	−	−	−	−
O^b	8	14	8.60	−0.23	−0.09	+0.33	+0.47	0.02	1	8.61	−0.22	−0.08	+0.35	+0.49	0.02	8.60	−0.23	−0.09	+0.34	+0.48	0.06
F^b	9	1	4.22	−0.34	−0.34	+0.22	+0.22	0.05	0	−	−	−	−	−	−	−	−	−	−	−	−
Fe I	26	179	6.94	−0.56	−0.56	+0.00	+0.00	0.01	230	6.93	−0.57	−0.57	+0.00	+0.00	0.01	6.93	−0.57	−0.57	+0.00	+0.00	0.01
Fe II	26	1	6.95	−0.55	−0.55	+0.01	+0.01	0.04	10	6.94	−0.56	−0.56	+0.01	+0.01	0.03	6.94	−0.56	−0.56	+0.01	+0.01	0.05
V I	23	4	3.48	−0.52	−0.45	+0.04	+0.11	0.07	41	3.49	−0.51	−0.44	+0.06	+0.13	0.03	3.49	−0.51	−0.44	+0.06	+0.13	0.08
Cr I	24	29	5.04	−0.63	−0.60	−0.07	−0.04	0.03	33	5.02	−0.65	−0.62	−0.08	−0.05	0.02	5.03	−0.64	−0.61	−0.07	−0.04	0.04
Mn I	25	4	4.84	−0.55	−0.59	+0.01	−0.03	0.04	5	4.83	−0.56	−0.60	+0.01	+0.03	0.05	4.83	−0.56	−0.60	+0.01	+0.03	0.06
Co I	27	6	4.44	−0.48	−0.55	+0.08	+0.01	0.06	36	4.44	−0.48	−0.55	+0.09	+0.02	0.02	4.44	−0.48	−0.55	+0.09	+0.02	0.06
Ni I	28	31	5.73	−0.52	−0.49	+0.04	+0.07	0.02	42	5.69	−0.56	−0.53	+0.01	+0.04	0.01	5.71	−0.54	−0.51	+0.03	+0.06	0.02
Cu I	29	1	3.83	−0.38	−0.36	+0.18	+0.20	0.04	1	3.81	−0.40	−0.38	+0.17	+0.19	0.03	3.82	−0.39	−0.37	+0.18	+0.20	0.05
Zn I	30	2	4.19	−0.41	−0.37	+0.15	+0.19	0.07	1	4.19	−0.41	−0.37	+0.16	+0.20	0.06	4.19	−0.41	−0.37	+0.16	+0.20	0.09
Mg I	12	11	7.33	−0.25	−0.27	+0.31	+0.29	0.02	7	7.36	−0.23	−0.25	+0.34	+0.32	0.02	7.34	−0.24	−0.26	+0.33	+0.31	0.03
Si I	14	58	7.26	−0.29	−0.25	+0.27	+0.31	0.03	40	7.26	−0.29	−0.25	+0.28	+0.32	0.02	7.26	−0.29	−0.25	+0.28	+0.32	0.04
S I	16	11	6.90	−0.43	−0.22	+0.13	+0.34	0.05	3	6.91	−0.42	−0.21	+0.15	+0.36	0.05	6.90	−0.43	−0.22	+0.14	+0.35	0.07
Ca I	20	24	5.84	−0.52	−0.50	+0.04	+0.06	0.02	22	5.80	−0.56	−0.54	+0.01	+0.03	0.02	5.82	−0.54	−0.52	+0.03	+0.05	0.03
Ti I	22	57	4.59	−0.43	−0.36	+0.13	+0.20	0.02	112	4.55	−0.47	−0.40	+0.10	+0.17	0.01	4.56	−0.46	−0.39	+0.11	+0.18	0.02
Ti II	22	0	−	−	−	−	−	−	21	4.61	−0.41	−0.34	+0.16	+0.23	0.03	−	−	−	−	−	−
Na I	11	3	5.78	−0.55	−0.46	+0.01	+0.10	0.04	3	5.76	−0.57	−0.48	+0.00	+0.09	0.03	5.77	−0.56	−0.47	+0.01	+0.10	0.04
Al I	13	4	6.14	−0.33	−0.31	+0.23	+0.25	0.04	10	6.15	−0.32	−0.30	+0.25	+0.27	0.02	6.15	−0.32	−0.30	+0.25	+0.27	0.04
P I	15	2	5.14	−0.31	−0.27	+0.25	+0.29	0.06	0	−	−	−	−	−	−	−	−	−	−	−	−
K I	19	6	4.81	−0.31	−0.22	+0.25	+0.34	0.07	2	4.80	−0.32	−0.23	+0.25	+0.34	0.08	4.81	−0.31	−0.22	+0.26	+0.35	0.11
Sc I	21	2	2.66	−0.51	−0.49	+0.05	+0.07	0.04	20	2.65	−0.52	−0.50	+0.05	0.07	0.03	2.65	−0.52	−0.50	+0.05	+0.07	0.05
Sc II	21	0	−	−	−	−	−	−	18	2.71	−0.46	−0.44	+0.11	+0.13	0.04	−	−	−	−	−	−
Y I	39	0	−	−	−	−	−	−	1	1.51	−0.73	−0.70	−0.16	−0.13	0.10	−	−	−	−	−	−
Y II	39	1	1.51	−0.73	−0.70	−0.17	−0.14	0.08	5	1.56	−0.68	−0.65	−0.11	−0.08	0.06	1.54	−0.70	−0.67	+0.13	+0.10	0.10
Ce II	58	6	1.06	−0.52	−0.52	+0.04	+0.04	0.04	4	1.04	−0.54	−0.54	+0.03	+0.03	0.05	1.05	−0.53	−0.53	+0.04	+0.04	0.06
Nd II	60	1	0.93	−0.57	−0.65	−0.01	−0.09	0.06	19	0.90	−0.60	−0.68	−0.03	−0.11	0.03	0.90	−0.60	−0.68	−0.03	−0.11	0.07
Dy II	66	1	0.70	−0.44	−0.40	+0.12	+0.16	0.05	1	0.68	−0.46	−0.42	+0.11	+0.15	0.05	0.69	−0.45	−0.41	+0.12	+0.16	0.07

On average these errors amount to a few hundredths of a dex at most. The only notable exception is the higher sensitivity of OH and HF lines to the effective temperature: indeed a variation of ± 33 K implies an error in the derivation of Oxygen and Fluorine abundances of ± 0.06 and ± 0.07 dex, respectively.

In the computation of these errors we did not include the inter-dependence between the C, N, O abundances contributing to the formation of the measured molecular lines, nor the influence of the abundances of the main electron donors on those derived from ionized species. We estimated that these effects normally yield errors below 0.1 dex (see also e.g. Ryde et al., 2009).

Measurement errors include uncertainty in the continuum positioning and photon noise. For elements with more than two measurable lines, we computed the dispersion around the mean abundance, while for those with one or two measurable lines, we computed the dispersion from a Monte-Carlo simulation, taking into account an error in the measured EW of $\approx \pm$ FWHM/SNR for a line FWHM sampled with 2-3 pixels.

The measurement errors ϵ quoted in Table 4.4 are the σ dispersion divided by the square root of the number of used lines.

In the course of the chemical analysis we checked a few problematic lines against possible NLTE effects by using the online web tool[†].

Abundances and corresponding measurement errors for all the sampled chemical elements in the $\log(N_X/N_H)+12$ and in the [X/H] solar scales, adopting as solar reference both Grevesse & Sauval (1998) (Gre98) and Asplund et al. (2009) (Aspl09), are listed in Table 4.4. In Fig. 4.7 we compare the derived abundances from NIR and optical lines for all the measured elements.

4.2.1   CNO and Fluorine

In our chemical analysis of Arcturus we first computed the abundances of CNO and then those of the other elements. Indeed, CNO are the most abundant metals and in red giant and supergiant star spectra the many molecular CO, CN and OH lines are the most important potential contaminants. Following Ryde et al. (2009) and Smith et al. (2013), we adopted an iterative method to derive CNO abundances, in order to consider the interplay among these three elements in setting the molecular equilibrium. The resulting abundances are listed in first three lines of Table 4.4. Most interestingly, the Carbon abundance derived from the Δv=3 CO band-heads visible in the H-band, is 8.02 and equal within the errors with the values derived

---

[†]http://nlte.mpia.de/gui-siuAC_secE.php, M. Kovalev et al. 2018
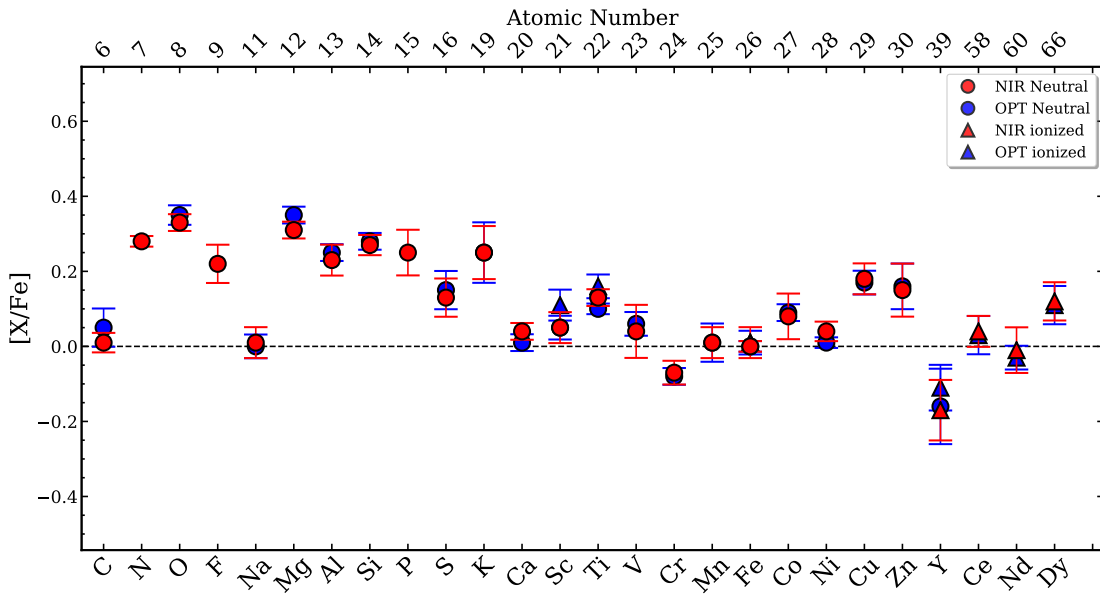
Figure 4.7: Derived [X/Fe] chemical abundances for Arcturus from the GIANO-B NIR spectrum (red symbols) and UVES optical spectra (blue symbols). The circles indicate the neutral species, while the triangles indicate the ionized species. Errorbars are from Table 4.4.
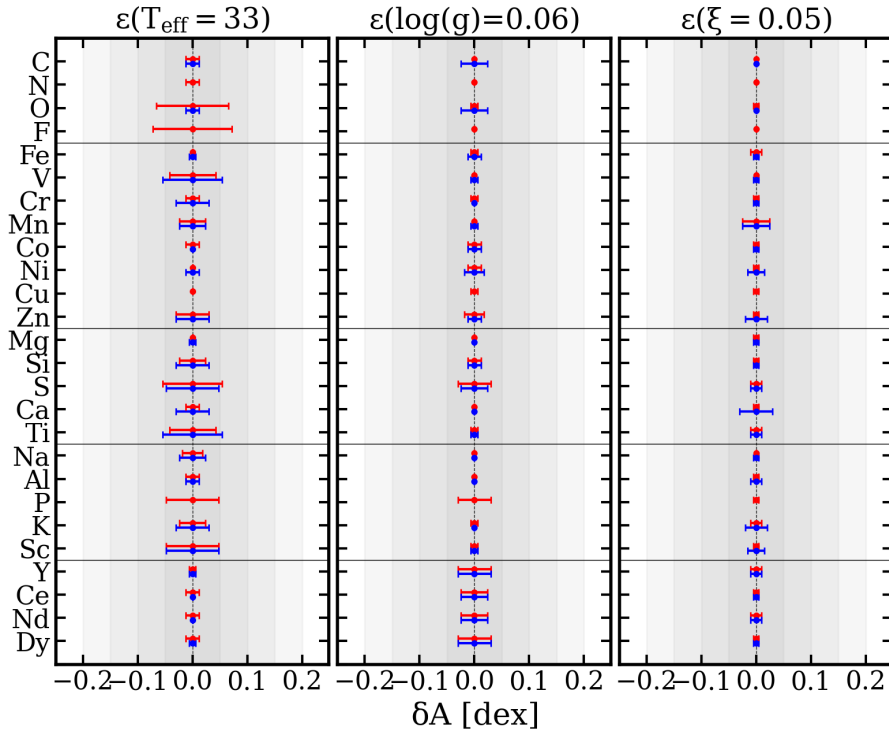
Figure 4.8: Abundance errors due to stellar parameters for optical (blue) and NIR (red) analysis.

from atomic C I lines and isolated CO roto-vibrational transitions.

This result indicates that the $\Delta v=3$ CO band-heads could be effectively used to measure Carbon abundances in cold stars where the single CO lines are severally blended or too weak for reliable abundance analysis.

Following a similar approach, we estimated the abundance of ^{13}C using two $\Delta v=3$ and three $\Delta v=2$ band-heads of ^{13}CO. This yielded a ^{12}C/^{13}C isotopic abundance ratio of 7 ± 1, consistent with the effects of the 2nd dredge-up coupled to some extra mixing in low mass giants (see e.g. Charbonnel & Lagarde, 2010).

The Fluorine abundance was derived from one HF molecular line at 23358.33 Å in the K band, using the transition parameters of Jönsson et al. 2014.

4.2.2   Iron-peak elements

The Iron abundance was derived for more than 400 lines of Fe I, and a dozen of Fe II lines. Fully consistent values were obtained from all these line sets, with a σ dispersion of about 0.1 dex. We adopted the average value of 6.93 ± 0.01 (see Table 4.4) as the reference iron abundance of Arcturus. However, it is interesting to note that many of the lines in the YJ bands provide abundances that are systematically lower (on average by 0.04 dex) than the reference abundance. We inspected some of these lines for possible NLTE effects, indeed finding that some positive corrections of ≤ 0.1 dex should be applied to their LTE abundances.

For the other Iron-peak elements, we could also measure both optical and NIR lines, as listed in Tables in appendix A, and derive suitable abundances. In particular, for Chromium and Nickel, we used a few tens lines both in the optical and NIR range. For Vanadium we used a few tens lines in the optical with hyperfine splitting (hereafter HFS) and only a few in the NIR. For Manganese we used the few measurable lines both in the optical and NIR. In particular, in the NIR we used the J band lines at 13218.49 Å and 13415.64 Å that need a NLTE correction of $\Delta A(\text{Mn}) = -0.16$ and $\Delta A(\text{Mn}) = -0.04$, respectively, and two lines in the H band with HFS. For Cobalt we used a few tens optical lines with HFS and a few NIR lines. The latter show a larger scatter that can be explained with small NLTE effects. Indeed, for example, we applied a NLTE correction of $+0.06$ dex to the LTE abundance of the 16757.64 Å line. For Copper we could only use one optical and one NIR line. The NIR line at 16005.75 Å has HFS and needs to be used with caution since potentially blended. For Zinc we used one line in the optical and two in the NIR. The NIR line at 11054.28 Å is partially blended with CN, while the one at 13053.63 Å is free from contamination.

Altogether, the iron-peak elements show fully consistent optical and NIR abun-

dances. They homogeneously scale as Iron, with the possible exception of Copper and Zinc that are slightly enhanced.

4.2.3 α elements

Dozens of unblended lines of Si I, Ca I, Ti I, Mg I and S I are available in the NIR spectrum of Arcturus for abundance analysis. NIR Mg I and S I lines are known to suffer of NLTE effects (Takeda et al., 2016; Zhang et al., 2017). However, at the metallicity, temperature and gravity of Arcturus, the corrections turn out to be negligible. In case of Sulphur there is also a forbidden line [S I] at 10821 Å that provides a fully consistent abundance with the one derived from the selected S I lines, further proving that NLTE effects are negligible.

The inferred NIR abundances for these alpha elements are fully consistent with the optical ones, as detailed in Table 4.4 and shown in Fig. 4.7.

The derived abundances of Mg and Si and to a lower extent of Ti, S and Ca suggest some [α/Fe] enhancement, as for Oxygen, and typical of thick-disk stars.

4.2.4 Z-odd elements

A few optical and NIR lines of Na, K and Sc can be safely used to derive reliable abundances. We found consistent optical and NIR solar-scaled abundances of Na and Sc and some enhanced K abundance. However, the K lines can suffer by significant NLTE effects with negative corrections to the LTE abundances (see.g. Osorio et al., 2020; Zhang et al., 2006), thus implying a lower [K/Fe] relative abundance, about solar or even sub-solar scaled. Two NIR lines of Phosphorus at 10529.52 Å and 10581.58 Å are also measurable, giving an abundance of 5.14 ± 0.08. A third line at 10596.90 Å gives a unexpected larger abundance (see also Maas et al., 2017), probably blended since its profile is clearly asymmetric, hence we rejected it.

Concerning Aluminium, ten optical lines and four NIR lines at 10782.05 Å, 10768.37 Å, 10872.97 Å and 10891.77 Å in the Y band with small (if any) NLTE corrections provide homogeneous abundances enhanced by almost a factor of two with respect to the solar-scaled value. For the NIR lines we used log(gf) from NIST, that are slightly different from those adopted in VALD3.

The strong lines at 13123.41 Å and 13150.75 Å and the K band line at at 21163.76 Å have HFS and suffer of significant NLTE effects (Nordlander & Lind, 2017) and require negative abundance correction of $0.25 - 0.30$ dex.

Although once corrected for NLTE, these lines provide Al abundances reasonably consistent with those of the Y band and optical lines, we did not used them.

The three strong lines at 16718.96 Å, 16750.56 Å and 16763.36 Å also suffer of NLTE effects and have HFS. The line at 16750.56 Å has also strong and blended wings.

In Arcturus-like stars abundances derived from these lines can be quite uncertain, hence we did not use them (see Sect. 4.2.6).

4.2.5   Neutron-capture elements

We measured NIR lines for five neutron-capture elements, namely Yttrium (mostly an s-process element), Cerium (an s-process element), Neodimium (mostly an s-process element) and Dysprosium (an r-process element). NIR Ce II and Nd II lines were identified for the first time by Cunha et al. (2017) and Hasselquist et al. (2016), respectively.

One neutral and five ionized lines of Yttrium were measured in the optical, while only one ionized line is measured in the NIR Y band (see also Matsunaga et al., 2020). We find an Y abundance slightly depleted with respect to the solar scale value, in agreement with the disk chemistry at the Arcturus metallicity (see e.g. Bensby et al., 2014; Reddy et al., 2006).

We finally used a few optical and NIR ionized lines of Cerium, Neodymium and Dysprosium and we derived about solar-scaled Ce and Nd abundances and slightly enhanced Dy with respect to the solar-scaled value.

4.2.6   Chromospheric activity

We noticed that some strong lines in the GIANO-B spectrum are deeper than the corresponding lines in the FTS winter and summer spectra of Arcturus by Hinkle et al. (2000). A few examples are shown in Fig. 4.9.

Chromospheric activity can fill the core of strong lines and mimic shallower absorptions (e.g. Shcherbakov et al., 1996). We thus wonder if a variation for the chromospheric activity in Arcturus could be responsible of the different line depth in the GIANO-B and FTS spectra.

To this purpose, we used the He I line at 10830 Å that is a good indicator of chromospheric activity (Danks & Lambert, 1985). As shown in Fig. 4.9 when the winter and especially the summer FTS spectra were acquired chromospheric activity was higher as suggested by the presence of some He I emission and shallower photospheric lines, while when the GIANO-B spectrum was acquired activity was low, without He I emission and with deeper photospheric lines. Hence, given that strong lines can be problematic also because potentially weakened by such a chro-
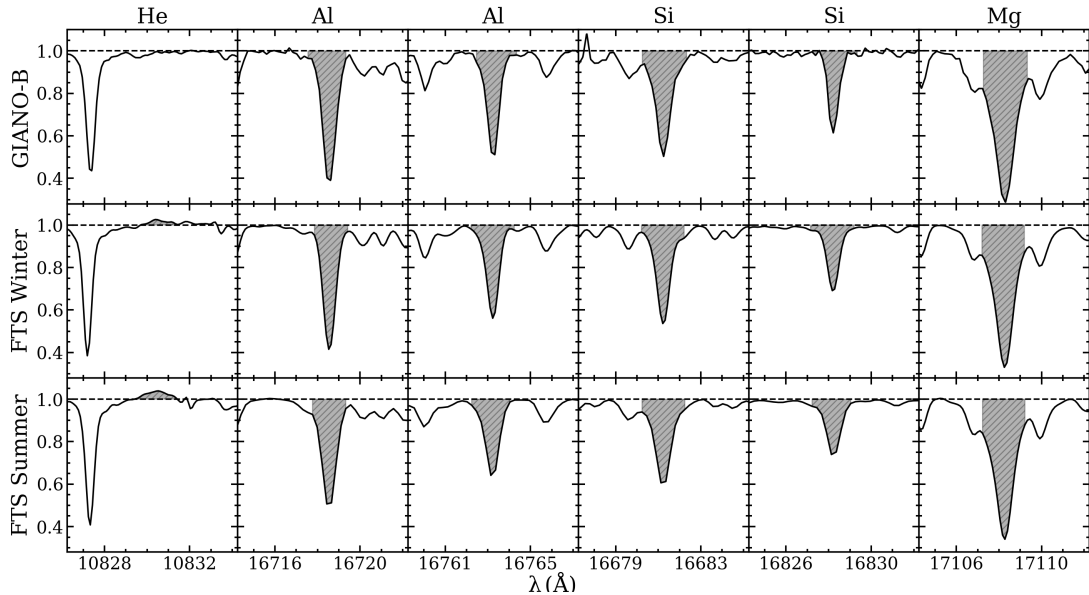
Figure 4.9: Chromospheric He I line in the Y band and a few strong photospheric Al, Si and Mg lines in the in the GIANO-B spectrum (top panel) and in the winter (middle panel) and summer (bottom panel) FTS spectra by Hinkle & Wallace (2005).

mospheric activity, they should be used with great caution for abundance analysis. We excluded these lines from our abundance analysis.

4.3   Lesson learned

The value of the combined optical and NIR study of Arcturus presented in this chapter is multifold and can be summarised as follows.

i) it maximizes the set of diagnostic lines to sample almost all the chemical elements of interest and with a statistically significant number of lines for most of them;

ii) it enables to sample lines of a given species at different wavelengths, extending the range of excitation potentials and transition probabilities for a better understanding of the physics of line formation and the modeling of the observed spectrum;

iii) it drives the analysis towards a physical, self-consistent solution over the entire spectrum of the degeneracy problem among stellar parameters and chemical abundances.

Taking advantage of our optical and NIR analysis, *i*) we could set an optimal
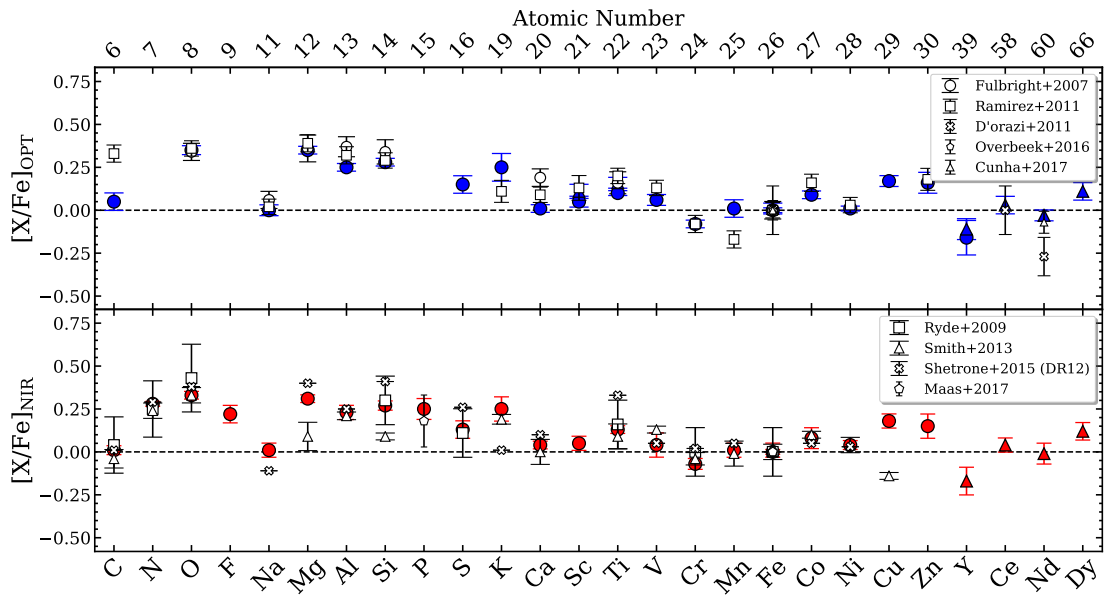
Figure 4.10: Derived [X/Fe] (Grevesse & Sauval, 1998) chemical abundances for Arcturus from some optical (top panel) and NIR (bottom panel) studies quoted in Table 4.1. Blue symbols are our abundances from the optical UVES spectra, red symbols our abundances from the NIR GIANO-B spectrum. Blue and red dots refer to neutral species, blue and red triangle to ionized species.

value for the microturbulence velocity that works over the full spectral range from 4800 to 24500 Å and *ii*) we could define a new spectroscopic thermometer and new spectroscopic gravitometer for cool giants, based on atomic and NIR molecular diagnostics of Carbon and Oxygen abundances, as detailed in Sect. 4.3 and Figs.4.4 and 4.6. By using these diagnostic tools we infer a temperature and gravity for Arcturus that are fully consistent with photometric estimates and with the values obtained from the standard tools used in optical spectroscopy (see Figs. 4.5 and 4.6).

As discussed in Sect. 5.2 and shown in Fig. 4.7 for all the analyzed elements we find fully consistent optical and NIR abundances. This demonstrates that *i*) the current generation of NIR echelle spectrographs is fully adequate to get high quality data for quantitative spectroscopy as in the optical; *ii*) the available atomic and molecular data for the NIR lines are generally accurate enough for reliable chemical abundance analysis.

Carbon, Sodium, Potassium and Iron-peak elements (with the exception of Copper and Zinc that are slightly enhanced) are consistent with solar-scaled values, with abundances between one fourth and one third solar. Nitrogen, Oxygen, Fluorine, and alpha elements (with only exception of Ca which is about solar-scaled), are enhanced by a few tenth of a dex with respect to the corresponding solar-scaled

values. The values inferred for [F/O] and [F/Fe] agree with literature values for thick-disk giant stars of similar metallicity (see, e.g. Grisoni et al., 2020, their figure 2). Among the neutron-capture elements, Cerium and Neodymium are about solar-scaled; Dysprosium is slightly enhanced, while Yttrium is slightly depleted with respect to the corresponding solar-scaled values.

Our inferred stellar parameters and chemical abundances are normally fully consistent with those obtained in previous optical or NIR studies, as shown in Fig. 4.10. We stress here that abundance differences of a few hundredths dex among different studies is something intrinsic to the analysis process, since different studies may use different codes, model atmospheres and/or line lists and transition probabilities as well as some different assumptions for the stellar parameters.

In particular, when comparing our optical abundances with those obtained by Ramírez & Allende Prieto (2011) we found some notable discrepancies only for C and Mn abundances. They determined C abundance from four C I lines. In our analysis we rejected those lines since the two at 9078 Å and 9111 Å are affected by NLTE and the other two at 8335 Å and 5380 Å AA are blended. We thus used only the forbidden line at 8727 Å. As discussed in Sect. 4.1.1 our [C I] abundance is fully consistent with the C abundance derived from CO and C I lines in the H band.

Regarding Mn, they mostly measured blue lines not present in our UVES spectrum, while we measured lines in the red part of the optical spectrum. As discussed in Sect. 4.2.2, our optical Mn abundance is fully consistent with our NIR estimates and the values obtained in other NIR studies.

It is also interesting to compare our results on stellar parameters and iron abundances to those obtained by the NIR studies of Kondo et al. (2019) in the in the $9300 - 13100$ Å spectral range and of Smith et al. (2013) in the $15000 - 17000$ Å spectral range at about half the spectral resolution of our study.

Kondo et al. (2019) used a standard temperature and gravity but a microturbulence velocity of 1.2 km s^{-1}, lower than any previous study and also lower than our adopted value of 1.6 km s^{-1}. They also used two different line list, VALD3 and the one by Meléndez & Barbuy (1999) (hereafter MB99). 48 lines in our list are in common with Kondo et al. (2019) VALD3 line list. Our and Kondo et al. (2019) VALD3 abundances are similar, despite we adopted a 0.4 km s^{-1} higher microturbulence velocity.

The other 20 lines in the Kondo et al. (2019) VALD3 line list have not been used in our analysis since blended or contaminated by nearby strong photospheric or telluric lines. These rejected lines give an average abundances that is off by more

than 0.1 dex and with a significantly larger (>0.2 dex) dispersion.

At variance, we used other 30 lines in the YJ bands that are not in the VALD3 Kondo et al. (2019) line list and, on average, provide abundances a few hundredths dex higher than those from the the lines in common.

As a result, our average VALD3 iron abundance from our selection of YJ band lines is 0.08 dex higher than in Kondo et al. (2019) and only a few hundredths dex lower than our reference abundance from the full set of optical and NIR lines. As mentioned in Sect. 4.2.2, correction for NLTE effects can significantly mitigate if not solve the problem.

If we use the MB99 astrophysical $log(gf)$, that are given for lines in the $10,000-18,000$ Å range and, on average, lower by 0.2-0.3 dex with respect to those in VALD3, we find corresponding larger abundances.

When compared to the iron abundances obtained in previous optical studies (see Table 4.1) and also in the present one, the abundances from the MB99 $log(gf)$ are in excess by more than 1σ in the YJ band and more than 2σ in the H band. If we also use the lower microturbulence velocity of Kondo et al. (2019) we get even larger and unlikely iron abundances.

Smith et al. (2013) used a microturbulence velocity of 1.85 km s^{-1} and nine H band lines with astrophysical $log(gf)$ calibrated on the Sun and Arcturus IR FTS spectra by Livingston & Wallace (1991) and Hinkle & Wallace (2005), respectively. Their $log(gf)$ values are somewhat in between those of VALD3 and MB99. In our analysis we used 84 H band lines. Five out of the nine lines listed by Smith et al. (2013) are in common with our sample. The other four lines in Smith et al. (2013) list have been rejected since problematic (i.e. partially blended and/or with strong wings). Our and their average abundances from the five lines in common are very similar. Indeed, the lower $log(gf)$ values used by Smith et al. (2013) are somewhat compensated by their slightly larger microturbulence velocity. The slightly revised iron abundance in Shetrone et al. (2015) study is practically coincident with our estimate.

The problem of the non-perfect modeling of a line is highly degenerate. Indeed, a given variation in the abundance from a given line can be obtained by modifying its log(gf) but also by slightly varying the stellar parameters, and/or by using different prescriptions for the damping, HFS, NLTE corrections, etc. That degeneracy (see also e.g. Takeda, 1992) cannot be easily removed.

The astrophysical calibration of the log(gf) is becoming very popular. However, such a calibration is model dependent (i.e. it depends on the adopted model atmospheres, spectral code, used lines etc.) and it also depends on the calibrator

itself, i.e. on the selected star, observed spectrum as well as on the adopted stellar parameters. Hence, none of the proposed astrophysically calibrated log(gf) can be safely adopted in studies that use recipes and tools for chemical analysis that are different from those used for the astrophysical calibration.

Our combined optical and NIR analysis shows that it is not necessary to systematically tune the log(gf) of the NIR lines in the VALD3 database to get reliable abundances, if the appropriate set of lines is chosen and self-consistent stellar parameters are derived.

Chapter **5**

The young stellar populations of the Perseus complex

The full characterisation of the young stellar populations in recently formed star clusters and associations within the Galaxy is of paramount importance to answer a number of open questions concerning the formation and early evolution of star clusters and associations, as well as the recent star formation and chemical enrichment history of the Milky Way disc.

Most stars in galaxies form on hierarchical scales as groups, associations and clusters, spending part of their lives gravitationally bound to each other while still within their progenitor molecular cloud (Lada & Lada, 2003; Portegies Zwart et al., 2010). Normally, within young associations and clusters, younger stars tend to be clustered on smaller (a few parsecs) and denser scales than older stars that are more dispersed and on larger scales (up to hundreds of parsecs; Elmegreen & Hunter, 2010).

The Gaia mission of the European Space Agency (Gaia Collaboration et al., 2016) is opening a new perspective in identifying and kinematically characterizing substructures in the inner and outer disc of the Galaxy. Follow-up spectroscopic observations at medium-high resolution provide complementary information on the
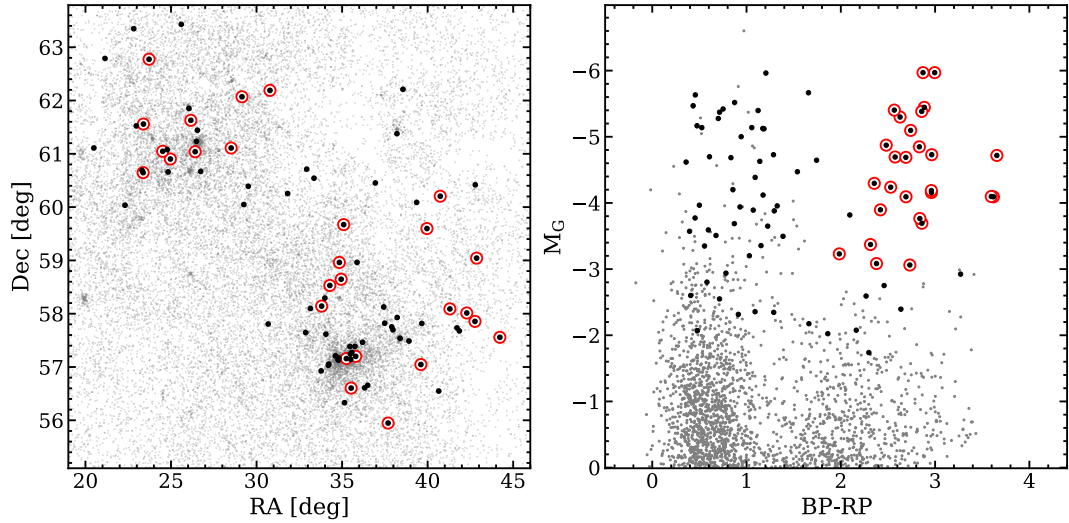
Figure 5.1: Left panel: RA-Dec map of the stars likely members of the Perseus complex young clusters and associations (grey dots), based on their distances and proper motions, within a projected area of about 10 degrees on sky. Black dots mark the 84 stars spectroscopically observed within the TNG-SPA Large Program, while red circles mark the 27 RSGs studied in this paper. Right panel: Gaia EDR3 color magnitude diagram (CMD) for the same stars in the left panel.

detailed chemistry and line-of-sight radial velocities (RVs) of those regions.

The Perseus complex at a Galactocentric distance of about 10 kpc hosts a number of young star clusters and associations, the densest structures being h,χ Per, NGC 457, NGC 654 and NGC 633, distributed within a projected area of approximately 10 degrees on sky. This region offers a unique opportunity to study the recent star formation and cluster assembling processes in the outer disc.

Recently de Burgos et al. (2020) provided a comprehensive kinematic study of the young Perseus OB-1 association, by combining Gaia DR2 and high resolution optical spectroscopy, finding that most of the sampled blue and red supergiants located at d$\approx$2.5$\pm$0.4 kpc share a common kinematics and are physically linked.

However, the detailed chemistry of this region is poorly constrained and only a few measurements exist so far. High resolution optical spectra for five B-type stars members of NGC 457 (Dufton et al., 1994) provided carbon, oxygen, magnesium and silicon abundances, indicating sub-solar values of about -0.3 dex, with the only exception of oxygen which resulted enhanced by about 0.2 dex.

A photometric estimate of about solar metallicity for the h,χ double cluster has been suggested by Currie et al. 2010. However, photometric estimates of metallicity in general, and especially in the case of very young stellar populations, should be regarded only as indicative, since isochrone fitting is not sufficiently sensitive to

metallicity variations of a few tenths of a dex and it also depends on the adopted age/model. For 11 RSGS in the Perseus OB-1 associations, Gazak et al. (2014), by using global spectral synthesis of a portion of the J-band spectrum, obtained rather warm temperatures in the 3700-4100 K range and about solar metallicites.

Within TNG Large Program titled SPA - Stellar Population Astrophysics: the detailed, age-resolved chemistry of the Milky Way disk (Program ID A37TAC_13, PI: L. Origlia), that aims at measuring detailed chemical abundances and radial velocities of the luminous stellar populations of the the Milky Way thin disk and its associated star clusters (Origlia et al., 2019), we performed a combined optical and NIR spectroscopic screening at high resolution of the young stellar populations within the Perseus complex.

We observed 84 luminous blue and red young stars, candidate members of the Perseus complex, according to their Gaia distances and proper motions. For all these stars we derived very accurate radial and rotational velocities. For the 27 RSGs in the sample we also derived accurate stellar parameters and chemical abundances. Indeed, optical and NIR spectra of RSGs are very rich in absorption lines from many light and heavy metals of interest, enabling a detailed chemical screening of their pristine chemical composition as well as of possible modifications due to mixing processes in their interiors.

5.1   Kinematics of the young stars in the Perseus complex

The distributions of the Gaia EDR3 proper motions (PMs) in the RA-Dec plane for the 84 observed stars in the Perseus complex are shown in Fig. 5.2.
The total PM $= \sqrt{\mathrm{PM}^2_{\mathrm{RA}} + \mathrm{PM}^2_{\mathrm{Dec}}}$ distribution with values ranging between 0.4 and 1.9 mas yr^{-1}, provides an average PM of 1.2±0.03 mas yr^{-1} and a dispersion of 0.3±0.02 mas yr^{-1}. For the same stars heliocentric RVs in the range between -70 and -8 km s^{-1} have been measured, with an average value of -42.7±0.8 km s^{-1} and a dispersion of 7.7±0.6 km s^{-1}.

  Fig. 5.3 shows the inferred total proper motions *versus* the RVs and the corresponding distributions. The RV distribution is more peaked and more symmetric than the PM one, indicating that motions are quite homogeneous in the radial direction while in the plane there is some sub-structuring, possibly due to clustering. For the sub-sample of 46 stars warmer than T$_{eff}$ ≳7000 K we have been also able
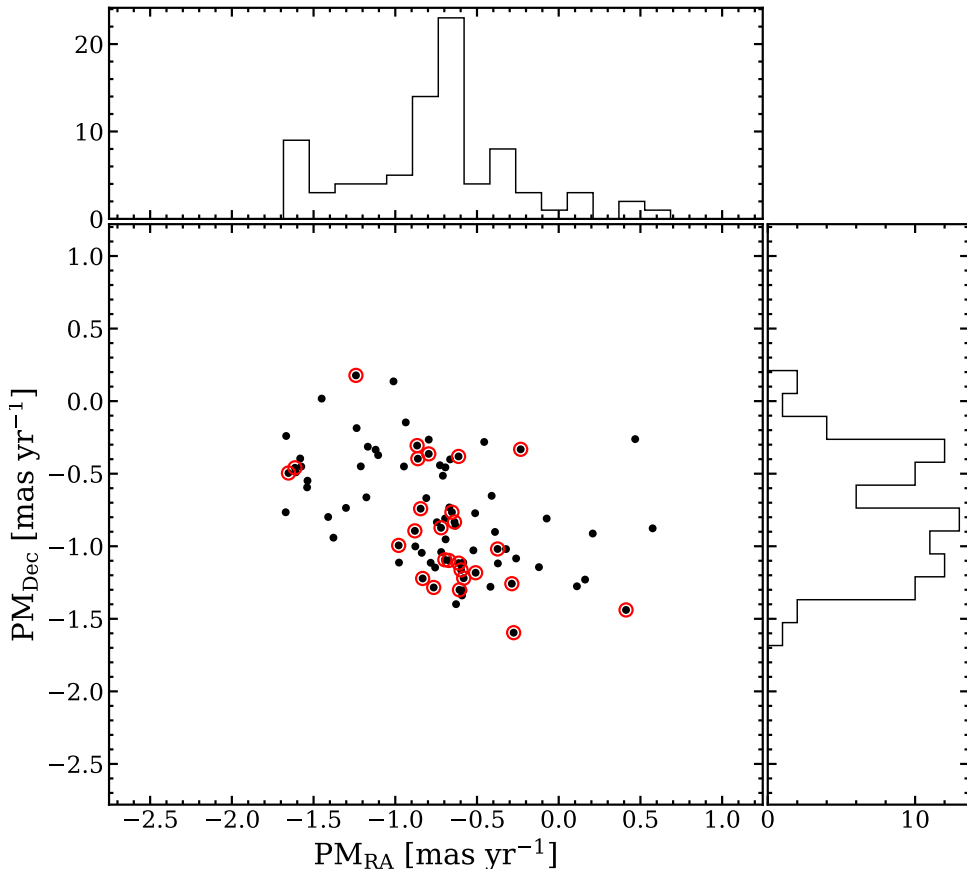
Figure 5.2: Gaia EDR3 PMs in the RA-Dec plane and corresponding histograms for the 84 observed stars in the Perseus complex (black dots). The sub-sample of 27 RSGs is also highlighted (red circles).

to measure the rotational broadening by using the Fourier transform (FT) method (see Sect. 3.1) on a few un-blended lines, under the assumption of a linear limb darkening law with a limb darkening coefficient of ϵ=0.6 (Reiners & Schmitt, 2002). Rotational velocities between 10 and 110 km s^{-1} have been measured.

According to their inferred luminosity, typically in the 10^4-10^5 solar luminosity range, and spectral types from SIMBAD, these warm/hot stars should be blue loop supergiants, with temperatures in the 7-20,000 K range and corresponding radii between a few hundreds and a few tens solar radii.

Fig. 5.4 shows the measured rotational velocities v $sini$ and corresponding histogram as a function of the star spectral type for the observed blue/yellow supergiants. The full range of measured rotational velocities is spanned by the stars with the earliest (O and early-B) spectral types, that is not substantially inflated, thus possibly reflecting the initial distribution of stellar rotations. Within this sub-sample of blue supergiants, $\approx$30% of stars are relatively slow (i.e. with v/v$_{crit}$ $\leq$0.1, corresponding
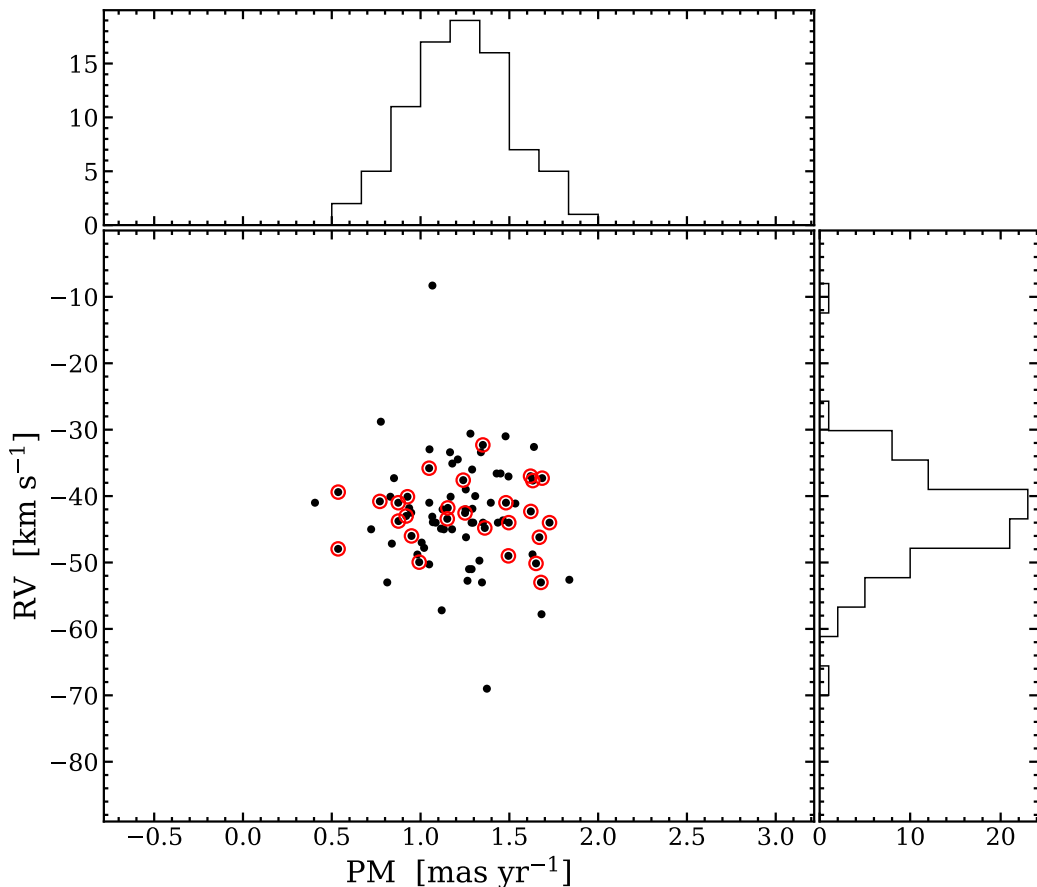
Figure 5.3: RVs *vs* Gaia EDR3 total PMs and corresponding histograms for the 84 observed stars in the Perseus complex (black dots). The sub-sample of 27 RSGs is also highlighted (red circles).
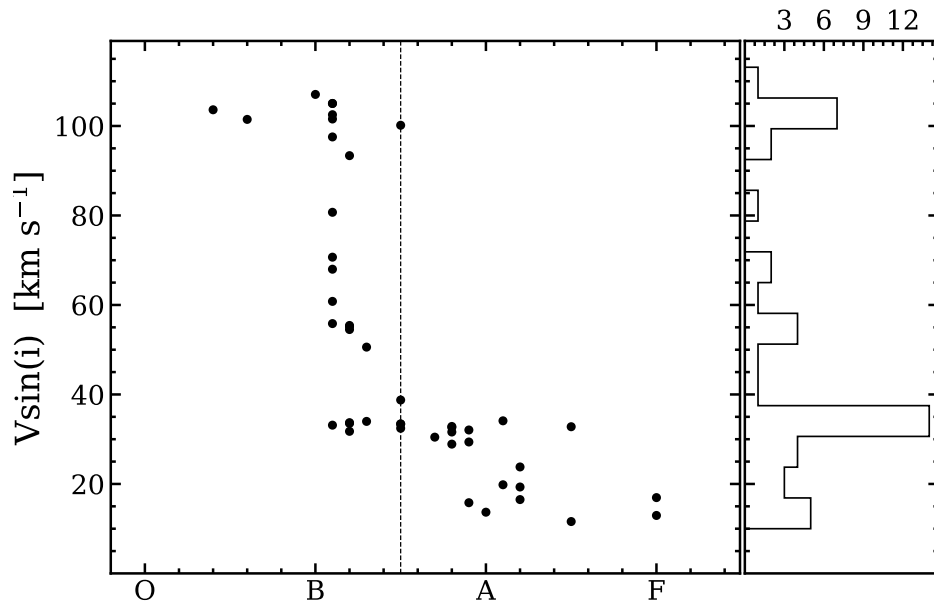
Figure 5.4: Rotational velocities as a function of the spectral type from SIMBAD for the observed sub-sample of blue supergiants in the Perseus complex. The vertical dotted line separates stars with spectral types earlier (left) and later (right) than B5.

to $vsin(i) \leq 50$ km s^{-1}) rotators. In this respect, Strom et al. (2005) provided rotational velocities in a sample of B0-B9 stars in h, χ Persei, with masses in the 4-15 M$_\odot$, thus including both MS and evolved blue/yellow supergiants. Only four stars are in common with our sample. They used spectra at R$\approx$22,000 and derived rotational velocities, with an average $\approx$10% uncertainty, from the line broadening of optical He I and Mg II lines. Similarly to what found in our study, only a small fraction of stars are slow rotators, the majority of them, either MS or more evolved giants and supergiants, are relatively fast rotators, in the 50-200 km s^{-1} range. Rotational velocities exceeding 200 km s^{-1} have been mostly measured only in dwarfs with masses below 9 M$_\odot$.

Stars in our sample with later (B5-9, A and F) spectral types, with likely lower temperatures and more expanded atmospheres, i.e. larger radii, are all slow rotators, in agreement with the momentum conservation principle.

Cooler RSGs and massive AGB with temperature well below $\approx$5000 K have even more expanded atmospheres and their broadening becomes quickly dominated by macroturbulence, while, according to the momentum conservation principle, rotation drops down to undetectable values.

For the observed stars Table 5.1 reports IDs, coordinates, Gaia EDR3 proper motions, parallaxes and photometry, radial and rotational velocities from the SPA Large Program spectra. Typical errors in the derived radial velocities are at most

1 km s^{-1} while for projected rotational velocities are within 1-3 km s^{-1}.

5.2   Physical and chemical properties of the RSGs in the Perseus complex

Stellar parameters for the observed RSGs in the Perseus complex are listed in Table 5.2. For each star, reddening has been estimated by interpolating the Schlegel et al. (1998) extinction maps and applying the corrections by Schlafly & Finkbeiner (2011). Bolometric luminosities have been estimated by using the de-reddened 2MASS K-band magnitudes, bolometric corrections as prescribed in Levesque et al. (2005). Effective temperatures have been obtained by minimizing the difference between carbon abundances derived from atomic C I and molecular CO lines, the so-called C-thermometer (see Sec. 4.1.1), with an average uncertainty of about $80-100$ K and a temperatures range between 3400 and 4200 K. These spectroscopic temperatures allow also the minimisation of any trend between iron abundances and excitation potentials of both the optical and NIR lines, as shown in Figure 5.5, although this diagnostic is only moderately sensitive at the low RSG temperatures. Surface gravities have been obtained by assuming an average stellar mass of 11 M$_{\odot}$, according to their young ages in the $15 - 30$ Myr range (see Currie et al., 2010; Dalessandro et al., 2021) and using eq. 3.1. We found log(g) values ranging from -0.40 to $+1.00$ dex, with an overall uncertainty of $\approx$ 0.15 dex. A variation of ± 2 M$_{\odot}$ for the adopted mass has little impact (less than 0.1 dex) on the derived gravity.

Microturbulence has been derived by using the standard approach of minimizing the slope between the iron abundance and the reduced EW of the measured lines. Values in the 2-4 km s^{-1} range have been obtained, with a typical uncertainty of $\sim$0.2 km s^{-1} (Fig. 5.6).

By using the inferred temperatures and bolometric magnitudes quoted in Table 5.2, we constructed the Hertzsprung-Russel (HR) diagram of Fig. 5.7. The location of the 27 RSGs here analyzed is qualitatively matched by theoretical evolutionary tracks of massive ($\gtrsim$9 M$_{\odot}$) stars, as e.g. those from the PARSEC models (Bressan et al., 2012), although it seems that the latter can reach sufficiently high luminosities and low temperatures to match the location of the coolest RSGs only after the He-core burning, that is during the faster phases of shell He-burning or core C-burning.

Table 5.1: IDs, RA, Dec, Gaia EDR3 PM, parallax, photometry, RVs and projected rotational velocities for the observed stars in the Perseus complex.

ID	star	RA	Dec	PM$_{RA}$	PM$_{Dec}$	parallax	G	BP	RP	RV	v sin(i)
		deg		mas yr^{-1}		mas				km s^{-1}	
P1	SU Per	35.528722	56.604131	-0.764940	-1.284087	0.416842	5.93	7.70	4.71	-49.00	0.00
P2	10 Per	36.316781	56.609815	-0.508466	-1.182499	0.442422	6.14	6.30	5.84	-43.42	55.17
P3	HD 14433	35.480976	57.242911	-0.581347	-1.219964	0.450917	6.21	6.57	5.69	-43.66	19.82
P4	HD 13267	32.871634	57.645542	-0.653379	-0.765238	0.524263	6.26	6.46	5.93	-34.48	33.41
P5	HD 13854	34.215479	57.055240	-0.611815	-1.116347	0.429048	6.37	6.53	6.10	-43.93	70.68
P6	HD 14134	34.768547	57.135494	-0.672723	-1.097664	0.434804	6.44	6.70	5.99	-41.91	33.98
P7	HD 14143	34.808087	57.169226	-0.591378	-1.339120	0.411042	6.51	6.79	6.04	-52.75	50.58
P8	HD 15497	37.972397	57.697637	-0.322443	-1.019456	0.370487	6.76	7.24	6.11	-44.80	30.46
P9	HD 14542	35.751769	57.387001	-0.719178	-1.039813	0.438911	6.79	7.17	6.22	-48.78	31.61
P10	FZ Per	35.248517	57.158318	-0.783403	-1.113813	0.370283	6.86	8.30	5.67	-44.00	0.00
P11	HD 15316	37.493983	57.820709	-0.389775	-0.901480	0.390141	6.92	7.43	6.26	-48.80	16.51
P12	V439 Per	35.796103	57.199436	-0.522113	-1.028315	0.458097	7.00	8.43	5.86	-44.00	0.00
P13	HD 13841	34.193289	57.029347	-0.628184	-1.399108	0.413678	7.30	7.42	7.07	-41.78	54.51
P14	HD 13744	33.994564	58.293614	-0.877534	-1.001197	0.404561	7.34	7.82	6.68	-47.16	15.81
P15	V550 Per	33.805399	58.142306	-0.669257	-0.732617	0.350906	7.58	9.10	6.41	-47.00	0.00
P16	PP Per	34.284290	58.529706	-0.977319	-1.112538	0.417423	7.74	9.48	6.52	-51.00	0.00
P17	HD 15690	38.386605	57.537425	-0.584009	-1.111900	0.447177	7.81	8.19	7.26	-42.31	55.42
P18	HD 14443	35.502397	57.144959	-0.597655	-1.163129	0.413029	7.95	8.14	7.64	-43.76	31.76
P19	HD 15620	38.220315	57.929345	-0.374079	-1.018650	0.421863	7.99	8.56	7.27	-42.54	32.64
P20	HD 16243	39.658666	57.816982	-0.417618	-1.279388	0.356374	8.04	8.39	7.53	-37.05	33.70
P21	HD 14052	34.617316	57.208368	-0.607213	-1.300560	0.421770	8.10	8.26	7.81	- 8.30	60.80
P22	BD+57 540	34.945796	58.646677	-0.410273	-0.652502	0.468253	8.28	9.51	7.19	-53.00	0.00
P23	BD+56 527	34.793528	57.130579	-0.692115	-0.952408	0.407938	8.36	8.57	7.98	-37.67	93.37
P26	HD 14422	35.461710	57.386563	-0.372202	-1.118325	0.372927	8.46	8.79	7.92	-41.81	102.52
P27	HD 14302	35.142196	56.329950	-0.582994	-1.304096	0.387312	8.49	8.62	8.23	-41.12	80.71
P28	HD 13659	33.777066	56.926520	-0.756222	-1.146514	0.393302	8.52	8.77	8.10	-32.96	33.14
P29	HD 15406	37.690456	55.944114	-0.511390	-0.772355	0.415356	8.68	9.69	7.70	-51.00	0.00
P30	HD 15266	37.431733	58.125222	-0.631589	-0.858661	0.420213	8.68	9.10	8.08	-49.72	13.69
P31	HD 14476	35.570651	57.271929	-0.832560	-1.221981	0.389598	8.70	8.86	8.31	-47.80	33.54
P32	HD 14870	36.495801	56.657906	-0.844929	-0.741204	0.668790	8.80	8.97	8.49	-50.14	97.55
P36	HD 236961	36.193054	57.464203	-0.880195	-0.893917	0.408014	9.01	9.31	8.53	-47.95	105.03
P37	HD 13784	34.053790	57.616172	-0.637617	-0.833017	0.520453	9.07	9.64	8.35	-37.60	16.95
P42	BD+56 525	34.788511	57.135087	-0.696711	-1.093535	0.400982	9.18	9.39	8.81	-49.95	101.56
P52	HD 236971	38.907649	57.487018	-0.286889	-1.257997	0.408809	9.39	9.66	8.95	-57.79	55.84
P54	BD+57 513	33.150279	58.098358	-0.979339	-0.994113	0.395671	9.41	9.55	9.14	-50.28	105.03
P61	BD+58 458	35.873129	58.963489	-0.745605	-0.834410	0.435709	9.49	9.85	8.94	-41.00	107.05
P63	2MASS J02024270+5748216	30.677959	57.806031	-0.838170	-1.045350	0.456308	9.53	10.33	8.66	-30.60	0.00
P64	2MASS J02313652+5745112	37.902227	57.753128	-0.260526	-1.084177	0.390878	9.68	10.14	9.05	-46.20	100.16
N5	2MASS J01570182+6002550	29.257544	60.048596	-1.120237	-0.334707	0.349388	9.89	11.37	8.73	-40.80	0.00
N6	HD 11831	29.515885	60.391091	-0.946939	-0.450234	0.322135	7.73	8.28	7.00	-36.60	23.80
N9	2MASS J01215808+6106357	20.492031	61.109969	-0.726664	-0.441899	0.329866	9.66	11.00	8.54	-35.80	0.00
N13	WX Cas	28.515568	61.109153	-1.176942	-0.662856	0.295469	8.46	10.17	7.21	-44.00	0.00
N18	HD 9167	22.968979	61.523579	-1.607984	-0.490408	0.373128	7.67	8.37	6.83	-45.00	12.96
N23	BD+62 246	21.142584	62.788709	-1.670575	-0.765829	0.339883	8.39	8.97	7.64	-52.60	38.76
N25	HD 10756	26.734947	60.669761	-1.010826	0.136084	0.289411	7.42	7.68	6.98	-37.30	28.90
N26	BD+60 327	26.411564	61.039665	-1.410662	-0.798302	0.318869	7.08	8.49	5.93	-46.00	0.00
N33	DO 24697	26.159728	61.628673	-1.378368	-0.940898	0.339657	8.58	10.21	7.37	-37.00	0.00
N35	BD+60 331	26.483806	61.234807	-1.104851	-0.372236	0.352103	8.62	9.15	7.92	-28.80	32.85
N36	BD+60 336	26.542574	61.442571	-1.240816	0.177363	0.368448	8.81	9.30	8.15	-32.30	29.38
N37	HD 10494	26.048389	61.849801	-1.211109	-0.449635	0.326479	6.76	7.55	5.89	-35.10	0.00
N41	HD 236946	31.818295	60.254210	-0.664519	-0.401359	0.355300	8.43	9.50	7.40	-36.60	0.00
N46	IRAS 01530+6149	29.149351	62.070327	-0.795284	-0.363602	0.247364	8.19	9.81	6.97	-45.00	0.00
N48	BD+61 369	30.784226	62.190011	-0.861983	-0.396643	0.382151	7.85	9.25	6.72	-44.00	0.00
N52	HD 10285	25.600511	63.429080	-1.450354	0.017442	0.294924	8.27	8.72	7.63	-69.00	11.60
N55	BD+62 272	23.717830	62.774669	-1.667531	-0.240076	0.344672	8.42	9.73	7.31	-45.00	0.00
N60	BD+59 274	23.371715	60.646584	-1.539454	-0.594270	0.345321	7.44	8.79	6.31	-45.00	0.00
N62	HD 9311	23.308343	60.686434	-1.301673	-0.735743	0.344024	7.15	7.33	6.85	-46.20	33.40
N66	BD+60 287	24.514955	61.047003	-1.653550	-0.495293	0.363885	7.90	9.16	6.81	-44.00	0.00
N67	HD 9973	24.779857	61.079092	-1.168157	-0.314038	0.313398	6.56	7.09	5.88	-33.40	0.00
N68	IRAS 01359+6024	24.830506	60.660651	-1.575298	-0.450831	0.340320	9.42	11.39	8.12	-53.00	0.00
N69	BD+60 299	24.965246	60.902292	-1.613748	-0.459418	0.329698	6.44	8.05	5.18	-44.00	0.00
N70	HD 9105	22.824957	63.347572	-0.810293	-0.668345	0.399289	7.31	7.64	6.80	-40.10	32.44
N71	BD+60 265	23.388188	61.558240	-1.537084	-0.548413	0.342733	7.23	8.79	6.05	-44.00	0.00
N72	HD 8906	22.313762	60.035667	-1.581792	-0.395387	0.399700	6.85	7.30	6.25	-43.10	0.00
AS3	IRAS 02476+5850	42.862918	59.042855	0.468010	-0.261664	0.308764	9.47	10.75	8.37	-31.00	0.00
AS4	YZ Per	39.605915	57.046160	-0.120893	-1.144047	0.417506	6.45	8.17	5.28	-43.00	0.00
AS9	IRAS 02389+5620	40.647867	56.548653	-0.073602	-0.809034	0.471020	9.56	10.69	8.52	-32.60	0.00
AS12	IRAS 02414+5752	41.300826	58.090110	0.574793	-0.876589	0.404778	8.27	9.93	7.07	-42.00	0.00
AS18	DO 26429	44.221750	57.556914	0.411963	-1.438901	0.405981	7.86	10.09	6.50	-42.00	0.00
AS19	HD 17088	41.714378	57.733797	0.208302	-0.912385	0.336350	7.25	7.75	6.57	-39.40	32.06
AS21	HD 17145	41.851031	57.677103	0.111377	-1.275963	0.415104	7.79	8.30	7.12	-40.10	34.11
AS22	HD 237006	42.286847	58.013449	-0.275705	-1.595608	0.406448	7.86	9.35	6.66	-39.00	0.00
AS23	V648 Cas	42.766450	57.855529	0.161402	-1.229690	0.474945	7.52	9.70	6.08	-41.00	0.00
IC3	GP Cas	39.960163	59.597581	-0.455881	-0.281408	0.368312	7.45	9.76	6.10	-44.00	0.00
IC4	BD+59 532	40.737416	60.204478	-0.866389	-0.306227	0.424286	8.80	10.35	7.62	-44.00	0.00
IC6	HD 17505	42.783226	60.417740	-0.695203	-0.809055	0.414680	7.21	7.41	6.81	-57.20	101.47
IC9	HD 17505A	39.358862	60.088438	-0.795259	-0.265214	0.786719	7.03	7.65	6.26	-33.40	0.00
IC14	HD 16088	36.943605	60.452751	-0.935894	-0.146592	0.479554	9.57	10.48	8.62	-53.00	32.79
IC17	HD 15570	38.205913	61.378354	-0.720136	-0.872716	0.442391	7.88	8.33	7.25	-42.50	103.62
IC24	IRAS 02304+6159	38.558113	62.210587	-0.232773	-0.331955	0.691273	9.06	10.29	7.99	-37.30	0.00
IC27	V605 Cas	35.093591	59.671360	-0.708831	-0.514053	0.330782	7.02	8.73	5.87	-36.00	0.00
IC30	2MASS J02132601+6032336	33.358386	60.542677	-0.693341	-0.456447	0.384439	9.48	10.66	8.40	-44.90	19.32
IC31	HD 13256	32.932952	60.712360	-0.612894	-0.381113	0.298858	7.98	8.81	7.06	-40.10	67.99
IC37	T Per	34.841144	58.961206	-1.236621	-0.185915	0.411877	7.20	8.88	5.92	-41.00	0.00

Table 5.2: Photometric information, derived stellar parameters and RVs for the studied RSGs.

#	ID	star	Gaia EDR3			2MASS	E(B-V)	$\log\left(\frac{L_{Bol}}{L_\odot}\right)$	T_{eff}	log(g)	ξ	RV
			G	BP	RP	K			[K]	[dex]	[km s^{-1}]	[km s^{-1}]
1	P1	SU Per	5.93	7.70	4.70	1.46	0.36	4.95	3466	-0.37	3.80	-49
2	P10	FZ Per	6.86	8.30	5.67	2.48	0.51	4.64	3750	0.07	3.10	-44
3	P12	V439 Per	7.00	8.43	5.86	2.69	0.55	4.44	3690	0.25	3.40	-44
4	P15	V550 Per	7.59	9.10	6.41	3.19	0.74	4.62	3720	0.08	3.30	-47
5	P16	PP Per	7.74	9.48	6.52	2.95	0.78	4.50	3670	0.18	3.00	-51
6	P22	BD+57 540	8.28	9.51	7.19	4.28	0.68	4.18	4125	0.70	2.10	-53
7	P29	HD 15406	8.68	9.69	7.71	5.15	0.40	3.96	4190	0.95	2.00	-51
8	AS4	YZ Per	6.45	8.17	5.28	1.91	0.62	4.85	3616	-0.20	4.00	-43
9	IC37	T Per	7.19	8.88	5.91	1.94	0.84	4.63	3594	0.01	3.30	-41
10	IC3	GP Cas	7.45	9.76	6.10	1.95	1.07	4.74	3471	-0.16	3.40	-41
11	N69	BD+60 299	6.44	8.05	5.18	2.11	0.75	5.05	3491	-0.45	3.40	-44
12	AS23	V648 Cas	7.52	9.70	6.08	2.25	1.27	4.87	3572	-0.24	3.50	-41
13	AS18	DO 26429	7.86	10.09	6.49	2.48	1.49	4.94	3578	-0.30	3.50	-42
14	IC27	V605 Cas	7.02	8.73	5.87	2.58	0.82	4.95	3736	-0.24	3.10	-36
15	N71	BD+60 265	7.23	8.79	6.05	2.63	0.88	4.61	3637	0.06	3.20	-41
16	N26	BD+60 327	7.08	8.49	5.93	2.93	1.26	4.58	3778	0.15	3.00	-46
17	AS22	HD 237006	7.86	9.35	6.66	3.12	1.10	4.40	3863	0.37	2.80	-39
18	N60	BD+59274	7.44	8.79	6.31	3.12	0.51	4.62	3740	0.09	2.80	-45
19	N13	WX Cas	8.46	10.20	7.24	3.41	1.88	4.50	3787	0.23	3.00	-44
20	AS12	IRAS02414+5752	8.27	9.91	7.07	3.56	0.89	4.42	3850	0.34	2.60	-42
21	N46	IRAS01530+6149	8.19	9.81	6.97	3.74	1.04	4.49	3793	0.25	2.60	-45
22	N48	BD+61 369	7.85	9.25	6.72	3.78	1.06	4.24	3869	0.53	2.60	-44
23	N33	DO 24697	8.58	10.21	7.37	3.87	1.62	4.29	3896	0.50	2.40	-37
24	N66	BD+60 287	7.90	9.16	6.81	3.98	0.73	4.04	4009	0.79	2.50	-44
25	N55	BD+62 272	8.42	9.73	7.31	4.20	1.18	4.34	3925	0.46	2.40	-40
26	IC4	BD+59 532	8.80	10.35	7.62	4.20	1.08	4.14	4016	0.69	2.40	-44
27	AS3	IRAS02476+5850	9.47	10.75	8.37	5.28	0.99	3.94	4048	0.91	2.30	-31

From the 27 RSGs here analyzed, an average [Fe/H]=-0.30 ± 0.01 dex with a dispersion σ=0.03 $\pm$0.01 dex has been measured. Such an average half-solar iron abundance fits within the metallicity distribution of older dwarf and giant stars (see e.g. Hayden et al., 2014; Mikolaitis et al., 2014, 2019; Reddy et al., 2003) at a similar galactocentric distance of about 10 kpc, which may imply inflows of metal poor gas as the origin of the sub-solar metallicity in such a young stellar population.

The line profiles of the observed stars are broader than the instrumental line profile and likely due to macroturbulence velocities in the $8 - 13$ km s^{-1} range. As expected for these evolved stars, we did not find any appreciable line broadening due to stellar rotation.

Chemical abundances for 23 species have been derived from more than 200 atomic and molecular lines in the NIR. Their values and corresponding measurement errors are listed in Table 5.3 and 5.4.

Measurement errors quoted in Table 5.3 and Table 5.4 include uncertainty in the continuum positioning and photon noise and correspond to the 1σ dispersion divided by the square root of the number of used lines. For elements with more than two measurable lines, we computed the dispersion around the mean abundance, while for those with one or two measurable lines, we assumed an error of 0.1 dex. Abundance errors from uncertainties in the stellar parameters (see Sect. 3) were estimated by computing elemental abundances with varying T_{eff} by $\pm$100 K, log(g) by $\pm$0.15 dex, and ξ by $\pm$0.2 km s^{-1}. Typically, the impact of these uncertainties in the estimated abundances is within 0.10-0.15 dex for all the species with the exception of nitrogen from CN lines, for which it can raise to 0.2 dex.

In the computation of these errors we did not include the interdependence between the C, N, and O abundances that contribute to the formation of the measured molecular lines. We estimate that this effect yields abundance errors below 0.1 dex for C and O, while for N errors can be as high as 0.2-0.3 dex (see also Ryde et al., 2009). We also neglect the effect of the abundances of the main electron donors on those derived from ionised species. However, we estimate that this effect yields abundance errors below 0.1 dex for all the species.

Iron abundances were derived from 40-60 NIR lines of Fe I. The scatter from different lines is typically 0.15 dex. However, the dispersion in metallicity of the measured RSGs in the Perseus complex is significantly lower than the typical values of $0.15 - 0.20$ dex measured in the thin disc. Such a chemical homogeneity reinforces the suggestion by Dalessandro et al. 2021, based on the co-moving kinematics of the LISCA I stellar sub-structures, that we may have caught an ongoing process of hierarchical cluster assembly.
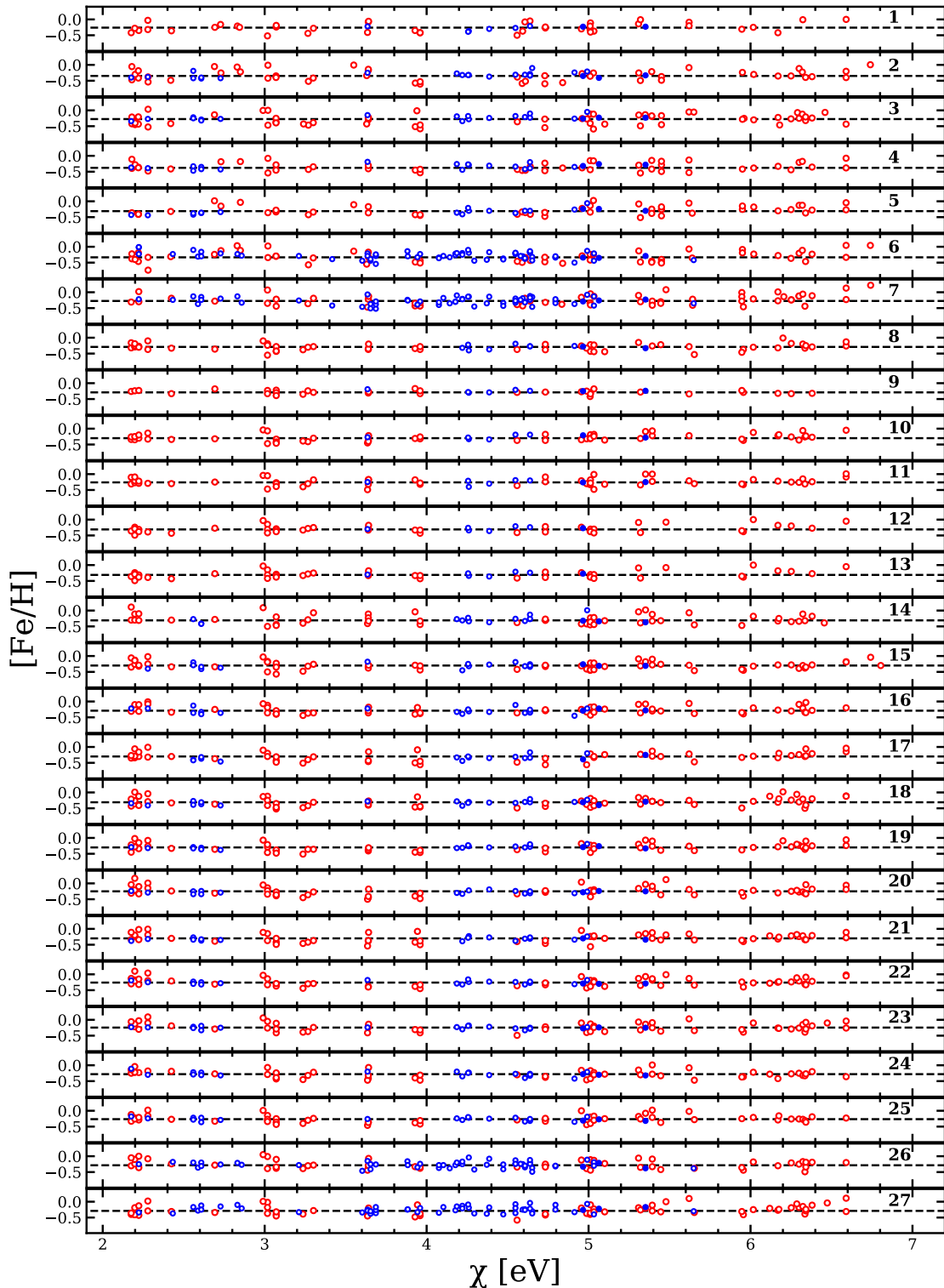
Figure 5.5: Iron abundances from different optical (blue) and NIR (red) lines as a function of the excitation potential for the studied RSGs in the Perseus complex. Circles indicates neutral lines, dots single-ionized lines.
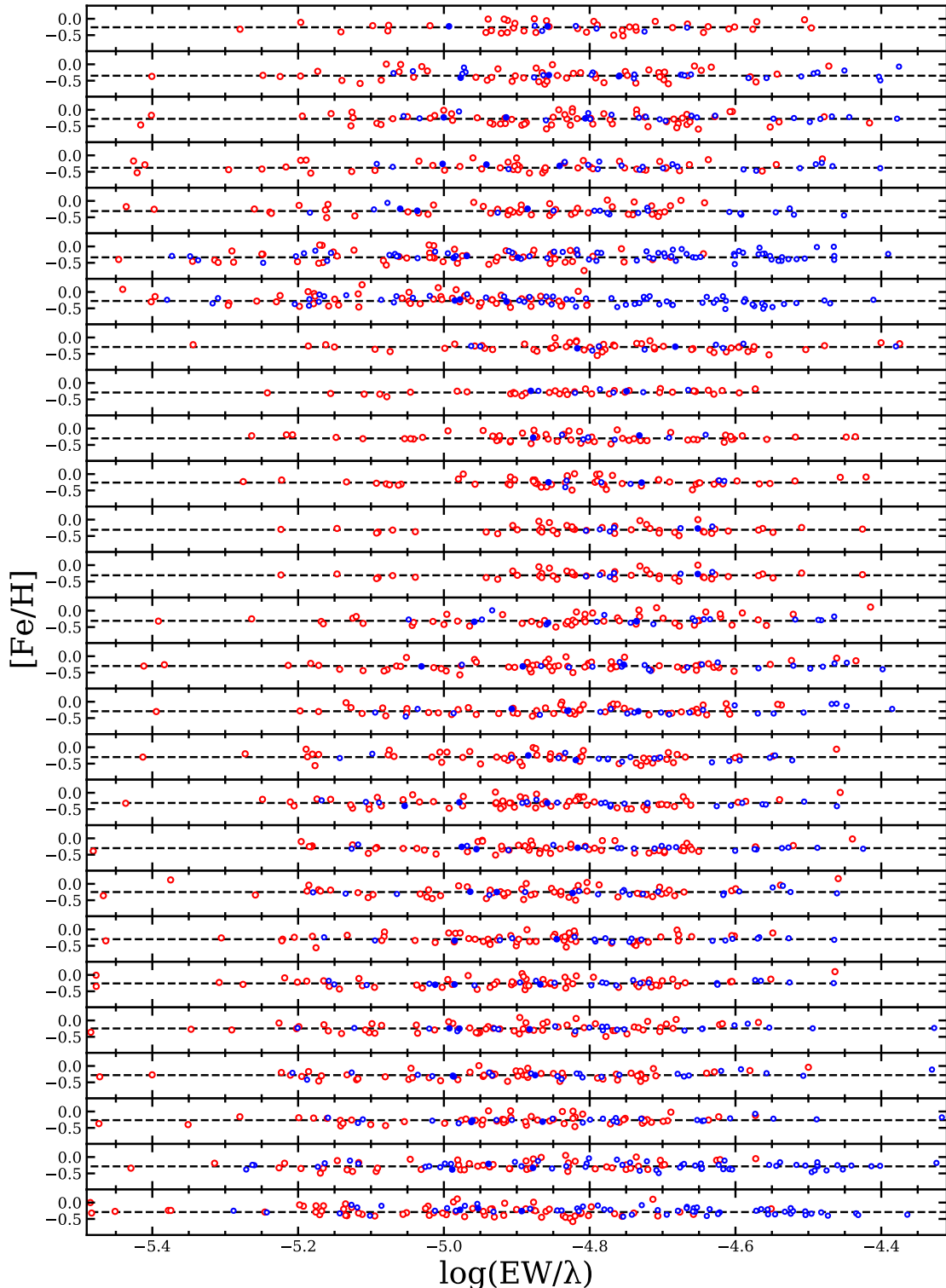
Figure 5.6: Iron abundances from different optical (blue) and NIR (red) lines as a function of the reduced equivalent widths for the studied RSGs in the Perseus complex. Circles indicates neutral lines, dots single-ionized lines.
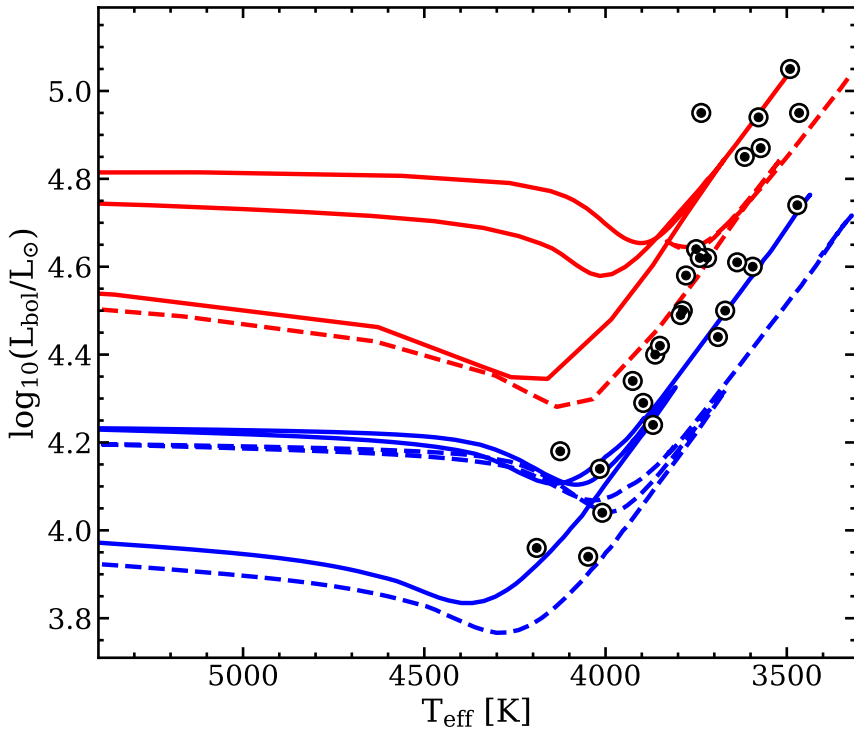
Figure 5.7: HR diagram for the 27 studied RSGs and overplotted the evolutionary tracks of 9 $M_\odot$ (blue lines) and 14 $M_\odot$ (red lines), for half-solar metallicity (solid lines) and solar metallicity (dashed lines) from the PARSEC models (Bressan et al., 2012), for comparison.

Concerning the other iron-peak elements, up to 20 NIR lines of Cr I could be used to derive chromium abundance, while a few lines have been used to derived abundances of V I, Mn I, Co I, Ni I and Cu I. V I, Mn I and Co I lines have hyperfine structure (HFS). Zinc abundances could be obtained only for the warmest K-type RSGs from the measurement of two NIR Zn I lines. Iron-peak elements homogeneously scale as iron within ± 0.1 dex.

Dozens of un-blended lines of Si I, Ca I, Ti I and Mg I and a few lines of Na I, Al I, S I, K I, Sc I (the latter with HFS) have been measured for each specie, also providing about solar-scaled abundances with the possible exception of Na and K, which turns out to be mildly enhanced with respect to the solar-scaled value. In particular, average [Na/Fe] = +0.18 ± 0.10 with σ = 0.10 ± 0.01 and [K/Fe] = +0.10 ± 0.10 with σ = 0.10 ± 0.01 dex have been obtained. Slightly sub-solar values for the fluorine abundance, with an average [F/Fe] = -0.20 ± 0.10 and σ = 0.17 ± 0.02 dex, have been obtained by measuring the HF molecular line at 23358.33 Å in the K band, and using the transition parameters of Jönsson et al. (2014).

The measurement of two lines of Y I and Ce II and one line of Dy II (r-process element) provided solar-scaled [Y/Fe], and slightly enhanced [Dy/Fe] and [Ce/Fe]
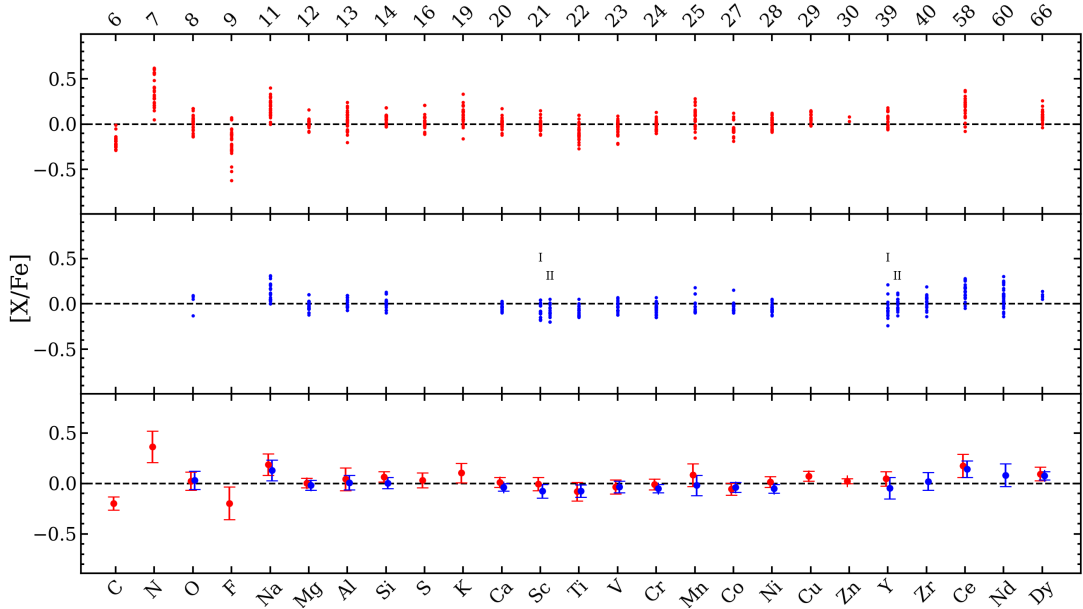
Figure 5.8: Derived [X/Fe] abundance ratios for the studied RSGs in the Perseus Complex from the NIR (top panel, red symbols) and optical (central panel, blue symbols). Bottom panel shows average [X/Fe] for each element for NIR (red symbols) and optical (blue symbols) with the average errorbars. Values are solar-scaled according to Grevesse & Sauval (1998) solar reference, with the only exception of oxygen for which we used Asplund et al. (2009).

abundance ratios. In particular we found average [Dy/Fe] = +0.08 ± 0.10 with σ = 0.09 ± 0.01 and [Ce/Fe] = +0.17 ± 0.10 with σ = 0.12 ± 0.01 dex.

Notably, despite the low temperatures and gravities of the analyzed RSGs, chemical abundances for 19 species have been also derived from more than 100 optical atomic lines. Their values and corresponding measurement errors are listed in Table 5.3 and Table 5.4. All the chemical elements measured in the optical are in common with those measured in the NIR with the exception of Zr and Nd, and the derived chemical abundances from the two datasets are fully consistent one to each other within the errors, as also shown in Fig. 5.8.

Interestingly, in the optical, iron abundance could be derived from both a few tens neutral and a few single-ionized lines, while oxygen could be measured only in the warmest K giants, where TiO contamination is minimal. Concerning Na I, we used only the doublet at 6154.226 and 6160.747 Å since only marginally affected by NLTE effects, with ≤0.1 dex negative corrections (Alexeeva et al., 2014; Lind et al., 2011; Mashonkina et al., 2000). This doublet provides sodium abundances consistent with those derived from the three selected lines in the NIR at 10746.449 Å, 16388.850 Å (partially blended with a Ni I line at 16388.729 Å) and at 21452.373 Å. For the coolest stars, the TiO and CN contamination is so severe that only a few

Mg, Fe I, Fe II, Cr I, Ce II and Nd II lines could be measured. About solar-scaled values for the majority of the measured elements, including Zr that could not be measured in the NIR, and the slightly enhancement of Na, Y, Dy, Ce and Nd (not measured in the NIR) has been also consistently inferred from the optical lines.

About solar-scaled [X/Fe] abundance ratios for most of the elements are consistent with RSGs being a thin disc population. However we also found deviations (on average between 0.1 and 0.2 dex) from solar-scaled abundance ratios for some elements, suggesting possible peculiarities in the recent enrichment of the thin disc by AGB and/or Wolf-Rayet stars within the Perseus complex. In particular, an average mild depletion of [F/Fe] and enhancement of [K/Fe] and [Na/Fe] light elements, at variance with the solar-scaled value of [Al/Fe] and [α/Fe] elements and a mild enhancement of [Ce/Fe] and [Nd/Fe] heavy-s process elements, at variance with the solar-scaled value of the [Y/Fe] light s-process element have been measured.

For the three stars in common with the study of Gazak et al. (2014) , we inferred spectroscopic temperatures that are systematically about 300-400 K cooler than in Gazak et al. (2014) and agree within about 100 K with those of Levesque et al. (2005), and 0.1-0.3 dex lower metallicities. We also measured some depletion of [C/Fe] and enhancement of [N/Fe] compared to the solar-scaled values adopted by Gazak et al. (2014). The warm temperatures, about solar metallicity and solar-scaled CNO abundances quoted by Gazak et al. 2014 cannot provide a reasonable, simultaneous fit of the CO, OH, CN, and TiO molecular absorptions observed in our HARPS-N and GIANO-B spectra of the three RSGs in common. Global spectral synthesis in the J band alone, as used by Gazak et al. (2014), may be not sufficiently adequate to simultaneously measure stellar parameters and global metallicity of complex atmospheres like those of RSGs because the resulting estimates are likely affected by degeneracy and systematics. In order to mitigate them, a wide NIR spectral coverage and self-consistent determination of CNO abundances are especially critical requirements.

Table 5.3: CNO, F, Na, Al, K and alpha element abundances for the studied RSGs in the Perseus complex.

#	[C/H] NIR	¹²C/¹³C NIR	[N/H] NIR	[O/H] NIR	[O/H] OPT	[F/H] NIR	[Na/H] NIR	[Na/H] OPT	[Al/H] NIR	[Al/H] OPT	[K/H] NIR	[Mg/H] NIR	[Mg/H] OPT	[Si/H] NIR	[Si/H] OPT	[S/H] NIR	[Ca/H] NIR	[Ca/H] OPT	[ScI/H] NIR	[ScI/H] OPT	[ScII/H] OPT	[Ti/H] NIR	[Ti/H] OPT
1	-0.54(29) ± 0.05	7.00(2) ± 1.50	0.26(18) ± 0.04	-0.33(17) ± 0.02	–	-0.50(1) ± 0.10	-0.15(3) ± 0.07	–	-0.33(4) ± 0.08	–	-0.14(1) ± 0.10	-0.29(4) ± 0.07	-0.38(2) ± 0.10	-0.31(11) ± 0.04	–	-0.14(1) ± 0.10	-0.32(10) ± 0.06	–	-0.32(3) ± 0.09	–	–	-0.40(11) ± 0.05	–
2	-0.58(45) ± 0.02	8.00(2) ± 1.00	0.05(54) ± 0.02	-0.35(34) ± 0.01	–	-0.58(1) ± 0.10	-0.20(3) ± 0.04	-0.25(2) ± 0.10	-0.41(4) ± 0.07	-0.36(2) ± 0.10	-0.28(1) ± 0.10	-0.37(3) ± 0.08	-0.38(2) ± 0.10	-0.29(12) ± 0.04	-0.39(2) ± 0.10	-0.36(5) ± 0.08	-0.31(14) ± 0.05	-0.29(3) ± 0.07	-0.32(5) ± 0.08	-0.43(4) ± 0.02	–	-0.47(16) ± 0.04	-0.35(17) ± 0.01
3	-0.55(43) ± 0.02	8.00(2) ± 1.00	0.10(61) ± 0.02	-0.37(31) ± 0.01	–	-0.56(1) ± 0.10	-0.14(3) ± 0.05	-0.20(2) ± 0.10	-0.35(4) ± 0.07	-0.32(2) ± 0.10	-0.31(1) ± 0.10	-0.27(4) ± 0.07	-0.25(2) ± 0.10	-0.25(10) ± 0.04	-0.25(2) ± 0.10	-0.37(2) ± 0.10	-0.28(13) ± 0.04	-0.29(5) ± 0.07	-0.34(4) ± 0.09	-0.43(3) ± 0.02	–	-0.47(16) ± 0.04	-0.35(17) ± 0.01
4	-0.66(37) ± 0.02	11.00(2) ± 1.00	0.10(58) ± 0.01	-0.34(16) ± 0.01	–	-0.63(1) ± 0.10	-0.26(3) ± 0.07	-0.18(2) ± 0.10	-0.50(5) ± 0.05	-0.33(2) ± 0.10	-0.33(1) ± 0.10	-0.40(4) ± 0.04	-0.36(2) ± 0.10	-0.28(12) ± 0.06	-0.33(2) ± 0.10	-0.31(2) ± 0.10	-0.28(12) ± 0.03	-0.35(5) ± 0.04	-0.43(6) ± 0.08	–	–	-0.44(15) ± 0.04	-0.42(25) ± 0.02
5	-0.56(39) ± 0.02	10.00(2) ± 1.00	0.10(56) ± 0.01	-0.34(13) ± 0.01	–	-0.53(1) ± 0.10	-0.10(3) ± 0.05	-0.05(2) ± 0.10	-0.24(5) ± 0.05	-0.37(2) ± 0.10	-0.17(1) ± 0.10	-0.27(4) ± 0.04	-0.26(2) ± 0.10	-0.22(11) ± 0.03	-0.25(2) ± 0.10	-0.33(3) ± 0.04	-0.25(12) ± 0.03	-0.36(5) ± 0.04	-0.33(3) ± 0.15	-0.38(4) ± 0.04	–	-0.44(16) ± 0.04	-0.36(22) ± 0.02
6	-0.34(36) ± 0.01	29.00(2) ± 1.50	-0.28(62) ± 0.01	-0.23(13) ± 0.01	-0.24(1) ± 0.10	-0.39(1) ± 0.10	-0.31(3) ± 0.03	-0.29(2) ± 0.10	-0.22(5) ± 0.04	-0.20(2) ± 0.10	-0.09(1) ± 0.10	-0.28(7) ± 0.05	-0.32(2) ± 0.10	-0.23(25) ± 0.03	-0.29(2) ± 0.10	-0.35(5) ± 0.03	-0.26(9) ± 0.04	-0.33(5) ± 0.09	-0.32(5) ± 0.10	-0.25(4) ± 0.07	–	-0.32(28) ± 0.03	-0.29(22) ± 0.03
7	-0.38(28) ± 0.02	23.00(2) ± 1.50	-0.18(56) ± 0.01	-0.16(16) ± 0.01	-0.20(1) ± 0.10	-0.43(1) ± 0.10	0.07(3) ± 0.08	-0.01(2) ± 0.10	-0.23(2) ± 0.10	-0.20(2) ± 0.10	0.00(1) ± 0.10	-0.17(9) ± 0.02	-0.32(2) ± 0.10	-0.15(30) ± 0.03	-0.29(2) ± 0.10	-0.34(5) ± 0.03	-0.16(9) ± 0.03	-0.33(5) ± 0.11	-0.26(3) ± 0.03	-0.25(4) ± 0.04	–	-0.23(27) ± 0.02	-0.29(22) ± 0.01
8	-0.55(31) ± 0.02	7.00(2) ± 1.00	-0.12(56) ± 0.01	-0.30(21) ± 0.01	–	-0.59(1) ± 0.10	-0.23(3) ± 0.05	-0.26(3) ± 0.08	-0.31(3) ± 0.10	-0.34(3) ± 0.06	-0.25(1) ± 0.10	-0.31(3) ± 0.03	-0.30(2) ± 0.10	-0.23(12) ± 0.04	-0.31(2) ± 0.10	-0.41(1) ± 0.10	-0.30(13) ± 0.05	-0.40(5) ± 0.07	-0.41(5) ± 0.04	-0.47(4) ± 0.03	-0.37(8) ± 0.08	-0.43(28) ± 0.03	-0.45(19) ± 0.02
9	-0.51(35) ± 0.01	7.00(2) ± 1.50	-0.08(58) ± 0.01	-0.33(21) ± 0.01	–	-0.59(1) ± 0.10	-0.29(3) ± 0.03	-0.33(3) ± 0.08	-0.28(3) ± 0.06	-0.34(2) ± 0.10	-0.23(1) ± 0.10	-0.28(3) ± 0.05	-0.30(2) ± 0.10	-0.21(11) ± 0.03	-0.22(1) ± 0.10	-0.31(2) ± 0.10	-0.32(11) ± 0.03	-0.31(5) ± 0.07	-0.31(5) ± 0.06	-0.44(3) ± 0.03	-0.43(8) ± 0.04	-0.46(27) ± 0.02	-0.45(17) ± 0.05
10	-0.45(33) ± 0.01	9.00(2) ± 1.50	-0.03(51) ± 0.01	-0.18(19) ± 0.01	–	-0.35(1) ± 0.10	-0.07(3) ± 0.05	-0.04(2) ± 0.16	-0.21(1) ± 0.10	-0.17(3) ± 0.06	-0.08(1) ± 0.10	-0.24(3) ± 0.05	-0.24(2) ± 0.10	-0.18(11) ± 0.04	-0.25(2) ± 0.10	-0.33(3) ± 0.03	-0.21(9) ± 0.04	-0.24(4) ± 0.09	-0.23(3) ± 0.03	-0.39(3) ± 0.04	-0.37(8) ± 0.03	-0.25(25) ± 0.02	-0.31(19) ± 0.02
11	-0.49(31) ± 0.01	6.00(2) ± 1.50	-0.06(57) ± 0.01	-0.13(21) ± 0.01	–	-0.25(1) ± 0.10	-0.10(3) ± 0.03	-0.20(1) ± 0.10	-0.22(2) ± 0.10	-0.23(3) ± 0.06	-0.09(1) ± 0.10	-0.27(3) ± 0.08	-0.30(2) ± 0.10	-0.31(12) ± 0.03	-0.31(1) ± 0.10	-0.30(3) ± 0.03	-0.30(11) ± 0.03	-0.39(4) ± 0.09	-0.15(3) ± 0.05	-0.32(2) ± 0.10	-0.46(6) ± 0.08	-0.20(25) ± 0.02	-0.26(16) ± 0.03
12	-0.48(28) ± 0.01	9.00(2) ± 1.00	0.02(54) ± 0.02	-0.20(21) ± 0.01	–	-0.38(1) ± 0.10	-0.04(3) ± 0.03	-0.13(2) ± 0.08	-0.21(3) ± 0.06	-0.23(3) ± 0.06	-0.12(1) ± 0.10	-0.28(3) ± 0.05	-0.30(2) ± 0.10	-0.29(12) ± 0.03	-0.35(2) ± 0.10	-0.18(3) ± 0.02	-0.27(11) ± 0.02	-0.34(5) ± 0.09	-0.27(3) ± 0.04	-0.35(4) ± 0.04	-0.36(8) ± 0.03	-0.33(25) ± 0.02	-0.31(20) ± 0.02
13	-0.50(28) ± 0.01	8.00(2) ± 1.00	0.02(55) ± 0.02	-0.25(20) ± 0.01	–	-0.31(1) ± 0.10	-0.02(3) ± 0.01	-0.04(1) ± 0.10	-0.33(1) ± 0.10	-0.27(2) ± 0.10	-0.15(1) ± 0.10	-0.28(3) ± 0.08	-0.30(2) ± 0.10	-0.25(10) ± 0.03	-0.27(2) ± 0.10	-0.25(3) ± 0.03	-0.24(11) ± 0.03	-0.28(5) ± 0.05	-0.27(4) ± 0.03	-0.42(4) ± 0.03	-0.45(8) ± 0.03	-0.36(23) ± 0.02	-0.38(22) ± 0.02
14	-0.49(38) ± 0.01	9.00(2) ± 1.00	0.01(55) ± 0.02	-0.24(21) ± 0.01	–	-0.42(1) ± 0.10	-0.22(3) ± 0.08	-0.29(2) ± 0.10	-0.33(3) ± 0.04	-0.36(2) ± 0.10	-0.17(1) ± 0.10	-0.32(3) ± 0.04	-0.30(2) ± 0.10	-0.25(14) ± 0.05	-0.28(1) ± 0.10	-0.24(5) ± 0.08	-0.27(12) ± 0.02	-0.34(2) ± 0.05	-0.32(3) ± 0.01	-0.41(4) ± 0.08	-0.52(5) ± 0.08	-0.35(32) ± 0.02	-0.39(17) ± 0.05
15	-0.42(27) ± 0.01	16.00(2) ± 1.00	-0.09(57) ± 0.02	-0.13(17) ± 0.01	–	-0.21(1) ± 0.10	0.01(3) ± 0.03	-0.05(2) ± 0.10	-0.15(1) ± 0.10	-0.23(3) ± 0.06	-0.08(1) ± 0.10	-0.29(3) ± 0.05	-0.28(2) ± 0.10	-0.28(12) ± 0.05	-0.27(2) ± 0.10	-0.21(3) ± 0.06	-0.25(10) ± 0.03	-0.30(5) ± 0.08	-0.17(3) ± 0.03	-0.29(3) ± 0.08	-0.32(8) ± 0.04	-0.22(23) ± 0.02	-0.32(15) ± 0.03
16	-0.55(27) ± 0.02	22.00(2) ± 1.00	0.30(26) ± 0.03	-0.38(12) ± 0.01	–	-0.88(1) ± 0.10	-0.02(3) ± 0.09	–	-0.35(3) ± 0.08	–	-0.21(1) ± 0.10	-0.23(3) ± 0.07	-0.29(2) ± 0.10	-0.08(13) ± 0.06	–	-0.19(2) ± 0.10	-0.26(12) ± 0.04	–	-0.38(4) ± 0.09	–	–	-0.53(29) ± 0.02	–
17	-0.52(34) ± 0.02	17.00(2) ± 1.00	0.10(38) ± 0.02	-0.36(21) ± 0.01	–	-0.77(1) ± 0.10	-0.14(3) ± 0.02	-0.15(1) ± 0.10	-0.38(3) ± 0.06	-0.39(2) ± 0.10	-0.32(1) ± 0.10	-0.32(3) ± 0.02	-0.29(2) ± 0.10	-0.21(12) ± 0.06	-0.29(2) ± 0.10	-0.09(3) ± 0.10	-0.36(13) ± 0.04	-0.35(5) ± 0.10	-0.37(5) ± 0.06	-0.47(2) ± 0.10	-0.41(5) ± 0.04	-0.45(28) ± 0.01	-0.46(18) ± 0.01
18	-0.45(33) ± 0.01	10.00(2) ± 1.00	0.02(58) ± 0.01	-0.23(19) ± 0.01	–	-0.53(1) ± 0.10	-0.18(2) ± 0.10	-0.21(3) ± 0.08	-0.16(3) ± 0.04	-0.19(3) ± 0.05	-0.16(1) ± 0.10	-0.26(3) ± 0.07	-0.16(2) ± 0.10	-0.19(13) ± 0.08	-0.13(2) ± 0.10	-0.26(5) ± 0.06	-0.27(12) ± 0.04	-0.30(4) ± 0.05	-0.35(5) ± 0.03	-0.34(4) ± 0.03	-0.21(8) ± 0.10	-0.38(29) ± 0.02	-0.38(21) ± 0.01
19	-0.53(30) ± 0.01	12.00(2) ± 1.00	0.28(43) ± 0.03	-0.43(20) ± 0.01	–	-0.81(1) ± 0.10	0.02(1) ± 0.08	–	-0.49(3) ± 0.08	–	-0.45(1) ± 0.10	-0.38(2) ± 0.10	-0.31(1) ± 0.10	-0.24(9) ± 0.04	–	-0.25(3) ± 0.04	-0.41(7) ± 0.03	–	-0.29(4) ± 0.05	–	–	-0.52(19) ± 0.02	–
20	-0.47(26) ± 0.01	9.00(2) ± 1.00	0.03(51) ± 0.01	-0.22(21) ± 0.01	-0.18(1) ± 0.10	-0.42(1) ± 0.10	0.08(1) ± 0.10	0.04(2) ± 0.10	-0.15(2) ± 0.04	-0.22(3) ± 0.05	-0.09(1) ± 0.08	-0.29(3) ± 0.06	-0.31(2) ± 0.10	-0.28(10) ± 0.04	-0.33(2) ± 0.10	-0.24(3) ± 0.02	-0.28(9) ± 0.02	-0.32(4) ± 0.08	-0.22(3) ± 0.04	-0.26(4) ± 0.04	-0.30(7) ± 0.10	-0.25(26) ± 0.02	-0.28(14) ± 0.04
21	-0.43(27) ± 0.02	13.00(2) ± 1.00	0.28(28) ± 0.03	-0.26(21) ± 0.01	–	-0.56(1) ± 0.10	-0.04(1) ± 0.10	–	-0.09(2) ± 0.10	–	-0.24(1) ± 0.10	-0.28(3) ± 0.08	-0.36(2) ± 0.10	-0.21(13) ± 0.08	–	-0.27(2) ± 0.10	-0.32(10) ± 0.04	–	-0.35(2) ± 0.10	–	–	-0.46(30) ± 0.02	–
22	-0.46(28) ± 0.02	17.00(2) ± 1.00	-0.01(56) ± 0.01	-0.13(16) ± 0.01	–	-0.24(1) ± 0.10	0.00(1) ± 0.10	-0.18(1) ± 0.10	-0.25(2) ± 0.10	-0.37(2) ± 0.10	-0.20(1) ± 0.10	-0.31(3) ± 0.06	-0.31(2) ± 0.10	-0.31(10) ± 0.03	-0.35(2) ± 0.10	-0.34(3) ± 0.03	-0.28(12) ± 0.04	-0.35(3) ± 0.10	-0.26(1) ± 0.10	-0.33(3) ± 0.02	-0.33(4) ± 0.08	-0.28(26) ± 0.02	-0.43(10) ± 0.02
23	-0.47(37) ± 0.01	19.00(2) ± 1.00	0.25(26) ± 0.04	-0.37(21) ± 0.01	–	-0.46(1) ± 0.10	-0.04(1) ± 0.10	–	-0.15(3) ± 0.01	–	-0.27(1) ± 0.10	-0.27(3) ± 0.07	-0.30(1) ± 0.10	-0.22(12) ± 0.04	–	-0.19(2) ± 0.10	-0.26(11) ± 0.04	–	-0.34(2) ± 0.10	–	–	-0.44(28) ± 0.02	–
24	-0.43(23) ± 0.02	21.00(2) ± 1.00	-0.05(57) ± 0.01	-0.19(19) ± 0.01	–	-0.41(1) ± 0.10	-0.18(1) ± 0.10	-0.16(3) ± 0.06	-0.10(4) ± 0.01	-0.19(3) ± 0.06	-0.14(1) ± 0.10	-0.30(3) ± 0.10	-0.27(2) ± 0.10	-0.19(12) ± 0.04	-0.23(2) ± 0.10	-0.24(2) ± 0.10	-0.28(11) ± 0.02	-0.32(5) ± 0.08	-0.26(5) ± 0.07	-0.34(4) ± 0.03	-0.27(7) ± 0.04	-0.34(27) ± 0.02	-0.37(22) ± 0.02
25	-0.50(20) ± 0.02	14.00(2) ± 1.00	0.29(15) ± 0.04	-0.27(18) ± 0.02	–	-0.40(1) ± 0.10	-0.14(1) ± 0.10	–	-0.07(1) ± 0.10	–	-0.21(1) ± 0.10	-0.33(1) ± 0.10	-0.34(1) ± 0.04	-0.23(7) ± 0.04	–	–	-0.30(7) ± 0.06	–	-0.34(1) ± 0.10	–	–	-0.41(22) ± 0.03	–
26	-0.56(24) ± 0.04	19.00(2) ± 1.00	0.31(18) ± 0.04	-0.45(17) ± 0.01	-0.41(1) ± 0.10	-0.59(1) ± 0.10	-0.23(3) ± 0.01	-0.24(2) ± 0.10	-0.27(3) ± 0.05	-0.31(2) ± 0.10	-0.31(1) ± 0.10	-0.33(3) ± 0.04	-0.40(2) ± 0.10	-0.21(8) ± 0.02	-0.32(1) ± 0.10	-0.27(2) ± 0.02	-0.36(10) ± 0.02	-0.35(2) ± 0.10	-0.38(4) ± 0.05	-0.39(2) ± 0.10	-0.39(5) ± 0.03	-0.42(25) ± 0.03	-0.42(12) ± 0.04
27	-0.53(23) ± 0.02	19.00(2) ± 1.50	0.08(27) ± 0.03	-0.28(19) ± 0.01	–	-0.60(1) ± 0.10	-0.15(1) ± 0.10	–	-0.17(1) ± 0.10	–	-0.20(1) ± 0.10	-0.36(3) ± 0.10	-0.36(2) ± 0.10	-0.23(9) ± 0.03	–	-0.20(1) ± 0.10	-0.38(9) ± 0.02	–	-0.28(2) ± 0.10	–	–	-0.40(22) ± 0.03	–

Table 5.4: Iron, iron-peak and neutron-capture element abundances for the studied RSGs in the Perseus complex.

#	[FeI/H] NIR	[FeI/H] OPT	[FeII/H] OPT	[V/H] NIR	[V/H] OPT	[Cr/H] NIR	[Cr/H] OPT	[Mn/H] NIR	[Mn/H] OPT	[Co/H] NIR	[Co/H] OPT	[Ni/H] NIR	[Ni/H] OPT	[Cu/H] NIR	[Zn/H] NIR	[YI/H] NIR	[YI/H] OPT	[YII/H] OPT	[Zr/H] OPT	[Ce/H] NIR	[Ce/H] OPT	[Nd/Fe] OPT	[Dy/H] NIR	[Dy/H] OPT
1	-0.35(42) ±0.03	-0.32(6) ±0.04	-0.35(2) ±0.10	-0.26(3) ±0.04	–	-0.27(19) ±0.04	-0.30(1) ±0.10	-0.25(2) ±0.10	–	-0.23(4) ±0.06	–	-0.28(4) ±0.09	–	-0.24(1) ±0.10	–	-0.21(1) ±0.10	–	–	–	–	-0.15(1) ±0.10	-0.23(2) ±0.10	–	–
2	-0.35(52) ±0.02	-0.32(23) ±0.02	-0.35(3) ±0.03	-0.36(3) ±0.03	-0.26(14) ±0.01	-0.36(18) ±0.04	-0.30(9) ±0.03	-0.37(2) ±0.08	-0.38(1) ±0.02	-0.44(3) ±0.12	-0.33(7) ±0.02	-0.39(6) ±0.10	-0.36(7) –	-0.21(1) ±0.10	–	-0.21(2) ±0.10	–	–	-0.30(7) ±0.03	-0.11(2) ±0.10	-0.15(2) ±0.10	-0.23(8) ±0.03	-0.26(1) ±0.10	-0.22(1) ±0.10
3	-0.27(61) ±0.02	-0.25(23) ±0.02	-0.23(3) ±0.10	-0.39(3) ±0.03	-0.26(14) ±0.02	-0.37(18) ±0.04	-0.30(9) ±0.02	-0.42(2) ±0.10	-0.32(1) ±0.10	-0.36(3) ±0.08	-0.25(8) ±0.02	-0.25(7) ±0.11	-0.23(7) ±0.02	-0.25(1) ±0.10	–	-0.31(1) ±0.10	–	–	-0.39(8) ±0.05	-0.12(2) ±0.10	-0.15(3) ±0.03	-0.23(8) ±0.03	-0.19(1) ±0.10	-0.20(1) ±0.10
4	-0.38(49) ±0.02	-0.35(21) ±0.02	-0.28(3) ±0.10	-0.40(3) ±0.03	-0.39(17) ±0.01	-0.37(18) ±0.04	-0.35(9) ±0.03	-0.26(2) ±0.10	-0.38(2) ±0.10	-0.42(3) ±0.10	-0.34(8) ±0.02	-0.28(6) ±0.11	-0.39(7) ±0.02	-0.24(1) ±0.10	–	-0.36(2) ±0.10	-0.30(1) ±0.10	-0.30(1) ±0.10	-0.36(7) ±0.02	-0.10(2) ±0.10	-0.10(3) ±0.03	-0.18(8) ±0.02	-0.27(1) ±0.10	-0.27(1) ±0.10
5	-0.31(48) ±0.02	-0.36(21) ±0.02	-0.24(3) ±0.03	-0.37(3) ±0.03	-0.29(17) ±0.01	-0.30(16) ±0.10	-0.29(7) ±0.04	-0.34(1) ±0.10	-0.39(1) ±0.10	-0.26(4) ±0.09	-0.21(6) ±0.02	-0.26(5) ±0.12	-0.32(8) ±0.02	-0.24(1) ±0.10	–	-0.22(2) ±0.10	-0.31(1) ±0.10	-0.31(1) ±0.10	-0.40(7) ±0.02	-0.09(2) ±0.10	-0.15(3) ±0.03	-0.25(6) ±0.03	-0.24(1) ±0.10	–
6	-0.33(57) ±0.02	-0.29(63) ±0.01	-0.34(3) ±0.17	-0.33(3) ±0.03	-0.36(17) ±0.02	-0.29(16) ±0.03	-0.33(7) ±0.04	-0.42(1) ±0.10	-0.38(1) ±0.10	-0.39(5) ±0.09	-0.39(8) ±0.05	-0.31(4) ±0.12	-0.35(8) ±0.06	-0.34(1) ±0.10	-0.30(2) ±0.10	-0.17(1) ±0.10	–	–	-0.23(8) ±0.03	-0.05(2) ±0.10	-0.15(2) ±0.10	-0.06(4) ±0.02	-0.25(1) ±0.10	–
7	-0.33(57) ±0.02	-0.29(63) ±0.01	-0.34(3) ±0.03	-0.30(2) ±0.10	-0.36(16) ±0.01	-0.20(18) ±0.02	-0.33(7) ±0.03	-0.38(1) ±0.10	-0.38(1) ±0.10	-0.25(6) ±0.06	-0.39(7) ±0.02	-0.29(6) ±0.05	-0.35(7) ±0.03	-0.20(1) ±0.10	-0.25(2) ±0.10	-0.15(2) –	–	–	-0.23(8) ±0.03	-0.02(1) ±0.10	-0.01(3) ±0.02	0.01(5) ±0.02	-0.22(1) ±0.10	–
8	-0.30(57) ±0.02	-0.30(21) ±0.01	-0.29(3) ±0.02	-0.35(1) ±0.04	-0.42(15) ±0.03	-0.36(17) ±0.10	-0.39(8) ±0.10	-0.19(2) ±0.10	–	-0.39(2) ±0.10	-0.37(8) ±0.03	-0.23(3) ±0.12	-0.39(5) ±0.03	–	–	-0.31(1) ±0.10	-0.30(1) ±0.10	-0.30(1) ±0.10	-0.31(10) ±0.02	-0.32(1) ±0.10	-0.21(3) ±0.03	-0.22(10) ±0.03	-0.19(1) ±0.10	-0.16(1) ±0.10
9	-0.29(56) ±0.02	-0.33(21) ±0.02	-0.26(3) ±0.02	-0.42(1) ±0.10	-0.40(13) ±0.03	-0.37(17) ±0.05	-0.35(7) ±0.03	-0.19(2) ±0.10	–	-0.37(2) ±0.10	-0.38(8) ±0.02	-0.27(3) ±0.10	-0.34(7) ±0.05	–	–	-0.26(2) ±0.10	-0.37(1) ±0.10	-0.37(1) ±0.10	-0.28(10) ±0.04	-0.20(2) ±0.10	-0.20(3) ±0.03	-0.27(10) ±0.04	-0.23(1) ±0.10	–
10	-0.24(60) ±0.02	-0.24(24) ±0.01	-0.25(3) ±0.02	-0.27(1) ±0.10	-0.24(16) ±0.02	-0.23(18) ±0.04	-0.31(7) ±0.04	-0.19(2) ±0.10	-0.33(2) ±0.10	-0.31(2) ±0.10	-0.31(8) ±0.04	-0.25(2) ±0.10	-0.30(7) ±0.02	–	–	-0.17(1) ±0.10	-0.29(1) ±0.10	-0.29(1) ±0.10	-0.14(10) ±0.04	0.04(1) ±0.10	-0.06(2) ±0.09	-0.13(9) ±0.03	-0.19(1) ±0.10	–
11	-0.30(61) ±0.02	-0.31(20) ±0.01	-0.32(2) ±0.10	-0.26(1) ±0.10	-0.28(16) ±0.03	-0.27(18) ±0.05	-0.28(8) ±0.05	-0.27(3) ±0.16	-0.41(2) ±0.10	-0.34(2) ±0.10	-0.32(8) ±0.04	-0.19(3) ±0.13	-0.38(2) ±0.10	–	–	–	-0.38(1) ±0.4	-0.38(1) ±0.4	-0.24(10) ±0.03	-0.18(1) ±0.10	-0.24(3) ±0.03	-0.23(9) ±0.07	-0.10(1) ±0.10	–
12	-0.26(60) ±0.02	-0.25(23) ±0.01	-0.29(3) ±0.01	-0.25(1) ±0.10	-0.28(15) ±0.03	-0.28(17) ±0.05	-0.31(9) ±0.02	-0.11(2) ±0.10	–	-0.31(2) ±0.10	-0.27(8) ±0.03	-0.32(2) ±0.10	-0.34(7) ±0.5	–	–	–	-0.22(1) ±0.10	-0.22(1) ±0.10	-0.17(10) ±0.04	0.08(2) ±0.10	0.01(1) ±0.10	-0.14(10) ±0.04	-0.10(1) ±0.10	–
13	-0.26(56) ±0.02	-0.25(23) ±0.01	-0.30(3) ±0.02	-0.47(1) ±0.10	-0.37(9) ±0.04	-0.26(17) ±0.04	-0.31(8) ±0.02	-0.17(3) ±0.14	-0.28(1) ±0.10	-0.34(2) ±0.10	-0.31(7) ±0.10	-0.35(3) ±0.09	-0.37(8) ±0.03	–	–	–	-0.34(1) ±0.10	-0.34(1) ±0.10	-0.22(10) ±0.03	-0.37(2) ±0.10	-0.07(1) ±0.10	-0.17(9) ±0.02	-0.20(1) ±0.10	–
14	-0.31(62) ±0.02	-0.32(22) ±0.03	-0.33(3) ±0.03	-0.25(1) ±0.10	-0.28(12) ±0.02	-0.33(18) ±0.09	-0.34(7) ±0.02	-0.25(3) ±0.10	-0.40(2) ±0.10	-0.39(3) ±0.07	-0.35(8) ±0.04	-0.30(3) ±0.14	-0.39(5) ±0.02	–	–	-0.25(2) ±0.10	-0.45(1) ±0.10	-0.45(1) ±0.10	-0.35(10) ±0.01	-0.16(2) ±0.10	-0.13(1) ±0.10	-0.29(10) ±0.10	-0.17(1) ±0.10	–
15	-0.28(54) ±0.02	-0.27(23) ±0.02	-0.30(3) ±0.02	–	-0.27(10) ±0.04	-0.22(15) ±0.04	-0.30(7) ±0.03	-0.24(2) ±0.10	-0.27(2) ±0.10	-0.43(3) ±0.11	-0.28(6) ±0.05	-0.36(5) ±0.09	-0.35(7) ±0.04	–	–	–	-0.17(1) ±0.10	-0.17(1) ±0.10	-0.08(10) ±0.06	0.17(1) ±0.10	–	-0.02(8) ±0.03	-0.02(1) ±0.10	–
16	-0.26(55) ±0.02	-0.23(6) ±0.01	-0.26(2) ±0.10	-0.35(1) ±0.10	–	-0.31(18) ±0.04	-0.38(1) ±0.10	-0.23(2) ±0.10	–	-0.33(3) ±0.04	–	-0.19(3) ±0.02	–	–	–	-0.32(2) ±0.10	–	–	–	-0.25(2) ±0.10	-0.28(1) ±0.10	-0.32(2) ±0.10	-0.30(1) ±0.10	–
17	-0.30(61) ±0.02	-0.32(19) ±0.01	-0.29(3) ±0.10	-0.34(1) ±0.10	-0.40(13) ±0.02	-0.37(18) ±0.10	-0.36(7) ±0.10	-0.24(1) ±0.10	–	-0.37(3) ±0.10	-0.39(7) ±0.05	-0.31(3) ±0.08	-0.34(6) ±0.02	-0.19(1) ±0.10	–	-0.34(2) ±0.10	-0.38(1) ±0.10	-0.38(1) ±0.10	-0.41(8) ±0.03	-0.11(2) ±0.10	-0.18(2) ±0.10	-0.33(8) ±0.05	-0.17(1) ±0.10	–
18	-0.29(66) ±0.02	-0.26(52) ±0.01	-0.22(3) ±0.03	-0.27(1) ±0.10	-0.30(12) ±0.04	-0.33(16) ±0.03	-0.33(8) ±0.03	-0.16(3) ±0.16	-0.08(2) ±0.10	-0.48(3) ±0.10	-0.34(5) ±0.03	-0.29(2) ±0.10	-0.34(7) ±0.02	-0.27(1) ±0.10	–	–	-0.14(1) ±0.10	-0.14(1) ±0.10	-0.19(9) ±0.04	0.08(1) ±0.10	0.01(3) ±0.07	-0.02(9) ±0.03	-0.25(1) ±0.10	–
19	-0.29(55) ±0.02	-0.27(9) ±0.02	-0.30(2) ±0.10	-0.40(1) ±0.10	–	-0.39(11) ±0.01	-0.42(1) ±0.10	-0.15(2) ±0.10	–	-0.35(3) ±0.15	–	-0.36(3) ±0.06	–	-0.23(1) ±0.10	–	-0.31(1) ±0.10	–	–	–	-0.23(2) ±0.10	-0.25(1) ±0.10	-0.38(2) ±0.10	-0.29(1) ±0.10	–
20	-0.25(59) ±0.02	-0.26(20) ±0.01	-0.26(3) ±0.03	-0.24(1) ±0.10	-0.25(12) ±0.03	-0.25(17) ±0.04	-0.26(7) ±0.04	-0.04(2) ±0.10	-0.15(1) ±0.10	-0.34(2) ±0.10	-0.28(8) ±0.03	-0.31(2) ±0.10	-0.30(7) ±0.02	–	–	–	-0.27(1) ±0.10	-0.27(1) ±0.10	-0.23(4) ±0.01	-0.18(1) ±0.10	–	-0.16(8) ±0.10	-0.15(1) ±0.10	–
21	-0.29(61) ±0.02	-0.26(6) ±0.01	-0.26(2) ±0.10	-0.32(1) ±0.10	–	-0.37(17) ±0.04	-0.38(1) ±0.10	-0.05(2) ±0.10	–	-0.37(3) ±0.03	–	-0.23(3) ±0.08	–	-0.16(1) ±0.10	–	–	–	–	–	–	-0.19(1) ±0.10	-0.22(2) ±0.10	-0.28(1) ±0.10	–
22	-0.30(53) ±0.02	-0.34(18) ±0.03	-0.32(2) ±0.10	-0.26(1) ±0.10	-0.37(5) ±0.03	-0.29(17) ±0.04	-0.36(5) ±0.02	-0.31(2) ±0.10	-0.33(2) ±0.10	-0.38(2) ±0.10	-0.35(8) ±0.03	-0.18(3) ±0.16	-0.29(2) ±0.06	-0.16(1) ±0.10	–	–	-0.32(1) ±0.10	-0.32(1) ±0.10	-0.25(6) ±0.03	-0.10(1) ±0.10	–	-0.32(6) ±0.03	-0.16(1) ±0.10	–
23	-0.30(56) ±0.02	-0.28(6) ±0.03	-0.24(2) ±0.04	-0.32(1) ±0.10	–	-0.28(17) ±0.04	-0.41(1) ±0.10	–	–	-0.37(3) ±0.06	–	-0.25(3) ±0.03	–	-0.26(1) ±0.10	–	–	–	–	–	-0.02(1) ±0.10	-0.30(1) ±0.10	-0.42(2) ±0.10	-0.30(1) ±0.10	–
24	-0.28(54) ±0.02	-0.26(54) ±0.01	-0.31(3) ±0.05	-0.50(1) ±0.10	-0.33(5) ±0.05	-0.28(16) ±0.04	-0.37(7) ±0.02	0.00(2) ±0.10	-0.15(2) ±0.10	-0.42(3) ±0.10	-0.33(5) ±0.06	-0.29(2) ±0.10	-0.29(7) ±0.04	-0.23(1) ±0.10	–	–	-0.21(1) ±0.10	-0.21(1) ±0.10	-0.24(8) ±0.03	0.08(1) ±0.10	-0.08(3) ±0.04	-0.05(8) ±0.03	-0.17(1) ±0.10	–
25	-0.31(46) ±0.02	-0.28(6) ±0.02	-0.27(1) ±0.10	-0.29(1) ±0.10	–	-0.29(11) ±0.02	-0.37(1) ±0.10	-0.15(2) ±0.10	–	-0.25(3) ±0.03	–	-0.27(2) ±0.10	–	-0.24(1) ±0.10	–	-0.16(1) ±0.10	–	–	–	0.00(1) ±0.10	-0.22(1) ±0.10	-0.31(2) ±0.10	–	–
26	-0.31(54) ±0.02	-0.28(16) ±0.04	-0.34(3) ±0.02	-0.34(1) ±0.10	-0.38(8) ±0.04	-0.37(14) ±0.04	-0.37(7) ±0.02	-0.06(2) ±0.10	–	-0.38(3) ±0.02	-0.35(7) ±0.02	-0.36(3) ±0.10	-0.41(6) ±0.04	-0.13(1) ±0.10	–	-0.36(2) ±0.10	-0.26(1) ±0.10	-0.26(1) ±0.10	-0.35(8) ±0.03	-0.04(2) ±0.10	-0.14(3) ±0.03	-0.33(8) ±0.03	-0.24(1) ±0.10	–
27	-0.28(36) ±0.01	-0.26(6) ±0.03	-0.24(2) ±0.10	-0.36(1) ±0.10	–	-0.34(13) ±0.02	-0.38(1) ±0.10	-0.18(2) ±0.10	–	-0.33(3) ±0.03	–	-0.30(3) ±0.03	–	-0.23(1) ±0.10	–	-0.20(2) ±0.10	–	–	–	-0.08(1) ±0.10	-0.17(1) ±0.10	-0.11(2) ±0.10	–	–

5.2.1   CNO abundances and stellar mixing

CNO abundances have been derived from a few tens of molecular ^{12}CO, CN and OH lines, respectively. Following Ryde et al. (2009) and Smith et al. (2013), we adopted an iterative method to derive CNO abundances, in order to consider the interplay among these three elements in setting the molecular equilibrium. We found depletion of carbon and enhancement of nitrogen with respect to the solar-scaled values, especially in the case of the coolest RSGs, while oxygen abundance turns out to be about solar-scaled. In particular, average [C/Fe]=-0.20±0.01 dex with a small dispersion of 0.06±0.01 dex and [N/Fe]=+0.36±0.03 and a dispersion of 0.16±0.02 dex have been obtained. It is interesting to notice that the carbon abundance derived from the Δv=3 ^{12}CO band-heads in the H-band, is fully consistent with the one derived from individual ^{12}CO roto-vibrational transitions. We used the Δv=3 and Δv=2 band-heads of ^{13}CO in the H and K bands, respectively, to also estimate the ^{13}C abundance and the ^{12}C/^{13}C isotopic abundance ratio, that turns out to be between 20 and 30 in the K-type RSGs and below 12 in the M-type RSGs. An average value of ^{12}C/^{13}C = 13.3±1.2 with a dispersion σ=6.1±0.8 has been obtained.

Depletion of carbon and of the ^{12}C/^{13}C isotopic abundance ratio and a corresponding enhancement of N with respect to the solar scaled values as measured in the 27 studied RSGs, is consistent with mixing processes in the stellar interiors, that modify the surface abundances of these elements during the post-MS evolution. Stars with progenitor mass in the 9-14 $M_\odot$ range, as for the studied RSGs in the Perseus complex, are indeed expected to have already underwent substantial mixing from the first dredge-up when evolving in the RSG phase.

Fig. 5.9 shows the trend of [C/Fe], [N/Fe], [C/N] abundance ratios with varying the bolometric luminosity and the effective temperature. The rather homogeneous carbon depletion with mild (if any) dependence on the star luminosity and temperature is at variance with the amount of nitrogen enhancement that shows a clear trend with stellar parameters. In particular [N/Fe] increases with increasing luminosity and decreasing temperature. A corresponding larger amount of [C/N] depletion with increasing luminosity and decreasing temperature has been derived, with an average value of [C/N]=-0.56±0.04 dex and a dispersion of σ=0.20±0.03 dex.

Different stellar evolution models (see e.g. Bertelli et al., 2009; Bressan et al., 2012; Chieffi & Limongi, 2013; Choi et al., 2016; Davies & Dessart, 2019; Georgy et al., 2013) predict C depletion by about 0.2 dex after the first dredge-up, in good agreement with the measured values. Models also predict N enhancement by about
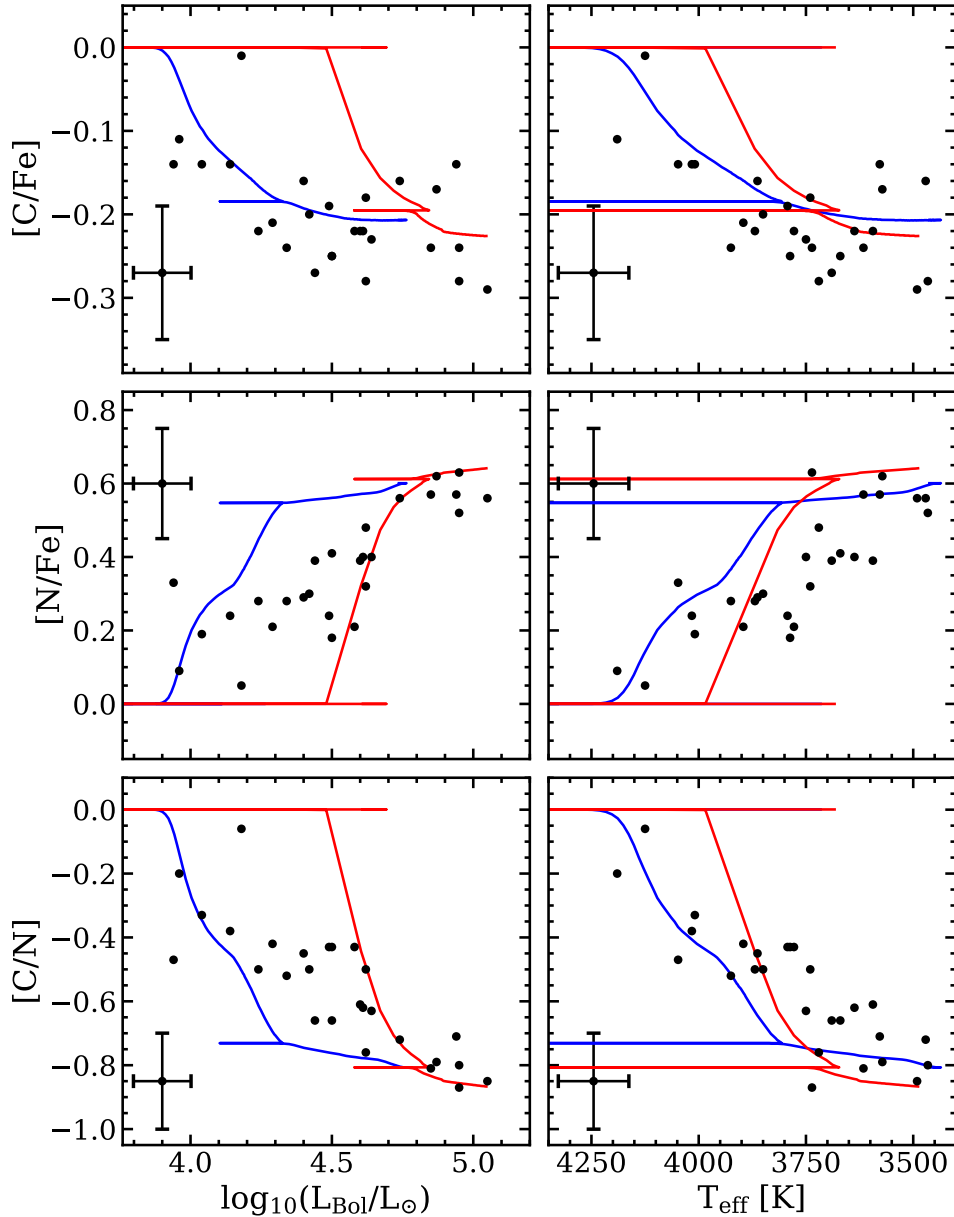
Figure 5.9: [C/Fe], [N/Fe], [C/N] abundance ratios as a function of the stellar luminosity (left panels) and temperature (right panels) for the 27 studied RSGs in the Perseus complex. Values are solar-scaled according to Grevesse & Sauval (1998) solar reference. Typical errorbars are reported in the left upper or lower corner of each panel. For comparison, the PARSEC model predictions for a 9 $M_\odot$ (blue lines) and a 14 $M_\odot$ (red lines) star have been also plotted.
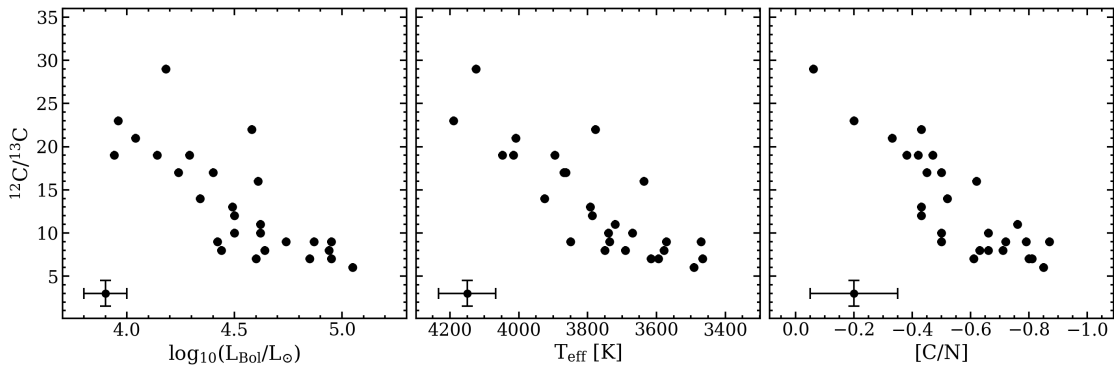
Figure 5.10: ^{12}C/^{13}C ratio as a function of bolometric luminosity (left panel), effective temperature (central panel) and [C/N] abundance ratio. Typical errorbars are reported in the left lower corner of each panel.

0.5-0.6 dex after the first dredge-up. Only the most luminous and coolest RSGs in our sample show such a nitrogen enhancement, while the majority of them show [N/Fe] values increasing from 0.1 to 0.4 dex with increasing luminosity and decreasing temperature. Models also predict a corresponding [C/N] depletion of 0.70-0.80 dex after the first dredge-up, as measured only in the most luminous, coolest RSGs of our sample. This may suggest that N enhancement is more dependent on the stellar mass than the C depletion (see also Davies & Dessart, 2019).

As shown in Fig. 5.10, we also measured the ^{12}C/^{13}C isotopic ratio in all the 27 RSGs analyzed, finding values that progressively decreases from a few tens to below ten with increasing luminosity and decreasing temperature. Only the warmest RSGs show isotopic ratios above 15 as predicted by the majority of models after the first dredge-up, while most of the RSGs with T_{eff} <3800 K show values below 10, possibly requiring some extra-mixing to be explained. Only the Choi et al. (2016) models can possibly reach values as low as 5-10. We also find a nice correlation between depletion of ^{12}C/^{13}C and of [C/N].

5.2.2 Lithium detection

Lithium is a key chemical element to constrain the primordial nucleosynthesis in the Universe. Cyburt et al. (2008) obtained a primordial Li abundance A(Li)=2.72 dex from the theory of big bang nucleosynthesis and the baryon density of WMAP (Dunkley et al., 2009).

In the stellar atmospheres Lithium is detectable only in stars cooler than ∼7000 K. Since the first studies on metal-poor Population II stars by Spite & Spite (1982), in halo stars values of A(Li)≈ 2.2 have been routinely measured (see e.g. Charbonnel & Primas, 2005, and references therein). In young stars of relatively low mass and at solar metallicity, a Lithium abundance A(Li)=3.2 dex has been measured (see e.g. Balachandran et al., 2011; Randich, 2010) and predicted by most recent chemical evolution models (Grisoni et al., 2019), which is in good agreement with the meteoritic solar abundance (Asplund et al., 2009; Grevesse & Sauval, 1998).

Li detection in massive stars is very rare. Indeed, massive MS stars are too hot for Li detection, and more evolved supergiants can suffer significant [if not total] Li disruption due to the development of a convective envelope and the mixing processes. Some early studies of Lithium in yellow and K-type supergiants based on photographic plates (see e.g. Warren, 1973, and references therein) provided upper limits to A(Li) of 1.5-2.0 dex. Gahm & Hultqvist (1976) detected the $\lambda\lambda6708$ doublet absorption in S Per, a M4 RSG of the Perseus complex. More recently, Li abundances A(Li) = 1.3–1.5 have been measured in the two relatively high-mass yellow supergiants, namely HR461 (SpT=KOI) and HR8313 (SpT=G5I) with about solar metallicity by Lyubimkov et al. (2012). Claims for some Li detection in RSGs of the Perseus complex (with masses between 9 and 10 $M_\odot$) have been made by Negueruela et al. (2020) but no measurements have been published so far.

We detected Li doublet and measured its abundance in eight out of the 27 RSGs observed in the Perseus complex. Fig.5.11 shows the HARPS-N spectra in correspondence of the Li doublet for the eight RSGs where it has been detected, and for comparison, those of other RSGs without detection.

The 30% RSGs with detected Li have similar homogeneous half-solar metallicity, 10-30 Myr age and spatial distribution as the other RSGs of the observed sample. They also span a similar wide range of luminosities ($\log_{10}(L/L_\odot$=4-4.6) and T_{eff}=3600-4100 K, i.e. likely the same 9-14 $M_\odot$ mass range, suggesting that stochasticity could affect the possible Li detection in massive stars.

Table 5.5 reports the LTE Li abundances and corresponding errors, together with stellar parameters Fe, CNO, $^{12}C/^{13}C$, O, Na, M and Al abundances (see also Tables 5.2,5.3,5.4). The inferred LTE abundances are quite low, in the $0<\log\epsilon(Li)<1$ dex
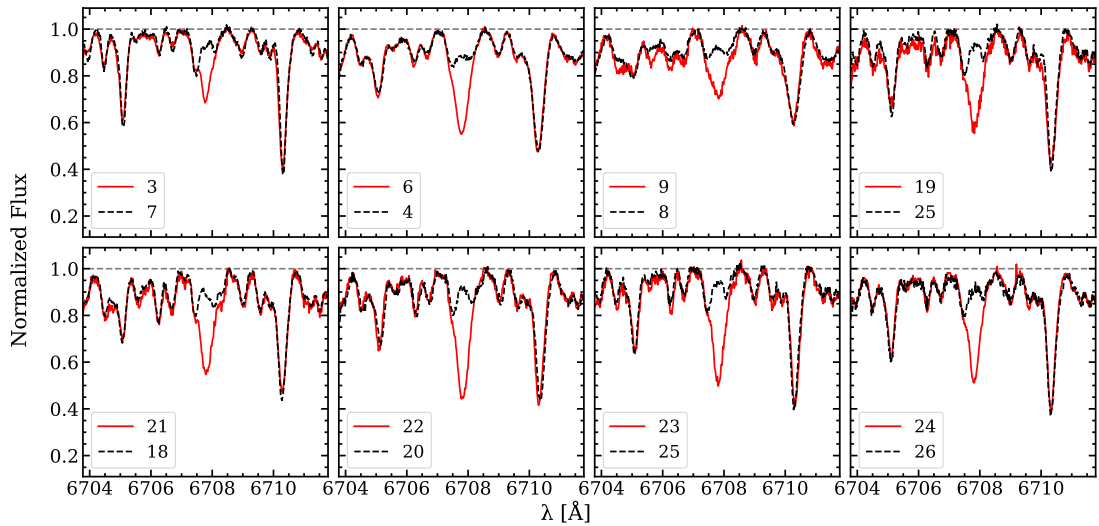
Figure 5.11: HARPS-N high resolution spectra around the LiI doublet at 6707.8 Å for the eight RSGs where Li has been detected (red lines) and for corresponding RSGs with similar stellar parameters but without Li (black dashed lines), for comparison. The star IDs from Fanelli et al. (2022) are marked in the bottom left corner of each panel.

range, and up to 0.5 dex higher if NLTE corrections are applied (see e.g. Lind et al., 2009). These values are about two orders of magnitudes lower than those of primordial nucleosynthesis (Cyburt et al., 2008). For the remaining 19 RSGs in the sample of Fanelli et al. (2022) no reliable detection could be obtained and an upper limit to the Li abundance of $\log\epsilon(\mathrm{Li}){<}{-}0.2$ dex have been obtained.

Fig. 5.12 shows the inferred Li abundance as a function of the stellar luminosity and effective temperature and of the [C/N], $^{12}\mathrm{C}/^{13}\mathrm{C}$, [O/Fe], [Na/Fe], [Mg/Fe] and [Al/Fe] abundance ratios. There is evidence of some anti-correlation between Li abundance and the RSG luminosity and effective temperature, suggesting that Li is more abundant in less luminous and warmer (i.e likely less massive) stars. There is also evidence of some anti-correlation between Li abundance and [C/N] and $^{12}\mathrm{C}/^{13}\mathrm{C}$ abundance ratio depletion, that are probing mixing processes in the stellar interiors, suggesting that Li is more abundant in less mixed stars. At variance, there is no evidence of any trend between Li abundance and [Mg/Fe], [Al/Fe], [O/Fe] and [Na/Fe] abundance ratios, nor of any difference in the distribution of these abundance ratios among RSGs with and without Li detection. The fact that RSGs with and without detected Li show similar [Mg/Fe], [Al/Fe], [O/Fe] and [Na/Fe] distributions with low spread, suggest that the nucleosynthesis of Mg, Al, O and Na in the RSG evolutionary stage should not be significantly altered by HBB in these massive stars.

Table 5.5: Stellar parameters and LTE chemical abundances for the eight RSGs in the Perseus complex with detected Lithium.

#	star	T_{eff}	log(g)	ξ	[Fe/H]	A(C)	A(N)	^{12}C/^{13}C	A(O)	A(Na)	A(Mg)	A(Al)	A(Li)	ϵLi
		K	dex	km s^{-1}	dex	dex	dex	dex	dex	dex	dex	dex	dex	dex
3	V439 Per	3690	0.25	3.40	-0.27	7.98	8.04	8	8.32	6.19	7.31	6.12	0.38	0.09
6	BD+57 540	4125	0.70	2.10	-0.33	8.18	7.64	29	8.46	6.02	7.30	6.25	0.71	0.15
9	T Per	3594	0.01	3.30	-0.31	7.99	8.00	7	8.41	6.18	7.22	6.30	-0.11	0.10
19	WX Cas	3787	0.23	3.00	-0.30	7.97	7.80	12	8.39	6.10	7.27	6.16	0.29	0.09
21	IRAS01530+6149	3793	0.25	2.60	-0.30	8.03	7.86	13	8.56	6.23	7.31	6.25	0.40	0.09
22	BD 61369	3869	0.53	2.60	-0.26	8.04	7.94	17	8.49	6.29	7.30	6.26	0.81	0.13
23	DO 24697	3896	0.50	2.40	-0.24	8.07	7.89	19	8.51	6.26	7.34	6.26	0.68	0.17
24	BD 60287	4009	0.79	2.50	-0.28	8.10	7.83	21	8.56	6.34	7.29	6.32	0.81	0.13

Note: Solar abundance reference for [Fe/H] is from Grevesse & Sauval (1998).
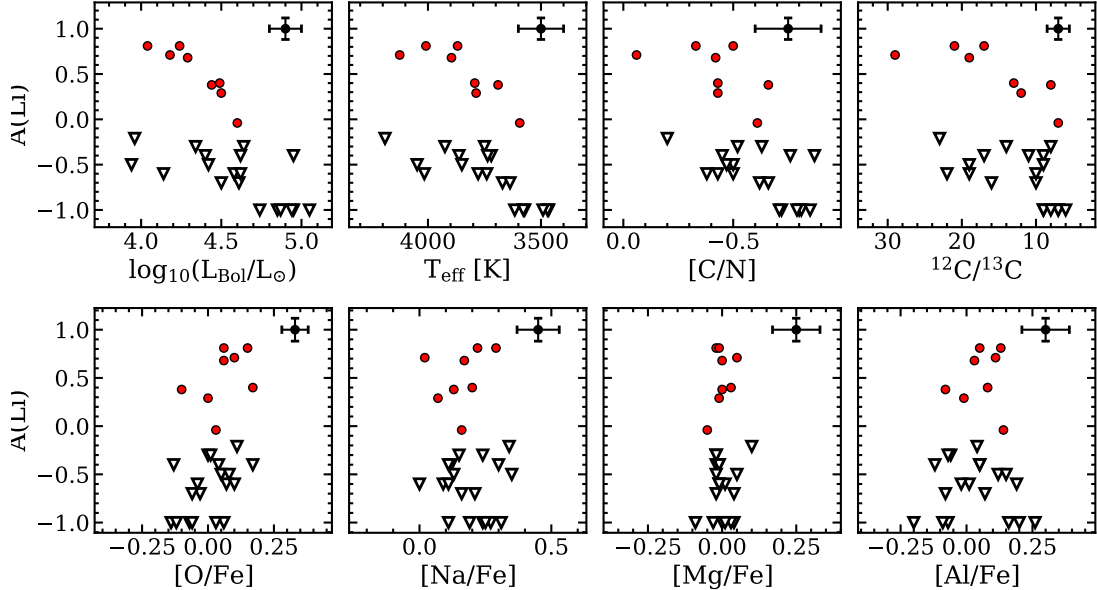
Figure 5.12: Lithium abundances and upper limits as a function of the stellar bolometric luminosity, effective temperature, [C/N], ^{12}C/^{13}C, [O/Fe], [Na/Fe], [Mg/Fe] and [Al/Fe] for the 27 observed RSGs in the Perseus complex. Adapted from Fanelli et al. (2022)

Normally, lithium is expected to be largely depleted in the atmospheres of evolved, massive stars due to convective dilution with the internal layers, where Li is quickly burned. However, in their post-MS evolution, massive stars are expected to experience hot bottom burning (HBB, Sackmann & Boothroyd, 1992), i.e. proton-capture nucleosynthesis at the base of the outer envelope. The HBB process is activated when the temperature at the bottom of the envelope reaches 40 MK and it can alter the abundances of CNO, Na, Al, Mg and of the $^{12}C/^{13}C$ isotopic ratio. At this temperature also the Cameron & Fowler mechanism (Cameron & Fowler, 1971) can act, Be^7 is transformed in Li^7 by electron-capture and transported to cooler layers in the outer atmosphere, where it can temporarily survive. This mechanism has been invoked to explain Li-rich massive Asymptotic Giant Branch (AGB) and super-AGB stars (see e.g. Lyubimkov et al., 2012; Siess, 2010; Ventura et al., 2011; Ventura & D'Antona, 2010, 2011; Ventura et al., 2013, and references therein). In these stars the lithium yield is dramatically dependent on the adopted mass-loss formulation. The RSGs with Li detection have similar homogeneous half-solar metallicity, 10-30 Myr age and spatial distribution as the other RSGs of the observed sample without Li. They also span a similar wide range of luminosities ($\log_{10}(L/L_{\odot}$=4-4.6) and T_{eff}=3600-4100 K, i.e. likely the same 9-14 $M_{\odot}$ mass range. The fact that we detect Li only in 30% of them, may indicate that some stochastic effect could regulate the presence and affect the detection of Li in their atmospheres. Moreover, among the RSGs with detected Li, there is evidence that the progenitor mass and the degree of mixing should matter in determining the amount of Li on the stellar surface, higher abundances being found in somewhat less massive and less mixed RSGs. Given the chemical homogeneity of our sample of RSGs, there is no reason to assume an initial non-homogeneous Lithium abundance in the progenitors, hence mixing should definitely play a role in depleting Li on the stellar surface. Finally, the fact that RSGs with and without detected Li show similar [Mg/Fe], [Al/Fe], [O/Fe] and [Na/Fe] distributions with low spread, suggests that the nucleosynthesis of Mg, Al, O and Na in the RSG evolutionary stage should not not be significantly altered by HBB.

Together with the mixing induced by convection in the post-MS stages, also rotational mixing can be important in depleting Li. Frischknecht et al. 2010 tested their rotational mixing prescriptions by using the Geneva stellar evolution code following the evolution of surface abundances of light elements (Li, Be, and B) in massive stars by using 9, 12, and 15 $M_{\odot}$ models with rotation, from the zero age main sequence up to the RSG phase. They found that massive dwarfs (as the RSG progenitors) that are fast rotators deplete Li already at the end of the MS evolution, while in

slow rotators (i.e. with $v_{in}/v_{crit} \leq 0.1$, corresponding to $\pm$ vsin(i) ≤ 50 km s^{-1}), it is somewhat delayed, occurring in the the Post-MS evolution. Strom et al. (2005) provided rotational velocities in a sample of B0-B9 stars in h, χ Persei, with masses in the 4-15 M$_\odot$, thus including both MS and evolved blue/yellow supergiants (see Sec. 5.1).

In the 9-14 M$_{odot}$ range, only a relatively small fraction of stars are slow rotators with vsin(i)<50 km s^{-1}, the majority of them, either MS or more evolved giants and supergiants, have vsin(i) in the 50-200 km s^{-1} range. Rotational velocities exceeding 200 km s^{-1} have been mostly measured in dwarfs with masses below 9 M$_\odot$. Interestingly, the fraction of RSGs with Li detection is similar to the fraction of slow rotators among the bluest supergiants in our sample as well as in the MS and evolved blue/yellow supergiant sample of Strom et al. (2005). Hence, in the atmospheres of RSGs with likely slow rotator progenitors, Li could have survived the total disruption and/or it could have experienced a secondary production due e.g. to the Cameron & Fowler (Cameron & Fowler, 1971) mechanism, as in less massive AGB and super-AGB stars.

5.3   The global observational framework
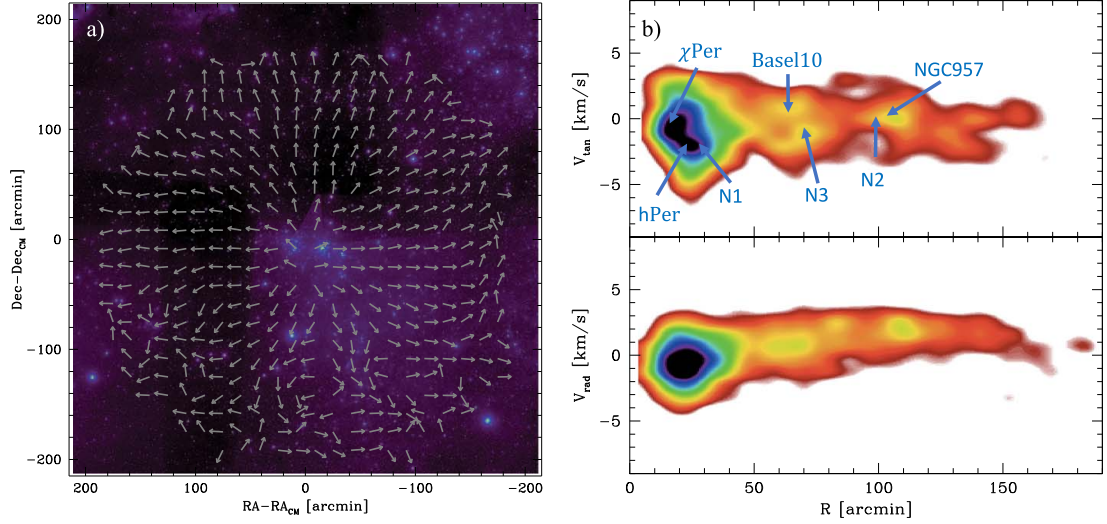
Figure 5.13: Left panel (a): velocity map for stars with G<16 in the LISCA I region superimposed on a Digital Sky Survey two false color image. The typical arrow size corresponds to a velocity of about 1.5 km s^{-1}. Right panels (b): radial (bottom panel) and tangential (upper panel) velocities as a function of the distance from the system barycenter in units of arcmin. The positions of the identified clusters are highlighted with blue arrows. Adapted from Fig. 4 of Dalessandro et al. (2021).

The synergic combination of photometric, astrometric and proper motion information from Gaia and 2MASS with quantitative optical and NIR spectroscopy from the SPA Large Program at the TNG enabled the first, comprehensive evolutionary, kinematic and chemical characterization of the young, evolved stellar populations in the Perseus complex.

The rather homogeneous young age ($\approx$20$\pm$10 Myr), chemical content (half-solar metallicity) and line-of-sight kinematics of the stellar populations of the Perseus complex within a projected area of about 10 degrees in diameter and at a distance of 2-3 kpc, suggest a common origin for the stars either members of denser clusters or distributed in looser associations/diffuse halos. On the other hand, the Gaia proper motion distribution shows that the region is a complex system of substructures physically linked and with possible evidence of co-evolution and interaction. Indeed, by performing a comprehensive study of the stellar kinematics and spectro-photometric properties of the area surrounding h and χ Per double stellar cluster (Dalessandro et al., 2021), we found that the region is populated by seven co-moving clusters, that is h and χ Per, NGC 957, Basel 10, N1, N2, N3, the latter three previously unknown, and by an extended and quite massive halo, defining a
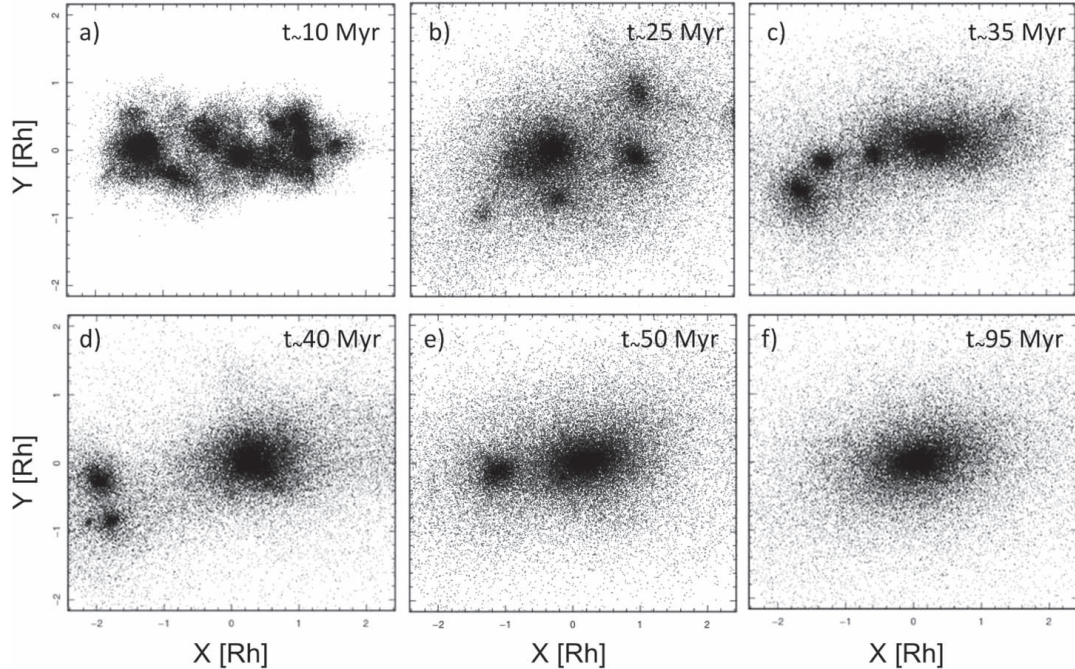
Figure 5.14: Schematic view of N-body simulations of the possible dynamical evolution of a LISCA I-like stellar system in a timeframe of about 100 Myr. X, Y axes are expressed in units of the system half mass radius R_h=56 arcmin. Adapted from Fig. 7 of Dalessandro et al. (2021).

complex structure that we named LISCA I. Fig. 5.13 shows the velocity map for stars in the LISCA I region with signature of expansion together with the tangential and radial velocities as a function of the distance from the system barycenter. The radial component shows a quite narrow distribution slowly increasing as a function of the distance, reaching a peak of about 2 km s^{-1} at R$\sim$100, thus confirming the expansion signal. The tangential velocity component shows a broader distribution, with a slowly declining trend as a function of the distance that can be indicative of a possible large-scale (of the order of some degrees) rotation pattern with an amplitude of 2-3 km s^{-1} (corresponding to about 0.2-0.3 mas yr^{-1}).

The kinematic and structural properties of LISCA I suggest that it might be forming a massive cluster (some 10^5 M$_\odot$) through hierarchical assembly. Fig. 5.14 shows a schematic view of N-body simulations of the possible dynamical evolution of a LISCA I-like stellar system (Dalessandro et al., 2021) in a timeframe of about 100 Myr. Initial small clumps of $\approx$100 M$_\odot$, due to dynamical interactions, mostly dissolve and their stars contribute to the formation of a bound halo. However a number of them can survive total disruption and merge to form sub-structures of 10^3-10^4 M$_\odot$, as those observed in LISCA I, and then eventually they can further merge into a single massive cluster, the expected progenitor of a globular cluster.
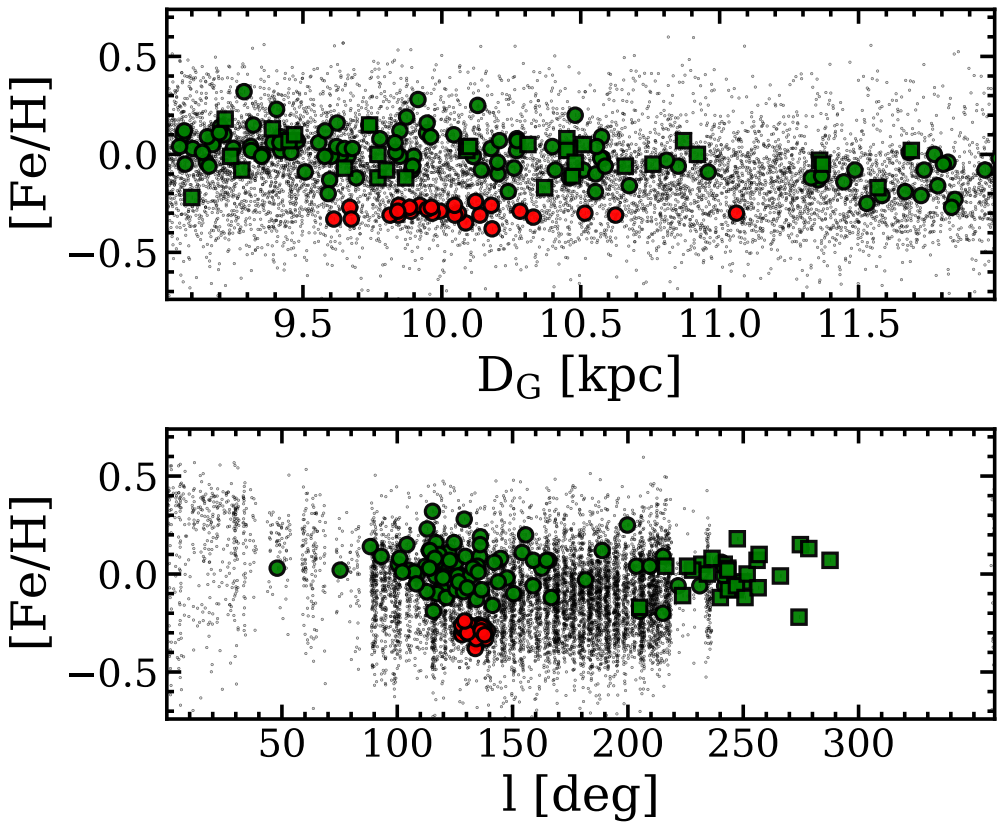
Figure 5.15: Iron abundances as a function of Galactocentric distance, (top panel) and of the Galactic longitude (bottom panel) for the stars within 9 and 11 kpc from the Galactic center, similarly to the the stars in the Perseus complex. Green circles and squares are Cepheids from Genovali et al. (2014) and Kovtyukh et al. (2022), respectively. Grey dots are older stars from the APOGEE DR12 catalog (Holtzman et al., 2015) within ±100 pc from the Galactic plane, according to the Gaia EDR3 (Gaia Collaboration et al., 2021) parallaxes.

Two additional kinematics studies of the other young clusters and associations in the Perseus complex are ongoing.

The present study has also shown the effectiveness of RSGs of K and M spectral types in tracing the detailed chemistry and recent enrichment of their host. To this purpose, the availability of high resolution, high signal-to-noise spectra in the Y,J,H and K NIR bands has been crucial to derive accurate stellar parameters and chemical abundances for the full set of of iron, iron-peak, CNO, alpha and other light and neutron-capture elements. In particular, abundances for Na, Mg, Al, Si, S, K, Ca, Sc, Ti, V, Cr, Mn, Fe, Co, Ni, Cu, Zn, Y, Ce, Dy from atomic lines and C, N, O and F from molecular lines. Despite the low temperatures and gravities of RSGs, optical spectra in a few selected windows less affected by molecular blending
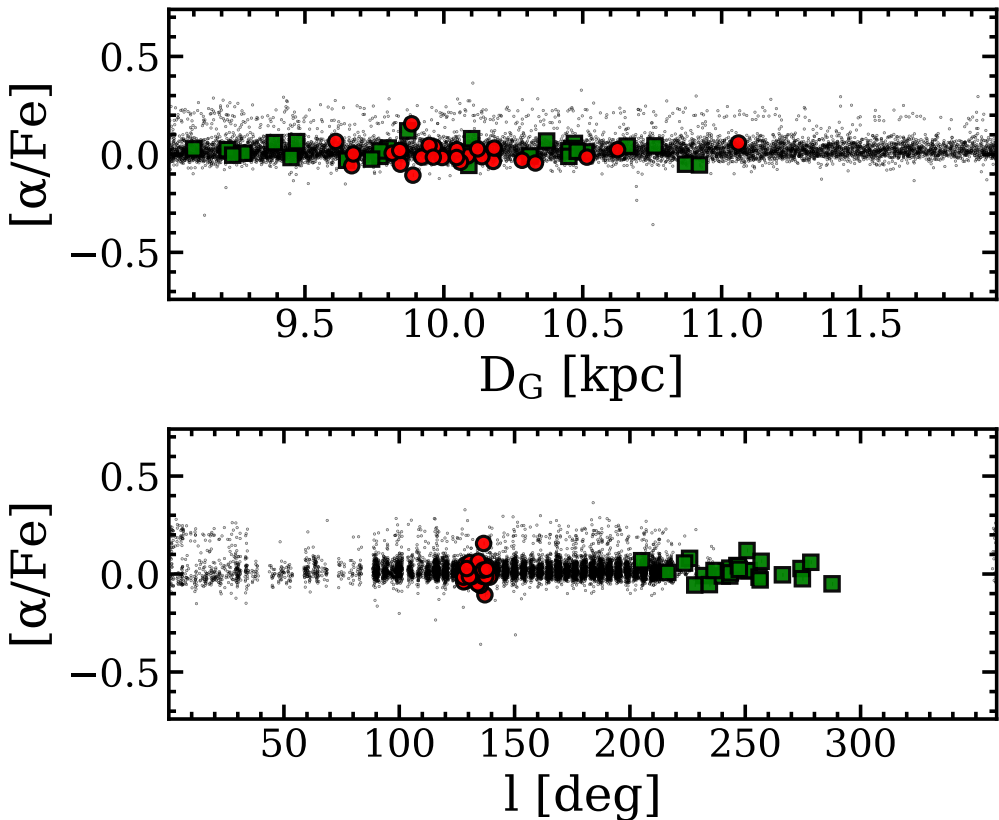
Figure 5.16: [α/Fe] abundance ratio as a function of Galactocentric distance (top panel) and of the Galactic longitude (bottom panel) for the stars with D_{GC} within 9 and 11 kpc from the Galactic center, similarly to the stars in the Perseus complex. Green squares are Cepheids from Kovtyukh et al. (2022). Grey dots are older stars from the APOGEE DR12 catalog (Holtzman et al., 2015) within ± 100 pc from the Galactic plane, according to the Gaia EDR3 (Gaia Collaboration et al., 2021) parallaxes.

and blanketing could also provide some lines for chemical analysis of a sub-set of elements, namely O, Na, Mg, Al, Si, Ca, Sc, Ti, V, Cr, Mn, Fe, Co, Ni, Y, Ce, Dy, and for two neutron-capture elements, namely Zr and Nd, not easily derivable from the few available IR lines, that turn out to be either blended in these cool stars or with uncertain atomic parameters.

It is the first time that a combined high resolution optical and NIR chemical analysis of RSGs has been provided, finding an excellent agreement between optical and NIR abundances for all the elements in common. It is interesting to compare the inferred homogeneous half-solar metallicity of the very young RSGs in the Perseus complex with that of other thin disc stars at similar Galactocentric distances. To this purpose Fig. 5.15 shows metallicities for young Cepheids (Genovali et al., 2014; Kovtyukh et al., 2022) and for older giants (APOGEE DR12 measurements, Holtz-

man et al. 2015) within ± 100 pc from the Galactic plane, according to the Gaia EDR3 parallaxes, as a function of the Galactocentric distance (top) and of the Galactic longitude (bottom) for the sub-sample of stars with Galactocentric distances similar to those of the stars in the Perseus complex, that is between 9 and 11 kpc, in order to check the possible existence of an azimuthal gradient. Metallicity distributions for young Cepheids and older giants are similar, with a mild negative radial gradient of about -0.1 dex kpc^{-1} and some scatter, more significant among the oldest stars. For the stars at Galactocentric distances between 9 and 11 kpc there is no evidence of a significant azimuthal gradient. The metallicity of the young RSGs in the Perseus complex barely fit the lower envelope of those distribution, at [Fe/H]$\approx$-0.3 dex. This is not surprising, indeed the recent (10-30 Myr ago) star formation event that occurred in the Perseus region has been quite intense, at least several 10^5 M$_\odot$ of young stars formed within a relatively small projected area of a few degrees in radius. Qualitatively, such and event likely occurred since a significant amount of fresh, metal poor halo gas was flowing there, and after cooling down and mixing with the existing, processed metal rich gas in the region, collapsed to form the observed RSGs and the other young stars with an overall metallicity slightly lower than that one of the bulk of older stars at similar Galactocentric distances.

RSGs in the Perseus complex, Cepheids and older giants across the thin disc homogeneously show about solar-scaled average abundances for the alpha elements, as also shown in Fig. 5.16, without any appreciable radial or azimuthal gradient. This is consistent with the fact that that the various generations of thin disc stars formed from a gas that since the beginning was already substantially enriched by both the ejecta from type II SNe, providing the alpha and 30-40% iron enrichment, and from Type I sNe, providing the bulk ($>$60%) of iron enrichment.

The detailed chemical study presented in this PhD thesis can also represent an interesting observational test bench to probe models of stellar evolution, nucleosynthesis and internal mixing in the critical RSG evolutionary phase for massive stars at half-solar metallicity, that is in a metallicity regime in between that one of the Solar neighborhood and of the Magellanic Clouds.

The chemical characterization of the warmer stars in the Perseus complex, also observed within the SPA Large Program, is still work in progress. When accomplished, this study will allow us to properly quantify stellar parameters and nucleosynthesis during the blue loop evolution.

Chapter 6

Side applications

*An activity mainly performed during
the Marco Polo fellowship at the
Observatoire de la Cote d'Azur in Nice.*

This PhD thesis work has provided new insights of the astrophysical power of high resolution NIR spectroscopy for the kinematic and chemical characterization of cool stellar populations. In the era of Gaia and major follow-up spectroscopic surveys as well as of major technological advances in the development and performances of NIR instrumentation, the topic is becoming of especially high interest for the stellar community. In particular, this work has attracted the interest of the MOONS community. MOONS is the project of a Multi-Object Optical and Near-infrared Spectrograph fiber-fed that will soon operate at the Nasmyth focus of the VLT.

MOONS is the only new generation multi-object spectrograph foreseen at an 8m-class telescope and it will observe simultaneously in the optical and near-infrared (0.6-1.8 μm), providing spectroscopy at R∼4000-20000 for up to 1,000 targets across a 25 arcmin field-of-view.

The MOONS Consortium will obtain 300 nights of Guaranteed Time Observations (GTO) for dedicated Galactic and extra-galactic surveys.

The Galactic Survey will provide a detailed kinematic and chemical characterization of the resolved stellar populations in the Milky Way and its closest satellites, with the focus on the inner 3 kpc of the Galaxy. This is an environment poorly sampled by previous/ongoing/future spectroscopic surveys at 4m-class telescopes, since stars are faint, due to the high reddening, and an efficient NIR multi-object

spectrograph at an 8m-class telescope is definitely needed.

To this purpose, a high-resolution (R~20,000) setting in the H-band has been included in the design of the instrument for accurate determination of stellar abundances of iron, iron-peak, alpha, light and neutron-capture elements. Additional measurement of chemical abundances and stellar parameters will also be obtained in the RI bands at R 9,000 and in the YJ bands at R~4,000. The Galactic Survey includes two sub-surveys, namely Survey #1 (GS1 ~70 nights) to sample the stellar populations in the inner 3kpc and in a few other Galactic disc regions affected by severe extinction in the visual. Survey #2 (GS2~30 nights) will sample the stellar populations in the central disc/bar region of the Magellanic Clouds (MCs) and in the Sagittarius (Sgr) galaxy and streams.

Within GS1, observations of 15 contiguous fields (see Fig. 6.2) around the Galactic center, covering -1 < l < 1 and -0.5 < b < 0.5 corresponding to a scale height coverage of ~ 50 pc and scale length of ~ 140 pc, will be performed. These specific observations will allow to sample the stellar populations of the nuclear stellar cluster, with a typical extension of 20 pc, and the nuclear disk/bar/bulge. Nuclear stellar clusters and other nuclear sub-structures are known to be present in the centre of nearly 75% of nearby galaxies (Böker et al., 2002; Carollo et al., 1998), but their formation process is still not well understood. In the Milky Way, it is clear that this cluster belongs to a distinct Galactic component. This distinction is possible thanks to the cluster being located at distance of only 8 kpc so we can spatially resolve its stellar populations and kinematics much better than in external galaxies.

Despite the unique astrophysical importance of such an environment, its detailed chemical and kinematic study is in its infancy, since it is very challenging from the observational point of view (Rich et al., 2017; Ryde et al., 2016; Thorsbro et al., 2020). Indeed, this region is affected by a huge total and differential reddening and extreme stellar density, making stars faint also in the NIR and crowding/blending a severe issue.

During this PhD thesis and the Marco Polo fellowship in Nice, I have been involved in a number of preparatory activities for the MOONS Galactic survey and in particular for the observations in the central 200 pc. These activities are briefly described in the next sections.
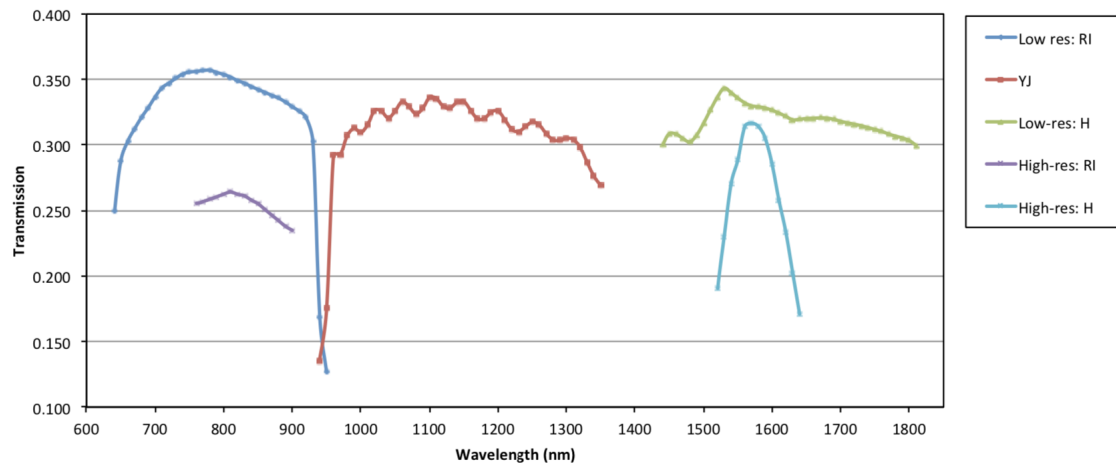
Figure 6.1: Transmission of the MOONS gratings in low and high resolution mode (adapted from Taylor et al., 2018).

6.1 Optimal line lists for chemical analysis with MOONS

The optimal high resolution linelists for chemical analysis obtained from the Arcturus Lab work (see Sect. 4 and Tables in Appendix A) are representing a primary reference for selecting the sub-samples of usable (e.g. sufficiently un-blended and bright but still poorly saturated) lines at the lower spectral resolutions of MOONS for the chemical analysis of red giants.

To this purpose, the `TurboSLine Python` code described in Sect. 3.2 and Tables in Appendix A have been used to select the sub-sample of lines free from major contaminants within one FWHM from their centroids. Then, suitable synthetic spectra at the MOONS spectral resolutions have been computed using the recipes also described in Sect. 3.2 in order to check the actual depth/EW of the selected lines and verifying whether they are reasonably measurable. Fig. 6.1 shows the transmission curves as a function of wavelength of the MOONS gratings. MOONS allows either the acquisition of a low (R≈4-6,000) resolution spectrum over the full 600-1800 nm wavelength range, or the acquisition of a YJ band spectrum at low (R≈4,000) resolution and of a portion of the RI and H band spectra at higher (R≈9,000 and R≈20,000 respectively) resolution. Hence, the following linelists have been compiled.

- Line-low-res-full-spectrum to be used for chemical analysis of spectra in the 600-1800 nm wavelength range at R≈4-6,000.

- Line-high-res-RI-spectrum to be used for chemical analysis of RI band spectra at R≈9,000.

- Line-high-res-H-spectrum to be used for chemical analysis of H band spectra at R≈20,000.
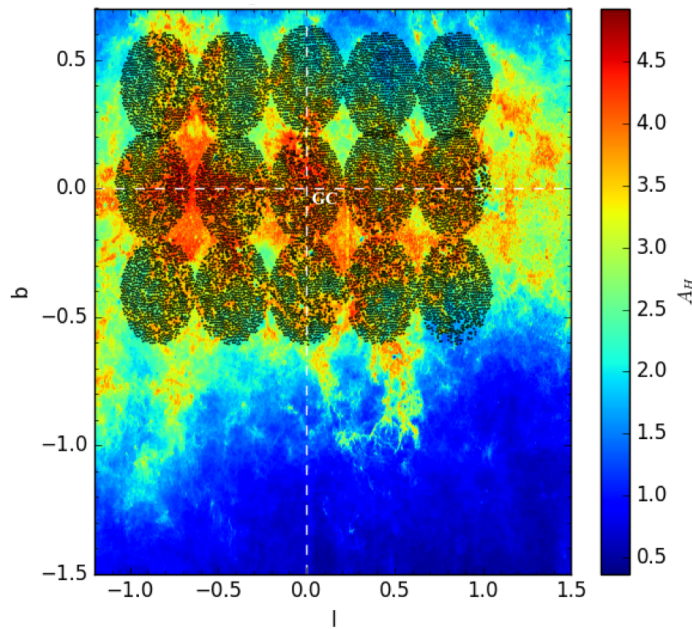
Figure 6.2: Galactic longitude-latitude map of the central 200 pc region around the Galactic center, colour-coded according to the extinction in the H-band, with the location of the foreseen 15 MOONS pointings overimposed.
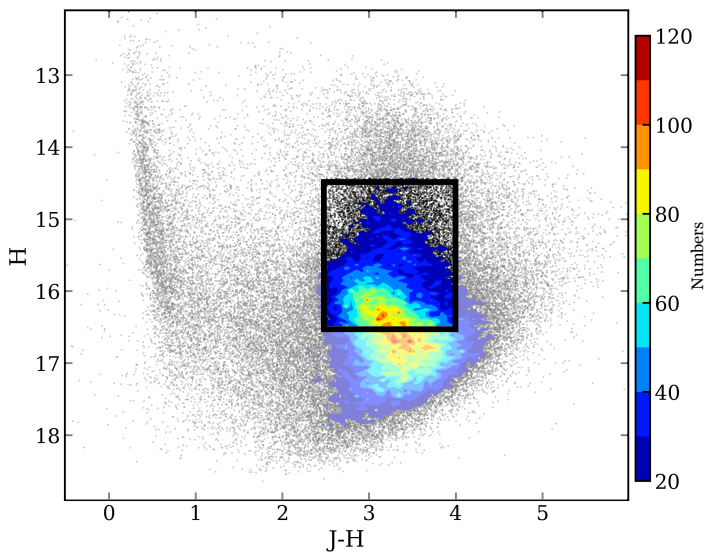
Figure 6.3: Hess H, (J-H) colour-magnitude diagram of the central 10 arcmin around the Galactic center from the VVV (Saito et al., 2012) photometry. The black rectangle marks the region of the CMD where candidate targets will be selected.

6.2 Machine learning techniques for optimal target selection

The selection of suitable giant stars to be observed with MOONS in the central 200 pc of the Galaxy is not trivial because of the extreme density and reddening. Indeed, visual extinctions between 10 and 25 mag are measured.

Fig. 6.2 shows a map of the central 200 pc region around the Galactic center, colour-coded according to the reddening, with superimposed the foreseen 15 MOONS pointings to cover that area.

A first photometric selection in the observed H, (J-H) color-magnitude diagram (see Fig. 6.3) allows to exclude a large fraction of foreground objects with low (if any) reddening. Candidate targets in the nuclear region are giant and Red Clump stars with H-band magnitudes in the 14.5-16.5 range and (J-H) colors in the 2.5-4.0 range.

Each star matching these photometric requirements is then checked against possible blends with close neighbors. Indeed, one of the major problem in the spectroscopic target selection for the galactic center region is the extreme stellar crowding.

Taking into account the typical stellar densities of the galactic center, it is not trivial to find isolated sources and each star in the MOONS field of view needs to be checked against contamination by close neighbors. This requires several hours of computational time. In order to decrease that time down to a few minutes I implemented some machine learning algorithms (taken from the `scikit-learn Python` library) based on decision-tree techniques (Ball et al., 2006; Golob et al., 2021; Vasconcellos et al., 2011).

A decision tree is a system with N input variables and M output variables. The input variables (called attributes) are derived from the observation of the environment (in our case, the field with the star positions). The output variables identify the decision/action to be taken (in our case, the "blend factor"). The decision process is represented with an inverted logic tree where each node is a conditional function. Each node tests a condition (test) on a particular property of the environment (variable) and the process consists of a sequence of tests.

Fig. 6.4 shows the schematic flux diagram. For each pre-selected target star, the code (named `MOONcatLIGHT`) compiles a list of "polluting stars" located within a projected angular distance of ≤1.2 arcsec, i.e. within one fiber diameter, from the target center. With these lists in hand, it is possible to assign a priority flag to each target star, in order to allocate a MOONS fiber. These priority flags are assigned according to the degree of pollution, i.e. depending on the properties of
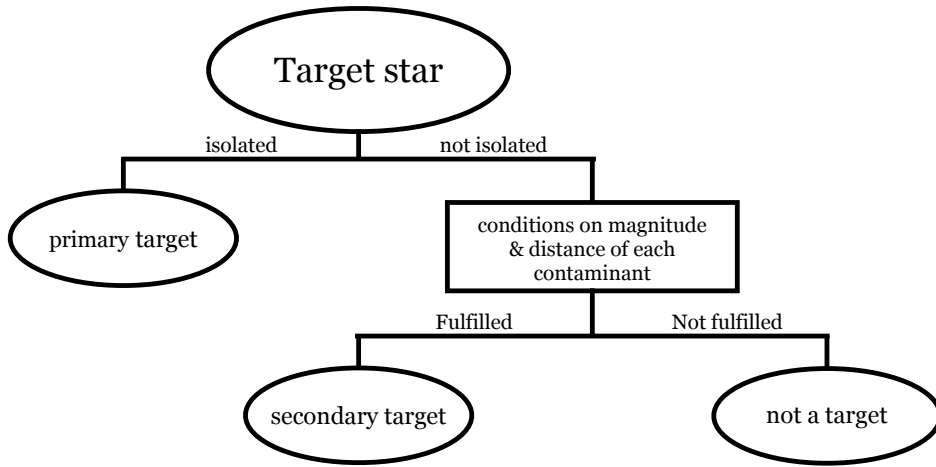
Figure 6.4: Schematic flux diagram of the decision tree process used for selecting optimal targets for MOONS observations.

the polluting stars, such as magnitudes, colours, distance from the target stars, etc. Another important step in the observation preparation is the identification of *empty* sky positions to allocate sky fibers and properly sample the background. These sky fibers should be evenly distributed within the MOONS field of view in order to account for spatial variations e.g. of the unresolved stellar background. For this task I implemented a Monte-Carlo pointing algorithm and the same decision-Tree technique, with also the option to visually inspect the sky fiber allocation.

Chapter **7**

Summary and Conclusions

This Ph.D. work used state-of-the-art high-resolution spectra to provide new insights for the chemical studies study of cool stars and stellar populations. The main results have been described in the previous chapters and they can be summarized as follows.

- Chapter 1 illustrates the astrophysical context and the overall outline of this PhD project.

- Chapter 2 describes the observations and the data reduction techniques which we used for this Ph.D. project. In particular, Arcturus (the calibrator) and massive giants and supergiants in selected regions of the Galactic disc have been observed in the context of the large program *SPA-Stellar Population Astrophysics: the detailed, age-resolved chemistry of the Milky Way disk"*, PI L. Origlia. High resolution stellar spectra were acquired with the HARPS-N and GIANO-B spectrographs mounted on the TNG. Figs. 2.1, 2.2, 2.3 and 2.4 show the Arcturus spectrum in the whole GIANO-B range; Figs. 2.6 and 2.7 show some portions of HARPS-N and GIANO-B spectra of three representative red and blue supergiants of our sample in the Perseus complex.

- Chapter 3 describes the tools and the methodologies with which the spectral analysis has been performed. The first described tool, namely `StarVelox`[2], has been developed for deriving RV with a cross-correlation technique between synthetic and for deriving projected rotational velocities with the Fourier-transform technique. The other developed code is `TurboSLine`, which per-

forms a pre-selection of optimal un-blended lines for chemical analysis and it also enables additional fine-tuning via visual inspection.

- Chapter 4 describes the work published in Fanelli et al. (2021), in which the standard red giant calibrator *Arcturus* was used as a stellar laboratory, for exploring and testing new tools and methods to infer stellar parameters, as well as defining an appropriate lines list for deriving chemical abundances. One of the most important result of this work is the combined use of molecular and atomic features to provide self-consistent stellar parameters, namely the *C-thermometer* described in Sec. 4.1.1 and the *O-gravitometer* described in Sec. 4.1.2.

- Chapter 5 presents new results on the kinematic, evolutionary and chemical properties of the young clusters and associations of the Perseus complex in the outer disc of the Milky Way, as traced by their populations of massive blue and red supergiants. Evidence of co-moving kinematics suggesting an ongoing process of hierarchical cluster assembly has been published in Dalessandro et al. (2021). From a combined optical and NIR study, new results on the evolutionary properties and detailed chemical abundances of an homogeneous sample of RSGs in the Perseus complex have been published in Fanelli et al. (2022). Rather homogeneous, solar-scaled abundances for the majority of the measured elements have been found (Fig. 5.8). At variance, the [C/N] and the $^{12}C/^{13}C$ abundance ratios show some trends with the RSG bolometric luminosities and temperatures (see e.g. Figs. 5.9 and 5.10), probing mixing phenomena in RSGs. Another outstanding result of this analysis (submitted for publication on ApJ Letter) is the detection of the lithium optical doublet in some RSGs (see Sect. 5.2.2), unexpected in these evolved stars since it should have been destroyed by convection and other mixing phenomena. We speculated on the possibility of differential depletion due to differences in the initial rotational velocity, as well as of secondary production due to the Cameron-Fowler mechanism.

- Chapter 6 describes two side applications of this PhD work in the context of the VLT-MOONS project for a multi-object optical and NIR spectrograph, namely *i*) the selection of optimal linelists for chemical analysis in the various grating/resolution configurations and *ii*) the use of machine learning techniques for optimal target selection. This activity was mostly done during the Marco Polo fellowship at the Observatoire de la Cote d'Azur in Nice.

Final remarks

In the James Webb Space Telescope and in the future Extremely Large Telescope era, high-resolution near-IR spectroscopy is becoming a fundamental tool to quantitatively investigate several hot topics in modern planetary, stellar, and extragalactic astrophysics.

In particular, in the field of stellar and Galactic astrophysics, the recent technological advances of the last generation of efficient near-IR spectrographs, are opening new perspectives in the exploration of a new space of stellar and evolutionary parameters as well as of environments where performing quantitative chemical analysis of cool stars and stellar populations.

This Ph.D. work has shown the potential of such an opportunity, by exploring and calibrating a new class of diagnostics for determining stellar parameters and chemical abundances of cool stars and stellar populations also in environments poorly explored so far, since affected by significant dust extinction.

The results for the young Perseus complex also demonstrate the robustness of using RSGs to probe the more recent evolutionary and chemical enrichment history of the Galactic disc, as well as to set the empirical framework where testing models of stellar evolution and nucleosynthesis of massive stars. Several other regions of recent star formation in the Galactic disc at different Galactocentric distances are being investigated within the TNG-SPA Large Program, by using the tools explored and calibrated within this PhD project.

Chapter **A**

Optical and NIR linelists for Arcturus-like stars

Table A.1: Optical atomic lines used for the abundance analysis of Arcturus. Wavelengths are in air

λ_{air} Å	code	χ eV	log gf	λ_{air} Å	code	χ eV	log gf
4813.113	26.00	3.27	-2.89	5230.967	22.00	2.24	-1.19
4847.311	20.00	2.93	-1.40	5235.183	27.00	2.14	-1.47
4865.610	22.01	1.12	-2.70	5238.961	24.00	2.71	-1.47
4872.907	26.00	4.22	-2.30	5239.813	21.01	1.46	-0.77
4873.442	28.00	3.70	-0.38	5241.458	24.00	2.71	-1.92
4873.750	26.00	3.30	-3.06	5246.354	22.00	0.81	-3.10
4874.009	22.01	3.09	-0.86	5247.565	24.00	0.96	-1.50
4874.353	26.00	3.07	-3.03	5247.920	27.00	1.79	-2.07
4875.030	26.00	4.73	-1.12	5249.580	60.01	0.98	0.20
4880.908	22.00	2.15	-0.91	5253.021	26.00	2.28	-3.94
4882.702	27.00	3.25	-0.86	5254.648	27.00	3.97	-0.24
4885.080	22.00	1.89	0.41	5255.330	25.00	3.13	-0.85
4899.514	27.00	2.04	-1.60	5255.505	60.01	0.20	-0.67
4909.757	21.00	2.01	-0.36	5259.973	22.00	2.74	-0.21
4914.380	60.01	0.38	-0.70	5260.387	20.00	2.52	-1.72
4915.229	22.00	1.89	-0.91	5267.269	26.00	4.37	-1.60
4918.012	26.00	4.23	-1.36	5268.334	28.00	4.54	-0.45
4922.265	24.00	3.10	0.38	5268.608	22.01	2.60	-1.61
4924.301	26.00	4.80	-1.50	5274.229	58.01	1.04	0.13
4926.148	22.00	0.82	-2.09	5275.747	24.00	2.89	-0.03
4935.831	28.00	3.94	-0.35	5279.650	26.00	3.30	-3.44
4936.335	24.00	3.11	-0.25	5280.626	27.00	3.63	-0.03
4937.726	22.00	0.81	-2.08	5284.608	26.00	4.19	-2.11
4945.444	28.00	3.80	-0.82	5285.127	26.00	4.43	-1.64
4959.119	60.01	0.06	-0.80	5288.794	22.00	2.43	-0.74
4961.387	60.01	0.63	-0.71	5289.816	39.01	1.03	-1.31
4964.927	24.00	0.94	-2.53	5293.160	60.01	0.82	0.10
4982.130	39.01	1.03	-1.32	5295.776	22.00	1.07	-1.59
4986.222	26.00	4.22	-1.39	5300.011	22.00	1.05	-2.30
4987.160	60.01	0.74	-0.79	5304.180	24.00	3.46	-0.67
4996.367	22.01	1.58	-3.29	5306.460	60.01	0.86	-0.97
4999.112	26.00	4.19	-1.74	5312.856	24.00	3.45	-0.55
5004.043	26.00	4.21	-1.40	5313.237	22.00	1.07	-2.36
5005.167	22.01	1.57	-2.73	5318.349	21.01	1.36	-2.02
5007.730	26.00	4.29	-1.96	5318.771	24.00	3.44	-0.67
5016.477	26.00	4.26	-1.69	5319.810	60.01	0.55	-0.14
5040.614	22.00	0.83	-1.67	5320.036	26.00	3.64	-2.54
5045.414	22.00	0.85	-1.84	5320.783	39.01	1.08	-1.95
5058.496	26.00	3.64	-2.83	5323.928	22.00	0.83	-2.82
5081.574	21.00	1.45	0.47	5325.274	27.00	4.02	0.09
5083.731	21.00	1.44	0.28	5325.552	26.01	3.22	-3.26
5087.419	39.01	1.08	-0.16	5326.790	26.00	4.42	-2.10
5088.153	26.00	4.15	-1.78	5329.784	24.00	2.91	-0.80
5115.777	26.00	3.57	-2.74	5329.989	26.00	4.08	-1.19
5129.156	22.01	1.89	-1.34	5330.556	58.01	0.87	-0.40
5197.567	26.01	3.23	-2.10	5334.240	21.01	1.50	-2.20
5211.530	22.01	2.59	-1.41	5336.786	22.01	1.58	-1.60
5212.688	27.00	3.51	-0.11	5338.306	22.00	0.83	-2.73
5213.806	26.00	3.94	-2.76	5340.447	24.00	3.44	-0.73
5226.539	22.01	1.57	-1.26	5342.701	27.00	4.02	0.74

Continued.

λ_{air} Å	code	χ eV	log gf	λ_{air} Å	code	χ eV	log gf
5344.756	24.00	3.45	-0.99	5483.954	27.00	3.63	-0.48
5349.465	20.00	2.71	-0.31	5484.626	21.00	1.85	0.15
5351.068	22.00	2.78	-0.07	5485.700	60.01	1.26	-0.12
5355.770	21.00	1.95	-0.29	5488.191	22.00	2.40	-0.34
5356.091	21.00	1.86	0.17	5490.147	22.00	1.46	-0.84
5356.970	60.01	1.26	-0.28	5490.693	22.01	1.57	-2.66
5357.199	21.01	1.51	-2.11	5490.846	22.00	0.05	-3.19
5359.200	27.00	4.15	0.24	5491.832	26.00	4.19	-2.19
5361.170	60.01	0.56	-1.48	5492.862	22.01	1.58	-3.31
5366.639	22.00	0.82	-2.59	5496.562	26.00	4.91	-1.73
5369.589	27.00	1.74	-1.65	5512.980	20.00	2.93	-0.46
5375.355	21.00	1.97	-0.05	5514.534	22.00	1.44	-0.50
5376.600	22.00	0.00	-4.00	5517.533	14.00	5.08	-2.61
5376.830	26.00	4.29	-2.31	5523.297	27.00	2.33	-1.64
5377.607	25.00	3.84	-0.17	5526.790	21.01	1.77	0.02
5379.573	26.00	3.69	-1.51	5529.160	26.00	3.64	-2.73
5381.021	22.01	1.57	-1.97	5529.999	22.01	1.58	-3.62
5384.630	22.00	0.83	-2.90	5530.775	27.00	1.71	-2.06
5385.575	26.00	3.69	-2.97	5536.580	26.00	2.83	-3.81
5385.888	60.01	0.74	-0.82	5539.280	26.00	3.64	-2.66
5389.989	22.00	1.87	-1.10	5543.935	26.00	4.22	-1.14
5392.331	28.00	4.15	-1.32	5544.611	39.01	1.74	-0.83
5396.247	22.01	1.58	-3.18	5546.505	26.00	4.37	-1.31
5398.278	26.00	4.45	-0.67	5548.450	60.01	0.55	-1.27
5399.475	25.00	3.85	-0.34	5549.949	26.00	3.69	-2.91
5404.991	24.00	3.38	-0.95	5552.224	21.01	1.46	-2.09
5408.130	27.00	2.28	-2.23	5557.063	13.00	3.14	-2.11
5408.940	22.00	0.00	-3.78	5560.211	26.00	4.43	-1.19
5414.070	26.01	3.22	-3.54	5565.474	22.00	2.24	-0.22
5418.768	22.01	1.58	-2.13	5568.074	26.00	4.15	-2.96
5421.551	60.01	0.38	-1.33	5574.008	23.00	0.04	-3.14
5422.495	22.01	1.57	-3.71	5577.024	26.00	5.03	-1.55
5425.249	26.01	3.20	-3.40	5584.497	23.00	1.06	-1.18
5430.780	60.01	1.22	-0.55	5587.574	26.00	4.14	-1.85
5431.520	60.01	1.12	-0.47	5590.114	20.00	2.52	-0.57
5436.294	26.00	4.39	-1.54	5590.738	27.00	2.04	-1.87
5441.338	26.00	4.31	-1.73	5593.735	28.00	3.90	-0.84
5446.195	21.00	2.01	-0.00	5597.061	26.00	4.99	-2.17
5452.088	26.00	3.64	-2.86	5604.936	23.00	1.04	-1.26
5453.642	22.00	1.44	-1.60	5607.664	26.00	4.15	-2.27
5454.570	27.00	4.07	0.24	5608.972	26.00	4.21	-2.40
5457.457	25.00	2.16	-2.89	5609.960	26.00	3.64	-3.24
5459.682	22.00	1.05	-3.20	5611.356	26.00	3.64	-2.99
5471.192	22.00	1.44	-1.42	5614.773	28.00	4.15	-0.57
5474.223	22.00	1.46	-1.23	5618.632	26.00	4.21	-1.28
5474.730	60.01	0.99	-0.86	5619.224	26.00	3.69	-3.27
5481.861	22.00	1.43	-1.36	5619.595	26.00	4.39	-1.70
5481.991	21.00	1.86	0.27	5624.021	26.00	4.39	-1.48
5483.099	26.00	4.15	-1.41	5624.874	23.00	1.05	-1.05
5483.354	27.00	1.71	-1.49	5625.317	28.00	4.09	-0.70

Continued.

λ_{air} Å	code	χ eV	log gf	λ_{air} Å	code	χ eV	log gf
5626.018	23.00	1.04	-1.26	5705.464	26.00	4.30	-1.35
5627.630	23.00	1.08	-0.35	5708.399	14.00	4.95	-1.47
5628.642	24.00	3.42	-0.74	5708.636	21.00	1.45	-0.64
5630.131	39.00	1.36	0.15	5709.932	26.00	4.26	-2.34
5633.946	26.00	4.99	-0.27	5712.771	24.00	3.01	-1.04
5636.695	26.00	3.64	-2.61	5713.880	22.00	2.29	-0.94
5641.001	21.01	1.50	-1.13	5715.821	20.00	2.71	-3.23
5642.359	24.00	3.86	-0.83	5716.450	22.00	2.30	-0.72
5645.613	14.00	4.93	-2.14	5717.307	21.00	1.44	-0.53
5646.107	23.00	1.05	-1.21	5719.815	24.00	3.01	-1.58
5646.684	26.00	4.26	-2.50	5720.436	22.00	2.29	-0.94
5647.234	27.00	2.28	-1.56	5721.707	26.00	4.15	-2.53
5648.565	22.00	2.50	-0.16	5724.107	21.00	1.43	-0.66
5649.386	24.00	3.84	-0.77	5725.639	23.00	2.37	-0.17
5649.987	26.00	5.10	-0.92	5727.044	23.00	1.08	-0.02
5650.705	26.00	5.09	-0.96	5727.655	23.00	1.05	-0.85
5651.468	26.00	4.47	-2.00	5731.249	23.00	1.06	-0.74
5652.317	26.00	4.26	-1.95	5731.762	26.00	4.26	-1.30
5653.864	26.00	4.39	-1.64	5733.999	23.00	2.36	-0.17
5654.919	14.00	5.61	-1.89	5737.062	23.00	1.06	-0.74
5655.176	26.00	5.06	-0.64	5739.469	22.00	2.25	-0.74
5657.440	23.00	1.06	-1.00	5740.860	60.01	1.16	-0.53
5657.896	21.01	1.51	-0.60	5741.847	26.00	4.26	-1.85
5658.361	21.01	1.50	-1.21	5742.960	26.00	4.18	-2.51
5659.574	26.00	5.09	-0.99	5743.438	23.00	1.08	-0.98
5662.150	22.00	2.32	0.01	5748.351	28.00	1.68	-3.24
5664.030	24.00	3.43	-0.71	5849.683	26.00	3.69	-2.99
5667.149	21.01	1.50	-1.31	5853.148	26.00	1.48	-5.28
5668.362	23.00	1.08	-1.01	5855.075	26.00	4.61	-1.48
5669.042	21.01	1.50	-1.20	5857.451	20.00	2.93	0.24
5670.848	23.00	1.08	-0.43	5858.778	26.00	4.22	-2.26
5671.821	21.00	1.45	0.49	5866.451	22.00	1.07	-0.92
5678.600	26.00	2.42	-4.67	5867.562	20.00	2.93	-1.57
5679.023	26.00	4.65	-0.92	5868.107	66.01	0.00	-2.73
5679.917	22.00	2.47	-0.51	5879.487	26.00	4.61	-2.14
5682.199	28.00	4.11	-0.47	5880.270	22.00	1.05	-2.13
5682.633	11.00	2.10	-0.71	5881.279	26.00	4.61	-1.84
5684.202	21.01	1.51	-1.07	5881.750	26.00	2.18	-5.09
5684.484	14.00	4.95	-1.65	5883.816	26.00	3.96	-1.36
5686.529	26.00	4.55	-0.45	5890.485	27.00	2.04	-2.16
5686.847	21.00	1.44	0.38	5894.092	22.00	0.00	-4.70
5689.460	22.00	2.30	-0.36	5898.215	26.00	4.73	-1.83
5694.740	24.00	3.86	-0.26	5899.293	22.00	1.05	-1.23
5694.983	28.00	4.09	-0.61	5902.472	26.00	4.59	-1.81
5696.088	26.00	4.55	-1.72	5903.315	22.00	1.07	-1.92
5698.519	23.00	1.06	-0.12	5905.671	26.00	4.65	-0.73
5701.104	14.00	4.93	-2.05	5913.728	22.00	0.02	-4.04
5702.660	22.00	2.29	-0.59	5918.536	22.00	1.07	-1.77
5703.575	23.00	1.05	-0.21	5922.110	22.00	1.05	-1.51
5704.732	26.00	5.03	-1.43	5929.677	26.00	4.55	-1.41

Continued.

λ_{air}	code	χ	log gf	λ_{air}	code	χ	log gf
Å		eV		Å		eV	
5930.180	26.00	4.65	-0.23	6120.246	26.00	0.91	-5.95
5937.809	22.00	1.07	-2.07	6122.633	27.00	3.57	-0.85
5940.649	22.00	0.05	-3.65	6125.021	14.00	5.61	-1.47
5940.991	26.00	4.18	-2.15	6126.216	22.00	1.07	-1.21
5943.578	26.00	2.20	-4.19	6127.906	26.00	4.14	-1.40
5944.660	22.00	0.00	-3.85	6128.973	28.00	1.68	-3.43
5948.541	14.00	5.08	-1.23	6130.135	28.00	4.27	-0.96
5952.718	26.00	3.98	-1.44	6131.573	14.00	5.62	-1.56
5953.160	22.00	1.89	-0.14	6131.852	14.00	5.62	-1.62
5965.828	22.00	1.88	-0.23	6135.365	23.00	1.05	-0.76
5975.818	58.01	1.33	-0.45	6142.483	14.00	5.62	-1.30
5976.776	26.00	3.94	-1.24	6145.016	14.00	5.62	-1.31
5978.541	22.00	1.87	-0.31	6146.207	22.00	1.87	-1.48
5984.815	26.00	4.73	-0.20	6149.246	26.01	3.89	-2.80
5999.658	22.00	2.24	-0.85	6149.725	22.00	2.16	-1.44
6002.303	23.00	1.22	-1.79	6154.226	11.00	2.10	-1.55
6005.026	27.00	1.71	-3.32	6156.023	20.00	2.52	-2.51
6007.310	28.00	1.68	-3.40	6160.747	11.00	2.10	-1.25
6012.209	26.00	2.22	-4.04	6161.297	20.00	2.52	-1.27
6018.639	22.00	1.05	-3.02	6163.755	20.00	2.52	-1.29
6027.050	26.00	4.08	-1.09	6166.439	20.00	2.52	-1.14
6031.670	22.00	0.05	-4.01	6169.042	20.00	2.52	-0.80
6039.726	23.00	1.06	-0.65	6169.563	20.00	2.53	-0.48
6043.373	58.01	1.21	-0.48	6175.367	28.00	4.09	-0.53
6053.685	28.00	4.24	-1.07	6176.812	28.00	4.09	-0.26
6054.073	26.00	4.37	-2.31	6178.218	21.01	1.46	-2.84
6058.142	23.00	1.04	-1.40	6187.397	26.00	2.83	-4.16
6064.626	22.00	1.05	-1.80	6189.364	23.00	0.28	-2.97
6076.310	26.00	0.96	-7.21	6195.433	14.00	5.87	-1.57
6078.491	26.00	4.80	-0.32	6199.506	26.00	2.56	-4.43
6081.442	23.00	1.05	-0.61	6204.604	28.00	4.09	-1.08
6082.422	27.00	3.51	-0.52	6210.658	21.00	0.00	-1.53
6086.282	28.00	4.27	-0.53	6213.866	23.00	0.30	-2.05
6086.657	27.00	3.41	-0.83	6220.779	26.00	3.88	-2.46
6090.208	23.00	1.08	-0.07	6224.529	23.00	0.29	-2.01
6091.171	22.00	2.27	-0.45	6226.734	26.00	3.88	-2.22
6091.919	14.00	5.87	-1.46	6230.089	28.00	4.11	-1.26
6092.792	22.00	1.89	-1.38	6233.164	23.00	0.28	-2.07
6093.141	27.00	1.74	-2.44	6237.319	14.00	5.61	-0.97
6093.642	26.00	4.61	-1.50	6239.408	21.00	0.00	-2.27
6094.373	26.00	4.65	-1.94	6239.762	21.00	0.00	-1.78
6096.664	26.00	3.98	-1.93	6242.822	23.00	0.26	-1.59
6098.243	26.00	4.56	-1.88	6243.814	14.00	5.62	-1.24
6098.658	22.00	3.06	-0.01	6245.637	21.01	1.51	-1.02
6105.127	26.00	4.55	-2.05	6247.557	26.01	3.89	-2.40
6111.070	28.00	4.09	-0.87	6251.823	23.00	0.29	-1.37
6111.650	23.00	1.04	-0.74	6253.828	26.00	4.73	-1.66
6113.319	26.01	3.22	-4.20	6256.900	23.00	0.28	-2.02
6116.990	27.00	1.79	-2.49	6257.573	27.00	3.71	-0.72
6119.527	23.00	1.06	-0.36	6257.803	22.00	0.00	-4.06

Continued.

λ_{air} Å	code	χ eV	log gf	λ_{air} Å	code	χ eV	log gf
5930.180	26.00	4.65	-0.23	6120.246	26.00	0.91	-5.95
5937.809	22.00	1.07	-2.07	6122.633	27.00	3.57	-0.85
5940.649	22.00	0.05	-3.65	6125.021	14.00	5.61	-1.47
5940.991	26.00	4.18	-2.15	6126.216	22.00	1.07	-1.21
5943.578	26.00	2.20	-4.19	6127.906	26.00	4.14	-1.40
5944.660	22.00	0.00	-3.85	6128.973	28.00	1.68	-3.43
5948.541	14.00	5.08	-1.23	6130.135	28.00	4.27	-0.96
5952.718	26.00	3.98	-1.44	6131.573	14.00	5.62	-1.56
5953.160	22.00	1.89	-0.14	6131.852	14.00	5.62	-1.62
5965.828	22.00	1.88	-0.23	6135.365	23.00	1.05	-0.76
5975.818	58.01	1.33	-0.45	6142.483	14.00	5.62	-1.30
5976.776	26.00	3.94	-1.24	6145.016	14.00	5.62	-1.31
5978.541	22.00	1.87	-0.31	6146.207	22.00	1.87	-1.48
5984.815	26.00	4.73	-0.20	6149.246	26.01	3.89	-2.80
5999.658	22.00	2.24	-0.85	6149.725	22.00	2.16	-1.44
6002.303	23.00	1.22	-1.79	6154.226	11.00	2.10	-1.55
6005.026	27.00	1.71	-3.32	6156.023	20.00	2.52	-2.51
6007.310	28.00	1.68	-3.40	6160.747	11.00	2.10	-1.25
6012.209	26.00	2.22	-4.04	6161.297	20.00	2.52	-1.27
6018.639	22.00	1.05	-3.02	6163.755	20.00	2.52	-1.29
6027.050	26.00	4.08	-1.09	6166.439	20.00	2.52	-1.14
6031.670	22.00	0.05	-4.01	6169.042	20.00	2.52	-0.80
6039.726	23.00	1.06	-0.65	6169.563	20.00	2.53	-0.48
6043.373	58.01	1.21	-0.48	6175.367	28.00	4.09	-0.53
6053.685	28.00	4.24	-1.07	6176.812	28.00	4.09	-0.26
6054.073	26.00	4.37	-2.31	6178.218	21.01	1.46	-2.84
6058.142	23.00	1.04	-1.40	6187.397	26.00	2.83	-4.16
6064.626	22.00	1.05	-1.80	6189.364	23.00	0.28	-2.97
6076.310	26.00	0.96	-7.21	6195.433	14.00	5.87	-1.57
6078.491	26.00	4.80	-0.32	6199.506	26.00	2.56	-4.43
6081.442	23.00	1.05	-0.61	6204.604	28.00	4.09	-1.08
6082.422	27.00	3.51	-0.52	6210.658	21.00	0.00	-1.53
6086.282	28.00	4.27	-0.53	6213.866	23.00	0.30	-2.05
6086.657	27.00	3.41	-0.83	6220.779	26.00	3.88	-2.46
6090.208	23.00	1.08	-0.07	6224.529	23.00	0.29	-2.01
6091.171	22.00	2.27	-0.45	6226.734	26.00	3.88	-2.22
6091.919	14.00	5.87	-1.46	6230.089	28.00	4.11	-1.26
6092.792	22.00	1.89	-1.38	6233.164	23.00	0.28	-2.07
6093.141	27.00	1.74	-2.44	6237.319	14.00	5.61	-0.97
6093.642	26.00	4.61	-1.50	6239.408	21.00	0.00	-2.27
6094.373	26.00	4.65	-1.94	6239.762	21.00	0.00	-1.78
6096.664	26.00	3.98	-1.93	6242.822	23.00	0.26	-1.59
6098.243	26.00	4.56	-1.88	6243.814	14.00	5.62	-1.24
6098.658	22.00	3.06	-0.01	6245.637	21.01	1.51	-1.02
6105.127	26.00	4.55	-2.05	6247.557	26.01	3.89	-2.40
6111.070	28.00	4.09	-0.87	6251.823	23.00	0.29	-1.37
6111.650	23.00	1.04	-0.74	6253.828	26.00	4.73	-1.66
6113.319	26.01	3.22	-4.20	6256.900	23.00	0.28	-2.02
6116.990	27.00	1.79	-2.49	6257.573	27.00	3.71	-0.72
6119.527	23.00	1.06	-0.36	6257.803	22.00	0.00	-4.06

Continued.

λ_{air} Å	code	χ eV	log gf	λ_{air} Å	code	χ eV	log gf
6258.102	22.00	1.44	-0.39	6531.421	23.00	1.22	-0.85
6264.810	22.00	1.74	-2.26	6533.928	26.00	4.56	-1.46
6266.010	22.00	1.75	-1.95	6543.504	23.00	1.19	-1.71
6266.307	23.00	0.28	-2.29	6554.223	22.00	1.44	-1.15
6268.525	22.00	1.43	-2.26	6555.462	14.00	5.98	-1.16
6271.277	26.00	3.33	-2.70	6556.062	22.00	1.46	-1.06
6273.388	22.00	0.02	-4.01	6559.563	22.01	2.05	-2.17
6274.652	23.00	0.27	-1.70	6560.566	14.00	5.96	-1.41
6276.295	21.00	0.02	-2.60	6581.209	26.00	1.48	-4.68
6285.160	23.00	0.28	-1.54	6583.708	14.00	5.95	-1.74
6290.542	26.00	2.59	-4.33	6595.864	27.00	3.71	-0.55
6300.304	8.00	0.00	-9.78	6598.598	28.00	4.24	-0.98
6300.698	21.01	1.51	-1.90	6599.105	22.00	0.90	-1.72
6305.657	21.00	0.02	-1.24	6604.601	21.01	1.36	-1.31
6309.920	21.01	1.50	-1.62	6606.950	22.01	2.06	-2.80
6312.236	22.00	1.46	-1.55	6608.024	26.00	2.28	-4.03
6318.717	12.00	5.11	-2.10	6632.439	27.00	2.28	-2.00
6319.237	12.00	5.11	-2.32	6633.748	26.00	4.56	-0.80
6320.851	21.01	1.50	-1.82	6646.930	26.00	2.61	-3.99
6322.166	28.00	4.15	-1.17	6653.851	26.00	4.15	-2.52
6325.164	22.00	0.02	-3.76	6661.075	24.00	4.19	-0.19
6326.836	23.00	1.87	-0.76	6667.417	26.00	2.45	-4.40
6327.599	28.00	1.68	-3.17	6678.569	22.00	2.25	-1.36
6330.091	24.00	0.94	-2.92	6678.809	27.00	1.96	-2.68
6336.099	22.00	1.44	-1.69	6680.134	22.01	3.09	-1.89
6338.875	26.00	4.80	-1.06	6689.260	22.00	2.25	-1.67
6359.888	22.00	0.05	-4.07	6696.023	13.00	3.14	-1.35
6362.338	30.00	5.79	0.15	6698.673	13.00	3.14	-1.65
6369.459	26.01	2.89	-4.29	6703.565	26.00	2.76	-3.16
6370.346	28.00	3.54	-1.94	6710.317	26.00	1.48	-4.88
6378.250	28.00	4.15	-0.82	6713.742	26.00	4.80	-1.60
6378.807	21.00	0.00	-2.42	6725.355	26.00	4.10	-2.30
6385.718	26.00	4.73	-1.91	6726.666	26.00	4.61	-1.09
6392.538	26.00	2.28	-4.03	6733.150	26.00	4.64	-1.58
6395.472	22.00	1.50	-2.54	6739.520	26.00	1.56	-4.79
6419.088	22.00	2.17	-1.53	6745.100	26.00	4.58	-2.16
6432.676	26.01	2.89	-3.52	6745.544	22.00	2.24	-1.23
6436.405	26.00	4.19	-2.46	6746.953	26.00	2.61	-4.35
6449.808	20.00	2.52	-0.50	6757.150	16.00	7.87	-0.24
6454.994	27.00	3.63	-0.25	6772.315	28.00	3.66	-0.98
6455.598	20.00	2.52	-1.34	6784.256	13.00	4.02	-1.28
6456.379	26.01	3.90	-2.20	6786.858	26.00	4.19	-2.07
6471.662	20.00	2.53	-0.69	6798.479	20.00	2.71	-2.54
6477.859	27.00	3.77	-0.61	6804.271	26.00	4.58	-1.81
6482.798	28.00	1.94	-2.63	6806.842	26.00	2.73	-3.21
6493.781	20.00	2.52	-0.11	6837.005	26.00	4.59	-1.69
6497.684	22.00	1.44	-2.02	6839.830	26.00	2.56	-3.45
6499.650	20.00	2.52	-0.82	6841.338	26.00	4.61	-0.75
6508.121	22.00	1.43	-2.03	6842.685	26.00	4.64	-1.32
6527.202	14.00	5.87	-1.07	6851.635	26.00	1.61	-5.32

Continued.

λ_{air} Å	code	χ eV	log gf	λ_{air} Å	code	χ eV	log gf
6854.823	26.00	4.59	-1.93	7132.986	26.00	4.08	-1.63
6855.161	26.00	4.56	-0.74	7148.150	20.00	2.71	0.14
6857.249	26.00	4.08	-2.15	7188.566	22.00	1.43	-1.71
6858.148	26.00	4.61	-0.93	7209.436	22.00	1.46	-0.43
6859.479	26.00	2.85	-4.52	7214.729	22.01	2.59	-1.74
6860.283	26.00	2.61	-4.15	7219.682	26.00	4.08	-1.69
6861.445	22.00	2.27	-0.73	7226.208	14.00	5.61	-1.51
6861.937	26.00	2.42	-3.89	7251.709	22.00	1.43	-0.76
6864.311	26.00	4.56	-2.32	7275.296	14.00	5.62	-0.85
6882.512	24.00	3.44	-0.38	7284.834	26.00	4.14	-1.75
6883.052	24.00	3.44	-0.42	7326.145	20.00	2.93	-0.21
6894.918	12.00	5.75	-1.64	7326.458	25.00	4.43	-0.25
6911.082	19.00	1.61	-1.42	7337.730	22.00	2.24	-1.41
6911.511	26.00	2.42	-4.04	7351.512	26.00	4.96	-0.64
6916.680	26.00	4.15	-1.45	7352.124	22.00	2.49	-1.04
6924.179	24.00	3.45	-0.09	7355.890	24.00	2.89	-0.28
6925.271	24.00	3.45	-0.33	7375.246	14.00	6.19	-1.05
6971.932	26.00	3.02	-3.34	7385.238	28.00	2.74	-2.07
6976.513	14.00	5.95	-1.17	7400.179	24.00	2.90	-0.11
6976.922	26.00	4.58	-1.85	7409.342	28.00	3.80	-0.14
6977.428	26.00	4.59	-1.56	7418.320	26.00	4.14	-2.93
6978.397	24.00	3.46	0.18	7418.666	26.00	4.14	-1.38
6979.159	26.00	2.83	-4.21	7422.275	28.00	3.64	-0.14
6980.903	24.00	3.46	-1.12	7423.183	22.00	1.44	-2.65
6988.523	26.00	2.40	-3.66	7423.497	14.00	5.62	-0.18
6992.878	14.00	5.87	-1.45	7430.538	26.00	2.59	-3.86
7000.614	26.00	4.14	-2.39	7435.591	26.00	5.31	-0.72
7001.541	28.00	1.94	-3.55	7440.911	26.00	4.91	-0.57
7003.569	14.00	5.96	-0.89	7443.021	26.00	4.19	-1.82
7014.986	26.00	2.45	-4.25	7453.997	26.00	4.19	-2.41
7017.653	14.00	5.87	-1.03	7461.520	26.00	2.56	-3.58
7022.952	26.00	4.19	-1.25	7472.750	26.00	5.35	-0.99
7030.011	28.00	3.54	-1.73	7473.554	26.00	4.61	-1.87
7034.372	28.00	3.54	-2.01	7476.375	26.00	4.80	-1.68
7034.900	14.00	5.87	-0.88	7481.739	26.00	2.76	-4.10
7050.688	22.00	2.34	-1.20	7491.647	26.00	4.30	-0.90
7062.956	28.00	1.95	-3.42	7514.198	26.00	5.31	-0.87
7065.212	22.00	1.46	-2.22	7525.110	28.00	3.64	-0.43
7068.409	26.00	4.08	-1.38	7540.429	26.00	2.73	-3.85
7069.531	26.00	2.56	-4.34	7547.309	12.00	5.93	-1.68
7083.395	26.00	4.91	-1.20	7547.896	26.00	5.10	-1.35
7084.643	13.00	4.02	-0.96	7551.104	26.00	5.09	-1.63
7086.725	26.00	3.60	-2.36	7555.597	28.00	3.85	0.05
7103.145	26.00	2.43	-4.49	7568.898	26.00	4.28	-0.77
7112.167	26.00	2.99	-3.00	7574.042	28.00	3.83	-0.45
7114.548	26.00	2.69	-4.01	7582.121	26.00	4.96	-1.75
7118.096	26.00	5.01	-1.57	7669.710	14.00	6.19	-0.80
7127.567	26.00	4.99	-1.05	7680.266	14.00	5.86	-0.69
7130.304	22.00	1.46	-2.32	7688.396	14.00	6.19	-1.22
7130.920	26.00	4.22	-0.79	7698.964	19.00	0.00	-0.15

Continued.

λ_{air} Å	code	χ eV	log gf	λ_{air} Å	code	χ eV	log gf
7712.663	27.00	2.54	-1.57	8698.706	26.00	2.99	-3.44
7723.207	26.00	2.28	-3.62	8699.454	26.00	4.96	-0.38
7745.513	26.00	5.09	-1.17	8719.577	22.00	1.74	-2.30
7748.884	28.00	3.71	-0.18	8727.140	6.00	1.26	-8.16
7751.108	26.00	4.99	-0.75	8728.010	14.00	6.18	-0.27
7767.443	22.00	0.90	-3.18	8729.143	26.00	3.41	-2.87
7790.317	22.00	3.18	-0.67	8734.711	22.00	1.05	-2.24
7797.580	28.00	3.90	-0.18	8742.445	14.00	5.87	-0.07
7802.473	26.00	5.09	-1.33	8747.425	26.00	3.02	-3.17
7807.908	26.00	4.99	-0.54	8755.749	26.00	5.35	-1.47
7835.309	13.00	4.02	-0.65	8763.966	26.00	4.65	-0.15
7836.134	13.00	4.02	-0.49	8766.680	22.00	1.07	-2.27
7838.126	27.00	3.97	-0.30	8772.865	13.00	4.02	-0.32
7844.558	26.00	4.83	-1.81	8773.896	13.00	4.02	-0.16
7855.399	26.00	5.06	-1.02	8793.342	26.00	4.61	-0.09
7863.786	28.00	4.54	-0.89	8804.624	26.00	2.28	-3.23
7922.023	22.00	2.47	-1.71	8808.170	26.00	5.01	-1.08
7925.852	14.00	6.22	-0.91	8834.017	26.00	4.22	-2.59
7993.600	22.00	1.87	-2.38	8841.277	13.00	4.09	-1.59
7996.435	22.00	3.34	0.37	8846.740	26.00	5.01	-0.78
8007.226	27.00	4.15	0.18	8862.049	26.00	5.36	-0.88
8024.843	22.00	1.88	-1.08	8862.548	28.00	4.09	-0.40
8071.284	14.00	6.10	-1.19	8863.587	26.00	4.97	-1.52
8092.631	29.00	3.82	-0.13	8866.931	26.00	4.55	0.08
8098.724	12.00	5.95	-1.17	8868.430	26.00	3.02	-2.91
8129.312	26.00	2.76	-4.28	8876.024	26.00	5.02	-1.05
8207.741	26.00	4.45	-0.86	8878.250	26.00	2.99	-3.38
8239.127	26.00	2.42	-3.18	8923.569	12.00	5.39	-1.68
8293.513	26.00	3.30	-2.17	8925.295	14.00	5.95	-1.35
8331.913	26.00	4.39	-0.55	8946.260	26.00	2.85	-3.51
8345.186	26.00	2.69	-4.69	8950.188	26.00	4.15	-2.42
8353.162	22.00	0.81	-2.62	8976.865	24.00	3.09	-1.03
8365.631	26.00	3.25	-2.05	8978.197	26.00	3.41	-3.46
8372.792	27.00	4.07	-0.04	8979.192	22.01	2.59	-1.98
8438.922	22.00	2.26	-0.70	8984.886	26.00	5.10	-0.92
8442.975	22.00	2.25	-1.64	8997.153	12.00	5.93	-1.77
8450.892	22.00	2.25	-0.80	9012.074	26.00	4.99	-0.31
8455.271	24.00	2.71	-2.24	9013.977	26.00	2.28	-3.84
8467.147	22.00	2.12	-1.10	9022.010	14.00	6.27	-1.11
8481.980	26.00	4.19	-2.00	9037.613	23.00	1.18	-2.12
8515.108	26.00	3.02	-2.07	9051.451	14.00	6.27	-0.99
8518.027	22.00	2.13	-0.94	9084.184	26.00	4.26	-2.24
8682.983	22.00	1.05	-1.79	9228.093	16.00	6.52	0.32
8686.352	14.00	6.21	-0.81	9237.538	16.00	6.52	0.01

Table A.2: NIR atomic lines used for the abundance analysis of Arcturus. Wavelengths are in air.

λ_air Å	code	χ eV	log gf	λ_air Å	code	χ eV	log gf
9653.114	26.00	4.73	-0.68	10273.684	20.00	4.53	-0.64
9657.232	26.00	5.09	-0.78	10288.944	14.00	4.92	-1.51
9663.241	22.00	2.29	-1.71	10299.290	12.00	6.12	-2.08
9688.873	22.00	0.81	-1.61	10302.611	28.00	4.27	-0.88
9718.960	22.00	1.50	-1.18	10313.197	14.00	6.40	-0.89
9730.316	24.00	3.55	-0.77	10330.228	28.00	4.11	-0.98
9746.920	22.00	2.32	-1.08	10332.327	26.00	3.64	-2.94
9753.091	26.00	4.80	-0.78	10340.885	26.00	2.20	-3.58
9763.896	26.00	5.03	-0.74	10343.819	20.00	2.93	-0.30
9770.301	22.00	0.85	-1.58	10347.965	26.00	5.39	-0.55
9773.353	24.00	3.56	-1.56	10353.804	26.00	5.39	-0.82
9786.641	26.00	4.61	-1.68	10364.062	26.00	5.45	-0.96
9787.688	22.00	0.83	-1.44	10371.263	14.00	4.93	-0.70
9800.308	26.00	5.09	-0.45	10378.602	28.00	4.09	-0.79
9811.504	26.00	5.01	-1.36	10378.999	26.00	2.22	-4.15
9832.140	22.00	1.89	-1.13	10382.306	27.00	2.87	-2.16
9868.186	26.00	5.09	-0.98	10395.794	26.00	2.18	-3.39
9879.583	22.00	1.87	-2.40	10396.802	22.00	0.85	-1.54
9881.522	26.00	4.58	-1.71	10407.037	14.00	6.62	-0.60
9889.035	26.00	5.03	-0.45	10416.620	24.00	3.01	-2.51
9904.480	24.00	3.55	-1.64	10423.027	26.00	2.69	-3.62
9927.351	22.00	1.88	-1.29	10423.743	26.00	3.07	-2.92
9941.379	22.00	2.16	-1.87	10435.355	26.00	4.73	-1.95
9944.206	26.00	5.01	-1.34	10455.470	16.00	6.86	0.25
9980.463	26.00	5.03	-1.38	10456.790	16.00	6.86	-0.45
9997.959	22.00	1.87	-1.56	10459.460	16.00	6.86	0.03
10003.088	22.00	2.16	-1.21	10460.049	22.00	2.26	-1.40
10005.664	22.00	1.07	-3.65	10469.652	26.00	3.88	-1.18
10011.744	22.00	2.15	-1.39	10486.250	24.00	3.01	-0.95
10034.491	22.00	1.46	-1.77	10496.113	22.00	0.84	-1.65
10046.414	27.00	2.72	-2.08	10510.010	24.00	3.01	-1.53
10048.828	22.00	1.44	-1.93	10523.390	66.01	1.95	-0.45
10058.252	26.00	2.20	-5.22	10529.524	15.00	6.95	0.24
10059.904	22.00	1.43	-2.08	10530.514	28.00	4.11	-1.19
10061.245	28.00	5.49	-0.40	10532.234	26.00	3.93	-1.48
10065.045	26.00	4.83	-0.29	10551.757	22.00	1.89	-2.42
10066.512	22.00	2.16	-1.85	10552.965	22.00	2.25	-1.57
10068.329	14.00	6.10	-1.32	10555.649	26.00	5.45	-1.11
10077.174	26.00	2.99	-4.27	10565.952	22.00	2.24	-1.78
10080.350	24.00	3.56	-1.27	10577.139	26.00	3.30	-3.14
10081.393	26.00	2.42	-4.54	10581.577	15.00	6.99	0.45
10086.242	26.00	2.95	-4.05	10582.160	14.00	6.22	-1.17
10155.162	26.00	2.18	-4.23	10584.633	22.00	0.83	-1.77
10167.468	26.00	2.20	-4.12	10607.718	22.00	0.85	-2.70
10193.224	28.00	4.09	-0.66	10611.686	26.00	6.17	0.02
10195.105	26.00	2.73	-3.58	10616.721	26.00	3.27	-3.13
10216.313	26.00	4.73	-0.06	10647.640	24.00	3.01	-1.58
10218.408	26.00	3.07	-2.76	10661.623	22.00	0.82	-1.92
10245.217	39.01	1.74	-1.82	10667.520	24.00	3.01	-1.48
10265.217	26.00	2.22	-4.54	10672.140	24.00	3.01	-1.35

Continued.

λ_{air} Å	code	χ eV	log gf	λ_{air} Å	code	χ eV	log gf
10677.047	22.00	0.84	-2.52	11422.319	26.00	2.20	-2.70
10689.716	14.00	5.95	-0.12	11473.020	24.00	3.32	-0.52
10694.251	14.00	5.96	0.05	11572.523	26.00	6.28	0.32
10725.185	26.00	3.64	-2.76	11588.684	28.00	4.24	-1.21
10726.391	22.00	0.81	-2.06	11592.289	14.00	6.27	-0.55
10727.406	14.00	5.98	0.22	11593.588	26.00	2.22	-2.45
10732.864	22.00	0.83	-2.52	11594.546	26.00	4.58	-1.88
10746.449	11.00	3.19	-1.29	11607.572	26.00	2.20	-2.01
10754.753	26.00	2.83	-4.52	11609.802	14.00	6.26	-1.06
10768.365	13.00	4.09	-2.02	11610.560	24.00	3.32	0.06
10774.866	22.00	0.82	-2.67	11611.060	14.00	6.26	0.10
10780.694	26.00	3.24	-3.29	11630.916	27.00	3.41	-0.68
10782.045	13.00	4.09	-1.76	11638.260	26.00	2.18	-2.21
10784.562	14.00	5.96	-0.84	11640.941	14.00	6.27	-0.43
10796.106	14.00	6.18	-1.27	11681.594	26.00	3.55	-3.62
10801.360	24.00	3.01	-1.56	11700.239	14.00	6.27	-0.53
10816.910	24.00	3.01	-1.89	11759.570	20.00	4.53	-0.88
10821.176	16.00	0.00	-8.61	11767.481	20.00	4.53	-0.54
10821.660	24.00	3.01	-1.52	11769.639	19.00	1.62	-0.45
10829.267	20.00	4.44	-1.22	11772.838	19.00	1.62	0.51
10833.382	20.00	4.88	-0.24	11780.542	22.00	1.44	-2.17
10838.970	20.00	4.88	0.24	11793.043	20.00	4.53	-0.26
10843.858	14.00	5.86	-0.11	11797.186	22.00	1.43	-2.28
10861.582	20.00	4.88	-0.34	11863.920	14.00	5.98	-1.46
10862.652	26.01	5.59	-2.20	11882.844	26.00	2.20	-1.67
10863.518	26.00	4.73	-0.90	11884.083	26.00	2.22	-2.08
10868.789	14.00	6.19	0.21	11892.877	22.00	1.43	-1.73
10872.973	13.00	4.09	-1.40	11900.055	14.00	5.96	-1.86
10879.868	20.00	4.88	-0.36	11927.838	28.00	4.27	-2.10
10881.758	26.00	2.85	-3.60	11949.547	22.00	1.44	-1.57
10882.809	14.00	5.98	-0.81	11955.955	20.00	4.13	-0.85
10884.262	26.00	3.93	-1.93	11973.046	26.00	2.18	-1.48
10885.333	14.00	6.18	0.22	11973.847	22.00	1.46	-1.39
10891.307	28.00	4.17	-1.25	12000.970	24.00	3.43	-2.07
10891.736	13.00	4.09	-1.03	12039.822	12.00	5.75	-1.53
10896.299	26.00	3.07	-2.69	12053.082	26.00	4.56	-1.54
10905.710	24.00	3.44	-0.56	12081.972	14.00	6.26	-0.52
10953.320	12.00	5.93	-0.86	12102.432	14.00	6.62	-0.69
10982.058	14.00	6.19	0.10	12105.841	20.00	4.55	-0.30
11015.530	24.00	3.45	-0.43	12110.659	14.00	6.62	-0.14
11026.788	26.00	3.94	-2.81	12119.494	26.00	4.59	-1.64
11054.253	30.00	5.80	-0.30	12167.243	22.00	3.35	-0.68
11119.795	26.00	2.85	-2.20	12178.339	14.00	6.27	-1.10
11374.078	26.00	2.18	-3.23	12189.241	14.00	6.62	-1.00
11379.330	24.00	3.32	-1.36	12213.336	26.00	4.64	-1.84
11388.538	26.00	5.62	-0.71	12216.579	28.00	5.28	-0.51
11390.750	24.00	3.32	-0.42	12227.112	26.00	4.61	-1.37
11398.060	24.00	3.32	-0.65	12239.915	22.00	2.15	-2.32
11402.734	26.00	6.26	0.24	12249.403	23.00	2.36	-1.00
11409.913	26.00	5.64	-0.84	12255.699	22.00	3.92	0.16

Continued.

| λ_{air} | code | χ | log gf | λ_{air} | code | χ | log gf |
Å		eV		Å		eV	
12311.480	11.00	3.75	-1.01	13104.517	23.00	1.95	-1.24
12340.481	26.00	2.28	-5.10	13134.942	20.00	4.45	0.09
12342.916	26.00	4.64	-1.46	13147.920	26.00	5.39	-0.81
12390.154	14.00	5.08	-1.77	13152.743	14.00	4.92	-2.50
12395.832	14.00	4.95	-1.64	13154.531	14.00	6.62	-1.00
12417.937	12.00	5.93	-1.66	13176.888	14.00	5.86	-0.20
12423.029	12.00	5.93	-1.19	13184.969	23.00	1.96	-1.90
12432.273	19.00	1.61	-0.44	13201.150	24.00	2.71	-1.83
12433.452	12.00	5.93	-0.97	13217.020	24.00	2.71	-2.30
12439.963	14.00	5.08	-2.73	13281.490	25.00	2.92	-1.35
12522.134	19.00	1.62	-0.14	13305.697	22.00	2.24	-1.86
12532.840	24.00	2.71	-1.88	13317.984	20.00	4.62	-0.48
12583.924	14.00	6.62	-0.46	13325.626	14.00	6.10	-0.16
12600.277	22.00	1.44	-2.32	13352.173	26.00	5.31	-0.52
12615.928	26.00	4.64	-1.52	13384.466	26.00	3.02	-4.12
12627.674	14.00	6.62	-0.81	13392.102	26.00	5.35	-0.12
12638.703	26.00	4.56	-0.78	13415.640	25.00	2.92	-1.73
12648.741	26.00	4.61	-1.14	14872.028	28.00	5.28	0.42
12651.030	24.00	3.84	-1.72	14897.406	26.00	6.42	0.31
12671.096	22.00	1.43	-2.36	14898.691	12.00	6.72	-1.64
12683.733	12.00	6.59	-1.50	14978.730	24.00	3.38	-1.81
12720.155	27.00	3.53	-1.17	14988.778	26.00	6.17	0.19
12738.383	22.00	2.17	-1.28	15013.771	26.00	6.22	0.09
12744.905	22.00	2.49	-1.28	15017.700	26.00	6.22	0.06
12807.152	26.00	3.64	-2.45	15032.251	28.00	5.28	-0.86
12808.243	26.00	4.99	-1.36	15136.124	26.00	5.83	-0.13
12811.478	22.00	2.16	-1.39	15160.503	26.00	6.34	-0.25
12816.045	20.00	3.91	-0.77	15163.067	19.00	2.67	0.69
12821.672	22.00	1.46	-1.19	15168.376	19.00	2.67	0.48
12823.867	20.00	3.91	-1.00	15176.713	26.00	5.92	-0.50
12824.859	26.00	3.02	-3.83	15194.490	26.00	2.22	-4.82
12827.059	20.00	3.91	-1.48	15207.526	26.00	5.39	0.32
12831.445	22.00	1.43	-1.49	15217.686	25.00	4.89	0.52
12847.034	22.00	1.44	-1.33	15224.729	26.00	5.96	-0.32
12879.766	26.00	2.28	-3.46	15239.712	26.00	6.42	-0.03
12885.290	20.00	4.43	-1.16	15243.588	14.00	6.73	-0.87
12901.212	23.00	1.96	-1.05	15262.415	25.00	4.89	0.39
12909.070	20.00	4.43	-0.22	15277.610	58.01	0.61	-1.94
12910.090	24.00	2.71	-1.78	15293.135	26.00	6.31	0.14
12919.899	22.00	2.15	-1.56	15301.557	26.00	5.92	-0.69
12921.810	24.00	2.71	-2.74	15315.585	22.00	2.34	-2.08
12934.666	26.00	5.39	-0.95	15343.788	26.00	5.65	-0.58
13011.897	22.00	1.44	-2.27	15381.960	26.00	5.98	-0.46
13029.524	14.00	6.08	-0.92	15469.816	16.00	8.05	-0.05
13030.921	14.00	6.08	-0.67	15478.482	16.00	8.05	0.18
13048.181	28.00	4.54	-1.01	15550.436	26.00	6.32	-0.10
13053.627	30.00	6.65	0.34	15588.259	26.00	6.37	0.42
13077.265	22.00	1.46	-2.22	15605.684	28.00	5.31	0.02
13098.876	26.00	5.01	-1.29	15621.654	26.00	5.54	0.59
13102.057	14.00	6.08	-0.31	15632.632	28.00	5.31	0.12

Continued.

λ_{air} Å	code	χ eV	log gf	λ_{air} Å	code	χ eV	log gf
15645.016	26.00	6.31	-0.39	16330.532	22.00	3.11	-0.89
15648.510	26.00	5.43	-0.60	16331.524	26.00	5.98	-0.39
15662.013	26.00	5.83	0.37	16363.103	28.00	5.28	0.59
15671.004	26.00	6.33	-0.22	16376.480	58.01	0.56	-1.79
15691.853	26.00	6.25	0.65	16388.850	11.00	3.75	-1.03
15753.606	28.00	5.47	-0.60	16434.926	14.00	5.96	-1.19
15761.313	26.00	6.25	0.14	16436.621	26.00	5.92	0.01
15769.423	26.00	5.54	0.70	16486.666	26.00	5.83	0.78
15770.617	26.00	6.30	0.46	16524.467	26.00	6.34	0.69
15784.786	58.01	0.32	-1.54	16551.994	26.00	6.41	0.34
15818.142	26.00	5.59	0.59	16589.439	28.00	5.47	-0.34
15821.712	26.00	5.64	-0.79	16635.160	22.00	2.34	-1.58
15822.816	26.00	5.64	0.19	16673.705	28.00	6.03	0.39
15827.213	14.00	7.09	-0.65	16679.160	26.00	5.92	-0.80
15833.602	14.00	6.22	-0.19	16693.072	26.00	6.42	-0.14
15860.210	24.00	4.70	0.02	16718.957	13.00	4.09	0.15
15891.160	26.00	6.31	-0.02	16721.463	26.00	6.38	-0.58
15895.225	26.00	6.26	0.48	16722.510	58.01	0.56	-1.65
15911.302	26.00	5.87	0.10	16750.564	13.00	4.09	0.41
15934.017	26.00	6.31	-0.29	16753.064	26.00	6.38	0.41
15958.390	58.01	0.47	-1.71	16757.643	27.00	3.41	-0.92
16006.540	29.00	5.35	0.26	16763.359	13.00	4.09	-0.55
16008.075	26.00	6.27	0.27	16775.250	27.00	5.55	0.49
16009.610	26.00	5.43	-0.47	16815.473	28.00	5.31	-0.42
16013.780	28.00	5.31	-0.53	16818.744	28.00	6.04	0.47
16040.654	26.00	5.87	0.32	16833.053	26.00	5.96	-0.89
16053.628	60.01	0.75	-2.20	16927.611	26.00	6.43	-0.16
16087.162	26.00	6.28	-0.71	16996.266	28.00	5.31	0.46
16102.408	26.00	5.87	0.55	17001.025	28.00	5.49	0.38
16115.966	26.00	6.39	0.43	17011.096	26.00	5.95	0.10
16125.899	26.00	6.35	0.86	17161.104	26.00	6.02	-0.07
16129.015	14.00	7.14	-0.66	17200.312	26.00	6.36	-0.64
16136.096	28.00	5.49	-0.00	17234.463	6.00	9.70	0.29
16136.823	20.00	4.53	-0.36	17277.479	26.00	6.32	-0.52
16150.762	20.00	4.53	-0.03	17282.291	26.00	6.43	0.10
16155.236	20.00	4.53	-0.50	17302.305	26.00	6.07	0.12
16156.557	26.00	5.96	-0.29	17376.576	22.00	4.49	0.75
16157.364	20.00	4.55	0.25	17399.387	28.00	6.07	0.06
16163.691	14.00	5.95	-0.86	17433.635	26.00	6.41	0.03
16165.029	26.00	6.32	0.99	17448.535	6.00	9.00	0.01
16171.930	26.00	6.38	-0.45	17469.920	26.00	6.41	-0.56
16177.991	26.00	6.38	-0.40	17480.645	26.00	6.64	0.32
16180.900	26.00	6.28	0.29	17524.297	26.00	6.69	0.23
16198.502	26.00	5.41	-0.44	17581.900	26.00	6.38	-0.08
16246.460	26.00	6.28	0.05	17640.186	26.00	5.11	-1.96
16292.840	26.00	5.92	-0.16	17672.039	6.00	7.95	-1.97
16310.501	28.00	5.28	0.22	17683.916	26.00	6.34	0.21
16316.320	26.00	6.28	1.07	17689.477	26.00	6.34	-0.14
16324.451	26.00	5.39	-0.56	17695.936	26.00	5.95	-0.52
16327.320	58.01	0.56	-2.40	17706.613	26.00	6.58	0.60

Continued.

λ_{air} Å	code	χ eV	log gf	λ_{air} Å	code	χ eV	log gf
17712.598	26.00	6.74	-0.14	21813.977	26.00	5.85	-1.39
17728.102	26.00	6.58	0.43	21832.980	26.00	6.78	-0.00
17749.615	12.00	6.73	-1.50	21837.953	14.00	7.07	-0.89
17755.158	26.00	6.34	-0.68	21851.381	26.00	3.64	-3.61
17768.910	6.00	9.71	0.42	21874.139	14.00	6.72	-0.60
17771.123	26.00	5.95	0.18	21879.324	14.00	6.72	0.41
17793.158	6.00	9.71	-0.04	21882.986	26.00	6.87	0.14
17861.725	26.00	6.59	-0.55	21924.830	14.00	7.06	-1.16
17930.154	26.00	5.87	0.04	22062.711	14.00	6.73	0.54
17951.836	28.00	6.09	0.32	22072.551	14.00	6.73	-0.94
17956.031	26.00	6.74	0.47	22310.617	22.00	1.73	-2.07
17969.510	14.00	7.11	-1.17	22380.797	26.00	5.03	-0.46
17986.533	28.00	6.09	0.99	22385.102	26.00	5.32	-1.35
17988.479	28.00	6.10	0.21	22392.879	26.00	5.10	-1.25
21139.760	14.00	7.29	-0.44	22394.670	21.00	1.43	-1.20
21163.756	13.00	4.09	-0.01	22443.926	22.00	1.74	-2.36
21167.928	28.00	5.28	-1.03	22473.264	26.00	6.12	0.44
21178.154	26.00	3.02	-4.01	22507.557	16.00	7.87	-0.48
21213.729	12.00	6.73	-1.56	22519.066	16.00	7.87	-0.25
21216.309	26.00	6.46	-0.60	22537.533	14.00	6.62	-0.23
21238.467	26.00	4.96	-1.42	22575.395	16.00	7.87	-0.73
21284.348	26.00	3.07	-4.26	22619.838	26.00	4.99	-0.36
21458.863	12.00	6.52	-1.32	22626.723	20.00	4.68	-0.22
21754.434	14.00	7.30	-0.67	22644.057	16.00	7.87	-0.34
21779.660	14.00	6.72	0.42	22707.738	16.00	7.87	0.44
21812.055	21.00	1.43	-1.96	23141.613	14.00	6.80	-0.97
21813.977	26.00	5.85	-1.39	23308.477	26.00	4.08	-2.31

Table A.3: NIR molecular lines used for the abundance analysis of Arcturus. Wavelengths are in air.

λ_{air} Å	code	χ eV	log gf	λ_{air} Å	code	χ eV	log gf
9682.068	607.00	0.66	-1.00	11550.312	607.00	0.40	-1.34
9706.730	607.00	0.52	-1.38	11575.142	607.00	0.42	-1.33
9749.751	607.00	0.57	-1.36	11578.002	607.00	0.62	-0.94
9757.623	607.00	0.77	-0.98	11580.309	607.00	0.88	-1.15
9759.349	607.00	0.57	-1.35	11603.597	607.00	0.75	-2.33
9771.955	607.00	0.59	-1.35	11606.542	607.00	0.90	-1.14
9779.767	607.00	0.79	-0.97	11615.760	607.00	0.64	-0.92
9802.389	607.00	0.82	-0.96	11617.543	607.00	0.90	-1.13
9804.015	607.00	0.62	-1.34	11626.590	607.00	0.46	-1.31
9810.249	607.00	0.82	-0.96	11629.788	607.00	0.66	-0.92
9825.487	607.00	0.85	-0.96	11633.388	607.00	0.93	-1.13
9841.420	607.00	0.66	-1.32	11644.315	607.00	0.93	-1.12
9849.080	607.00	0.88	-0.95	11668.477	607.00	0.69	-0.90
9874.644	607.00	0.69	-1.31	11671.710	607.00	0.96	-1.12
9940.901	607.00	0.77	-1.29	11680.463	607.00	0.50	-1.29
9948.443	607.00	0.99	-0.92	11683.988	607.00	0.71	-0.90
9955.930	607.00	0.99	-0.91	11694.121	607.00	0.52	-1.29
9974.568	607.00	1.02	-0.91	11695.756	607.00	0.71	-0.89
9982.003	607.00	1.02	-0.91	11708.326	607.00	0.52	-1.28
10035.743	607.00	1.08	-0.89	11712.011	607.00	1.38	-3.03
10977.173	607.00	0.08	-1.67	11717.674	607.00	1.02	-1.11
10981.077	607.00	0.09	-1.64	11722.780	607.00	0.55	-1.28
10985.461	607.00	0.10	-1.62	11723.660	607.00	0.74	-0.89
10990.322	607.00	0.11	-1.60	11736.815	607.00	0.55	-1.27
11001.474	607.00	0.13	-1.56	11740.659	607.00	0.77	-0.89
11007.763	607.00	0.14	-1.54	11781.371	607.00	0.79	-0.87
11033.194	607.00	0.04	-2.00	11781.982	607.00	0.59	-1.26
11065.131	607.00	0.23	-1.43	11812.540	607.00	0.62	-1.25
11066.964	607.00	0.06	-1.87	11826.118	607.00	0.62	-1.24
11070.714	607.00	0.26	-2.40	11843.748	607.00	0.64	-1.24
11074.544	607.00	0.25	-1.42	11857.190	607.00	0.64	-1.23
11075.243	607.00	0.25	-1.42	11861.671	607.00	0.88	-0.85
11085.839	607.00	0.26	-1.40	11872.811	607.00	0.88	-0.85
11096.920	607.00	0.28	-1.39	11888.929	607.00	0.66	-1.23
11102.186	607.00	0.15	-1.27	11904.624	607.00	0.90	-0.84
11105.320	607.00	0.31	-1.38	11921.341	607.00	0.69	-1.22
11362.293	607.00	0.62	-1.21	11941.357	607.00	0.71	-1.21
11367.626	607.00	0.40	-1.02	11959.411	607.00	0.96	-0.83
11375.103	607.00	0.28	-1.44	11975.253	607.00	0.74	-1.21
11392.648	607.00	0.28	-1.43	11988.224	607.00	0.74	-1.20
11396.289	607.00	0.29	-1.43	11993.370	607.00	0.99	-0.83
11407.670	607.00	0.44	-1.00	12004.190	607.00	0.99	-0.82
11414.961	607.00	0.46	-1.00	12022.716	607.00	0.78	-3.22
11428.516	607.00	0.46	-0.99	12038.785	607.00	1.02	-0.81
11456.811	607.00	0.33	-1.39	12045.139	607.00	0.79	-1.19
11458.082	607.00	0.74	-1.18	12057.915	607.00	0.79	-1.18
11486.445	607.00	0.36	-1.38	12081.151	607.00	0.82	-1.18
11526.069	607.00	0.38	-1.36	12099.521	607.00	1.08	-0.81
11528.571	607.00	0.57	-0.95	12117.893	607.00	0.85	-1.17
11534.864	607.00	0.40	-1.35	12130.491	607.00	0.85	-1.17

Continued.

λ_{air} Å	code	χ eV	log gf	λ_{air} Å	code	χ eV	log gf
12136.365	607.00	1.11	-0.80	15481.868	607.00	0.86	-1.50
12146.933	607.00	1.11	-0.79	15530.776	607.00	0.89	-1.50
12167.887	607.00	0.88	-1.16	15568.780	108.00	0.30	-5.27
12184.472	607.00	1.15	-0.79	15600.740	608.00	0.11	-7.80
12193.584	607.00	0.90	-1.16	15612.500	608.00	0.08	-7.88
12212.306	607.00	1.18	-0.79	15651.896	108.00	0.53	-5.13
12251.432	607.00	1.21	-0.78	15667.550	608.00	0.86	-7.13
12272.315	607.00	0.96	-1.14	15684.088	607.00	0.96	-1.47
12284.636	607.00	0.96	-1.14	15719.696	108.00	0.36	-5.25
12301.714	607.00	1.24	-0.77	15737.445	607.00	0.99	-1.46
12373.552	607.00	1.31	-0.76	15755.522	108.00	0.57	-5.11
12383.853	607.00	1.31	-0.76	16052.765	108.00	0.64	-4.91
12415.883	607.00	1.34	-0.76	16162.191	607.00	1.49	-1.04
14855.675	607.00	0.99	-1.44	16211.760	608.00	1.31	-5.93
14868.927	607.00	0.56	-1.67	16222.600	608.00	0.86	-6.52
14887.588	607.00	0.88	-1.64	16314.410	608.00	0.84	-6.61
14954.435	607.00	0.63	-1.95	16368.135	108.00	0.73	-4.80
14958.275	607.00	0.72	-1.48	16475.890	608.00	1.77	-5.54
15005.117	607.00	0.82	-1.21	16526.254	108.00	0.79	-4.78
15127.914	607.00	0.69	-1.58	16610.130	608.00	0.89	-6.64
15130.921	108.00	0.17	-5.50	16633.730	608.00	1.40	-5.91
15181.277	607.00	1.24	-1.38	16637.410	608.00	1.39	-5.94
15266.168	108.00	0.21	-5.43	16670.580	608.00	1.92	-5.37
15281.052	108.00	0.21	-5.38	16771.620	608.00	0.91	-6.76
15298.487	607.00	0.88	-1.87	16904.279	108.00	0.90	-4.66
15308.893	607.00	1.01	-1.15	16949.380	608.00	1.22	-6.26
15318.740	607.00	0.94	-1.31	17104.721	108.00	0.96	-4.61
15337.959	607.00	0.90	-1.83	17193.950	608.00	1.48	-6.02
15341.508	607.00	0.80	-1.53	17531.820	108.00	1.10	-4.56
15409.172	108.00	0.26	-5.37	21161.020	607.00	0.96	-1.87
15432.811	607.00	0.84	-1.70	21291.668	607.00	1.00	-1.82
15447.095	607.00	1.09	-1.12	21352.234	607.00	1.00	-1.81
15466.235	607.00	1.09	-1.12	23358.329	109.00	0.23	-3.96

Table A.4: ^{12}CO and ^{13}CO bandheads used for the abundance analysis of Arcturus. Wavelengths are in air.

v'-v"	code	λ_{air} Å
3-0	608.12	15577-15580
4-1	608.12	15774-15776
5-2	608.12	15976-15980
6-3	608.12	16183-16186
7-4	608.12	16395-16400
5-2	608.13	16529-16532
8-5	608.12	16611-16615
9-6	608.12	16834-16837
6-3	608.13	16956-16960
10-7	608.12	17061-17065
4-2	608.13	23440-23447
6-4	608.13	23731-23738
7-5	608.13	24028-24034

Optical and NIR linelists for red supergiant stars

Table B.1: Optical atomic lines used for the abundance analysis of Arcturus. Wavelengths are in air.

λ_{air}	code	χ eV	log gf	λ_{air}	code	χ eV	log gf
4805.870	40.00	4.58	-6.04	5526.790	21.01	1.77	0.02
4815.040	40.00	4.65	-4.87	5530.775	27.00	1.71	-2.06
4828.040	40.00	5.09	-5.93	5548.450	60.01	0.55	-1.27
4914.380	60.01	0.38	-0.70	5552.224	21.01	1.46	-2.09
4915.229	22.00	1.89	-0.91	5593.735	28.00	3.90	-0.84
4922.265	24.00	3.10	0.38	5604.936	23.00	1.04	-1.26
4926.148	22.00	0.82	-2.09	5611.356	26.00	3.64	-2.99
4935.831	28.00	3.94	-0.35	5614.773	28.00	4.15	-0.57
4936.335	24.00	3.11	-0.25	5626.018	23.00	1.04	-1.26
4959.119	60.01	0.06	-0.80	5627.630	23.00	1.08	-0.35
4961.387	60.01	0.63	-0.71	5630.131	39.00	1.36	0.21
5045.414	22.00	0.85	-1.84	5641.001	21.01	1.50	-1.13
5081.574	21.00	1.45	0.47	5647.234	27.00	2.28	-1.56
5217.389	26.00	3.21	-1.07	5652.317	26.00	4.26	-1.95
5239.813	21.01	1.46	-0.77	5653.864	26.00	4.39	-1.64
5241.458	24.00	2.71	-1.92	5657.440	23.00	1.06	-1.00
5249.580	60.01	0.98	0.20	5662.516	26.00	4.18	-0.57
5260.387	20.00	2.52	-1.72	5664.030	24.00	3.43	-0.71
5274.229	58.01	1.49	-2.66	5668.362	23.00	1.08	-1.01
5289.816	39.01	9.60	-1.26	5669.042	21.01	1.50	-1.20
5293.160	60.01	0.82	0.10	5670.848	23.00	1.08	-0.43
5295.776	22.00	1.07	-1.59	5682.633	11.00	2.10	-0.71
5300.011	22.00	1.05	-2.30	5686.120	26.00	3.64	-2.92
5304.180	24.00	3.46	-0.67	5686.529	26.00	4.55	-0.45
5306.460	60.01	0.86	-0.97	5703.575	23.00	1.05	-0.21
5330.556	58.01	1.49	-2.66	5704.732	26.00	5.03	-1.43
5334.240	21.01	1.50	-2.20	5712.131	26.00	3.42	-1.99
5338.306	22.00	0.83	-2.73	5712.771	24.00	3.01	-1.04
5344.756	24.00	3.45	-0.99	5715.821	20.00	2.71	-3.23
5351.068	22.00	2.78	-0.07	5716.450	22.00	2.30	-0.72
5356.970	60.01	1.26	-0.28	5717.307	21.00	1.44	-0.53
5357.199	21.01	1.51	-2.11	5719.815	24.00	3.01	-1.58
5359.200	27.00	4.15	0.24	5724.107	21.00	1.43	-0.66
5366.639	22.00	0.82	-2.59	5725.639	23.00	2.37	-0.17
5369.961	26.00	4.37	0.54	5727.655	23.00	1.05	-0.85
5375.355	21.00	1.97	-0.05	5731.249	23.00	1.06	-0.74
5376.600	22.00	0.00	-4.00	5732.296	26.00	4.99	-1.56
5377.607	25.00	3.84	-0.17	5737.062	23.00	1.06	-0.74
5384.630	22.00	0.83	-2.90	5741.847	26.00	4.26	-1.85
5385.888	60.01	0.74	-0.82	5748.351	28.00	1.68	-3.24
5399.475	25.00	3.85	-0.34	5752.031	26.00	4.55	-1.17
5404.991	24.00	3.38	-0.95	5775.080	26.00	4.22	-1.30
5408.130	27.00	2.28	-2.23	5778.453	26.00	2.59	-3.43
5410.909	26.00	4.47	0.40	5793.915	26.00	4.22	-1.70
5425.249	26.01	3.20	-3.16	5853.148	26.00	1.48	-5.28
5431.520	60.01	1.12	-0.47	5856.087	26.00	4.29	-1.33
5462.959	26.00	4.47	-0.13	5866.451	22.00	1.07	-0.92
5471.192	22.00	1.44	-1.42	5868.107	66.01	0.00	-2.73
5476.289	26.00	4.14	-0.92	5879.800	40.00	0.15	-1.67
5523.297	27.00	2.33	-1.64	5883.816	26.00	3.96	-1.36

Continued.

λ_{air}	code	χ eV	log gf	λ_{air}	code	χ eV	log gf
5885.620	40.00	5.54	-9.13	6312.236	22.00	1.46	-1.55
5918.536	22.00	1.07	-1.77	6318.717	12.00	5.11	-2.10
5925.130	40.00	5.37	-9.86	6319.237	12.00	5.11	-2.32
5930.180	26.00	4.65	-0.23	6325.164	22.00	0.02	-3.76
5937.809	22.00	1.07	-2.07	6327.599	28.00	1.68	-3.17
5944.660	22.00	0.00	-3.85	6336.823	26.00	3.69	-0.86
5948.541	14.00	5.08	-1.23	6353.835	26.00	0.91	-6.17
5976.438	26.00	4.18	-2.52	6359.888	22.00	0.05	-4.07
5976.776	26.00	3.94	-1.24	6393.600	26.00	2.43	-1.43
6003.011	26.00	3.88	-1.12	6408.017	26.00	3.69	-1.02
6005.026	27.00	1.71	-3.32	6411.647	26.00	3.65	-0.59
6007.310	28.00	1.68	-3.40	6419.088	22.00	2.17	-1.53
6007.959	26.00	4.65	-0.60	6432.676	26.01	2.89	-3.52
6024.057	26.00	4.55	-0.12	6436.405	26.00	4.19	-2.46
6027.050	26.00	4.08	-1.09	6445.740	40.00	0.99	-0.83
6039.726	23.00	1.06	-0.65	6455.598	20.00	2.52	-1.34
6043.373	58.01	1.49	-2.66	6471.662	20.00	2.53	-0.69
6058.142	23.00	1.04	-1.40	6482.798	28.00	1.94	-2.63
6064.626	22.00	1.05	-1.80	6543.504	23.00	1.19	-1.71
6078.491	26.00	4.80	-0.32	6554.223	22.00	1.44	-1.15
6081.442	23.00	1.05	-0.61	6560.287	26.00	4.91	-1.46
6111.650	23.00	1.04	-0.74	6581.209	26.00	1.48	-4.68
6116.990	27.00	1.79	-2.49	6604.601	21.01	1.36	-1.31
6119.527	23.00	1.06	-0.36	6632.439	27.00	2.28	-2.00
6120.246	26.00	0.91	-5.95	6646.930	26.00	2.61	-3.99
6126.216	22.00	1.07	-1.21	6648.079	26.00	1.01	-5.43
6127.440	40.00	4.73	-3.09	6696.023	13.00	3.14	-1.35
6134.550	40.00	5.39	-3.08	6698.673	13.00	3.14	-1.65
6140.460	40.00	5.07	-5.68	6699.141	26.00	4.59	-2.10
6143.200	40.00	5.45	-6.97	6713.742	26.00	4.80	-1.60
6145.016	14.00	5.62	-1.31	6725.355	26.00	4.10	-2.30
6154.226	11.00	2.10	-1.55	6726.666	26.00	4.61	-1.09
6160.747	11.00	2.10	-1.25	6733.150	26.00	4.64	-1.58
6175.367	28.00	4.09	-0.53	6739.520	26.00	1.56	-4.79
6183.558	26.00	5.03	-1.18	6745.100	26.00	4.58	-2.16
6185.693	26.00	5.65	-0.62	6746.953	26.00	2.61	-4.35
6187.397	26.00	2.83	-4.16	6784.256	13.00	4.02	-1.28
6226.734	26.00	3.88	-2.22	6793.258	26.00	4.08	-2.33
6240.646	26.00	2.22	-3.23	6798.479	20.00	2.71	-2.54
6246.317	26.00	3.60	-0.73	6806.842	26.00	2.73	-3.21
6247.557	26.01	3.89	-2.31	6810.262	26.00	4.61	-0.99
6270.223	26.00	2.86	-2.46	6828.591	26.00	4.64	-0.92
6300.304	8.00	0.00	-9.78	6839.830	26.00	2.56	-3.45
6301.500	26.00	3.65	-0.72	6842.685	26.00	4.64	-1.32

Table B.2: NIR atomic lines used for the abundance analysis of Arcturus. Wavelengths are in air.

λ_{air}	code	χ eV	log gf	λ_{air}	code	χ eV	log gf
9667.285	24.00	2.54	-2.51	10677.047	22.00	0.84	-2.52
9734.563	24.00	2.54	-1.95	10694.251	14.00	5.96	0.05
9811.504	26.00	5.01	-1.36	10725.185	26.00	3.64	-2.76
9879.583	22.00	1.87	-2.40	10726.391	22.00	0.81	-2.06
9889.035	26.00	5.03	-0.45	10732.864	22.00	0.83	-2.52
9946.320	24.00	3.56	-1.62	10746.449	11.00	3.19	-1.29
9981.276	22.00	3.11	-0.99	10753.004	26.00	3.96	-1.84
10003.088	22.00	2.16	-1.21	10770.134	14.00	6.62	-1.25
10005.664	22.00	1.07	-3.65	10774.866	22.00	0.82	-2.67
10025.039	21.00	1.86	-1.18	10780.694	26.00	3.24	-3.29
10034.491	22.00	1.46	-1.77	10784.562	14.00	5.96	-0.84
10046.414	27.00	2.72	-2.08	10796.106	14.00	6.18	-1.27
10059.904	22.00	1.43	-2.08	10801.360	24.00	3.01	-1.56
10066.512	22.00	2.16	-1.85	10816.910	24.00	3.01	-1.89
10075.123	22.00	1.07	-3.93	10818.274	26.00	3.96	-1.95
10080.350	24.00	3.56	-1.27	10821.176	16.00	0.00	-8.61
10081.393	26.00	2.42	-4.54	10838.970	20.00	4.88	0.24
10083.180	24.00	3.56	-1.72	10847.633	22.00	0.83	-3.92
10155.162	26.00	2.18	-4.23	10863.518	26.00	4.73	-0.90
10167.468	26.00	2.20	-4.12	10882.809	14.00	5.98	-0.81
10189.146	22.00	1.46	-3.10	10891.736	13.00	4.09	-1.10
10216.313	26.00	4.73	-0.06	11026.788	26.00	3.94	-2.81
10218.408	26.00	3.07	-2.76	11054.253	30.00	5.80	-0.30
10265.217	26.00	2.22	-4.54	11379.330	24.00	3.32	-1.36
10340.885	26.00	2.20	-3.58	11422.319	26.00	2.20	-2.70
10343.819	20.00	2.93	-0.30	11473.020	24.00	3.32	-0.52
10353.804	26.00	5.39	-0.82	11484.630	24.00	3.32	-0.23
10382.306	27.00	2.87	-2.16	11588.684	28.00	4.24	-1.21
10395.794	26.00	2.18	-3.39	11627.527	14.00	5.96	-1.93
10414.913	14.00	6.62	-1.14	11630.916	27.00	3.41	-0.68
10423.027	26.00	2.69	-3.62	11667.226	22.00	2.34	-2.19
10423.743	26.00	3.07	-2.92	11767.481	20.00	4.53	-0.54
10455.470	16.00	6.86	0.25	11797.186	22.00	1.43	-2.28
10456.790	16.00	6.86	-0.45	11863.920	14.00	5.98	-1.46
10486.250	24.00	3.01	-0.95	11892.877	22.00	1.43	-1.73
10510.010	24.00	3.01	-1.53	11900.055	14.00	5.96	-1.86
10517.511	14.00	6.73	-1.04	11955.955	20.00	4.13	-0.85
10523.390	66.01	1.95	-0.45	12000.970	24.00	3.43	-2.07
10530.514	28.00	4.11	-1.19	12039.822	12.00	5.75	-1.53
10532.234	26.00	3.93	-1.48	12081.972	14.00	6.26	-0.52
10551.757	22.00	1.89	-2.42	12105.841	20.00	4.55	-0.30
10552.965	22.00	2.25	-1.57	12178.339	14.00	6.27	-1.10
10555.649	26.00	5.45	-1.11	12189.241	14.00	6.62	-1.00
10565.952	22.00	2.24	-1.78	12190.098	26.00	3.64	-2.33
10577.139	26.00	3.30	-3.14	12216.579	28.00	5.28	-0.51
10582.160	14.00	6.22	-1.17	12340.481	26.00	2.28	-5.10
10607.718	22.00	0.85	-2.70	12432.273	19.00	1.61	-0.44
10616.721	26.00	3.27	-3.13	12433.452	12.00	5.93	-0.97
10647.640	24.00	3.01	-1.58	12532.840	24.00	2.71	-1.88
10672.140	24.00	3.01	-1.35	12583.924	14.00	6.62	-0.46

Continued.

λ_{air}	code	χ eV	log gf	λ_{air}	code	χ eV	log gf
12638.703	26.00	4.56	-0.78	15764.323	26.00	6.30	-0.06
12720.155	27.00	3.53	-1.17	15784.786	58.01	0.32	-1.54
12738.383	22.00	2.17	-1.28	16006.540	29.00	5.35	0.26
12743.264	28.00	5.28	-0.45	16155.236	20.00	4.53	-0.50
12807.152	26.00	3.64	-2.45	16163.691	14.00	5.95	-0.86
12808.243	26.00	4.99	-1.36	16171.930	26.00	6.38	-0.45
12811.478	22.00	2.16	-1.39	16330.532	22.00	3.11	-0.89
12816.045	20.00	3.91	-0.77	16388.729	11.00	6.04	-0.25
12823.867	20.00	3.91	-1.00	16446.551	26.00	6.29	-0.75
12824.859	26.00	3.02	-3.83	16635.160	22.00	2.34	-1.58
12827.059	20.00	3.91	-1.48	16718.957	13.00	4.09	0.15
12847.034	22.00	1.44	-1.33	16750.564	13.00	4.09	0.41
12879.766	26.00	2.28	-3.46	16757.643	27.00	3.41	-0.92
12901.212	23.00	1.96	-1.05	16763.359	13.00	4.09	-0.55
12909.070	20.00	4.43	-0.22	16775.250	27.00	5.55	0.49
12910.090	24.00	2.71	-1.78	17001.025	28.00	5.49	0.38
12919.899	22.00	2.15	-1.56	17161.104	26.00	6.02	-0.07
12921.810	24.00	2.71	-2.74	17257.564	26.00	6.32	-0.38
12937.020	24.00	2.71	-1.90	17376.576	22.00	4.49	0.75
13006.684	26.00	2.99	-3.74	17499.980	26.00	5.96	-0.76
13030.921	14.00	6.08	-0.67	17689.477	26.00	6.34	-0.14
13033.554	20.00	4.44	-0.06	17717.133	26.00	6.34	-0.36
13053.627	30.00	6.65	0.34	17771.123	26.00	5.95	0.18
13098.876	26.00	5.01	-1.29	17932.600	26.00	6.46	0.17
13102.057	14.00	6.08	-0.31	17982.309	26.00	6.59	0.04
13104.517	23.00	1.95	-1.24	17993.316	26.00	6.59	0.43
13134.942	20.00	4.45	0.09	21163.756	13.00	4.09	-0.01
13147.920	26.00	5.39	-0.81	21167.928	28.00	5.28	-1.03
13152.743	14.00	4.92	-2.50	21178.154	26.00	3.02	-4.01
13184.969	23.00	1.96	-1.90	21238.467	26.00	4.96	-1.42
13201.150	24.00	2.71	-1.83	21284.348	26.00	3.07	-4.26
13260.728	26.00	5.01	-0.64	21452.373	11.00	4.28	-0.53
13309.045	14.00	6.10	-0.51	21458.863	12.00	6.52	-1.32
13352.173	26.00	5.31	-0.52	21730.506	21.00	1.44	-1.96
13384.466	26.00	3.02	-4.12	21735.457	26.00	6.18	-0.71
13392.102	26.00	5.35	-0.12	21779.660	14.00	6.72	0.42
13429.070	14.00	6.40	-1.54	21812.055	21.00	1.43	-1.96
14872.028	28.00	5.28	0.42	21837.953	14.00	7.07	-0.89
14917.060	25.00	5.70	0.38	21842.840	21.00	1.43	-2.70
14988.778	26.00	6.17	0.19	21851.381	26.00	3.64	-3.61
15194.490	26.00	2.22	-4.82	21874.139	14.00	6.72	-0.60
15217.686	25.00	4.89	0.52	22052.143	21.00	1.45	-0.84
15262.415	25.00	4.89	0.39	22062.711	14.00	6.73	0.54
15277.610	58.01	0.61	-1.94	22065.232	21.00	1.44	-1.06
15315.585	22.00	2.34	-2.08	22072.551	14.00	6.73	-0.94
15361.161	14.00	5.95	-2.08	22380.797	26.00	5.03	-0.46
15723.586	26.00	5.62	-0.14	22385.102	26.00	5.32	-1.35
15740.706	12.00	5.93	-0.21	22392.879	26.00	5.10	-1.25
15741.917	26.00	5.65	-0.10	22394.670	21.00	1.43	-1.20
15761.313	26.00	6.25	0.14	22443.926	22.00	1.74	-2.36

Continued.

λ_{air}	code	χ eV	log gf	λ_{air}	code	χ eV	log gf
22519.066	16.00	7.87	-0.25	22651.178	20.00	4.68	0.85
22537.533	14.00	6.62	-0.23	22653.578	20.00	4.68	-0.22
22543.836	39.00	1.39	-0.77	22665.758	14.00	6.62	-0.68
22624.963	20.00	4.68	0.69	22707.738	16.00	7.87	0.44
22626.723	20.00	4.68	-0.22	23141.613	14.00	6.80	-0.97

Table B.3: NIR molecular lines used for the abundance analysis of Arcturus. Wavelengths are in air.

λ_{air}	code	χ eV	log gf	λ_{air}	code	χ eV	log gf
9749.751	607.00	0.57	-1.36	12193.584	607.00	0.90	-1.16
9757.623	607.00	0.77	-0.98	12251.432	607.00	1.21	-0.78
9802.389	607.00	0.82	-0.96	12284.636	607.00	0.96	-1.14
9804.015	607.00	0.62	-1.34	12366.388	607.00	1.02	-1.12
9841.420	607.00	0.66	-1.32	12585.213	607.00	1.18	-1.09
9974.568	607.00	1.02	-0.91	12764.137	607.00	1.31	-1.07
10878.237	607.00	0.03	-2.60	12785.843	607.00	1.63	-0.71
10890.362	607.00	0.01	-2.62	12795.927	607.00	1.63	-0.71
11046.350	607.00	0.20	-1.46	12814.180	607.00	1.34	-1.07
11066.964	607.00	0.06	-1.87	12865.179	607.00	1.38	-1.06
11075.243	607.00	0.25	-1.42	12877.069	607.00	1.38	-1.06
11085.839	607.00	0.26	-1.40	12981.996	607.00	1.45	-1.04
11362.293	607.00	0.62	-1.21	15129.663	108.00	0.17	-5.50
11370.630	607.00	0.64	-1.22	15130.921	108.00	0.17	-5.50
11418.008	607.00	0.31	-1.41	15266.168	108.00	0.21	-5.43
11428.516	607.00	0.46	-0.99	15278.524	108.00	0.20	-5.38
11463.080	607.00	0.35	-1.39	15281.052	108.00	0.21	-5.38
11492.797	607.00	0.77	-1.17	15409.172	108.00	0.26	-5.37
11510.370	607.00	0.38	-1.36	15560.244	108.00	0.30	-5.31
11528.571	607.00	0.57	-0.95	15568.780	108.00	0.30	-5.27
11534.864	607.00	0.40	-1.35	15572.084	108.00	0.30	-5.27
11559.931	607.00	0.42	-1.34	15597.348	608.00	0.12	-7.94
11615.760	607.00	0.64	-0.92	15600.737	608.00	0.11	-7.97
11633.388	607.00	0.93	-1.13	15612.497	608.00	0.08	-8.05
11644.315	607.00	0.93	-1.12	15655.537	608.00	0.03	-8.34
11660.853	607.00	0.96	-1.12	15667.552	608.00	0.86	-7.25
11671.710	607.00	0.96	-1.12	15719.696	108.00	0.36	-5.25
11683.988	607.00	0.71	-0.90	15755.522	108.00	0.57	-5.11
11694.121	607.00	0.52	-1.29	15756.532	108.00	0.57	-5.11
11695.756	607.00	0.71	-0.89	15824.025	608.00	0.32	-7.50
11708.326	607.00	0.52	-1.28	15869.942	608.00	1.12	-6.62
11717.674	607.00	1.02	-1.11	15983.227	608.00	0.91	-6.50
11736.815	607.00	0.55	-1.27	15983.618	608.00	0.70	-6.75
11740.659	607.00	0.77	-0.89	15995.809	608.00	1.01	-6.42
11807.756	607.00	1.11	-1.09	16052.765	108.00	0.64	-4.91
11843.748	607.00	0.64	-1.24	16174.141	608.00	0.36	-7.63
11888.929	607.00	0.66	-1.23	16199.728	608.00	0.92	-6.51
11904.624	607.00	0.90	-0.84	16211.761	608.00	1.31	-6.07
11914.304	607.00	1.21	-1.07	16222.602	608.00	0.86	-6.67
11941.357	607.00	0.71	-1.21	16227.416	608.00	0.85	-6.70
11947.688	607.00	1.24	-1.06	16237.901	608.00	0.84	-6.77
11954.436	607.00	0.71	-1.21	16276.238	608.00	0.80	-7.03
11959.411	607.00	0.96	-0.83	16282.271	608.00	0.56	-7.35
11993.370	607.00	0.99	-0.83	16295.603	608.00	0.57	-7.32
12038.785	607.00	1.02	-0.81	16314.409	608.00	1.71	-5.84
12074.101	607.00	1.05	-0.81	16354.582	108.00	0.74	-4.84
12099.521	607.00	1.08	-0.81	16364.590	108.00	0.73	-4.80
12117.893	607.00	0.85	-1.17	16368.135	108.00	0.73	-4.80
12130.491	607.00	0.85	-1.17	16429.053	608.00	0.65	-7.14
12136.365	607.00	1.11	-0.80	16448.055	108.00	0.61	-5.08

Continued.

λ_{air}	code	χ eV	log gf	λ_{air}	code	χ eV	log gf
16462.549	608.00	1.72	-5.71	17146.822	608.00	1.81	-6.12
16469.061	608.00	1.74	-5.69	17148.080	608.00	2.47	-5.12
16475.889	608.00	1.77	-5.68	17213.340	608.00	1.49	-6.22
16488.121	608.00	1.06	-6.76	17214.467	608.00	1.61	-6.22
16500.574	608.00	0.53	-8.05	17239.723	108.00	1.14	-4.50
16526.254	108.00	0.79	-4.78	17264.895	608.00	1.46	-6.34
16538.586	108.00	0.78	-4.75	17273.574	608.00	1.54	-6.19
16610.133	608.00	0.88	-6.84	17308.439	108.00	1.03	-4.60
16662.205	108.00	0.68	-5.01	17322.248	108.00	1.03	-4.58
16771.625	608.00	0.91	-6.97	17335.590	608.00	2.09	-5.70
16793.756	608.00	0.93	-6.96	17367.959	608.00	1.69	-6.07
16823.691	608.00	1.03	-6.69	17473.326	608.00	5.95	-6.62
16848.703	608.00	1.67	-5.84	17531.820	108.00	1.10	-4.56
16904.279	108.00	0.90	-4.66	17585.619	108.00	1.02	-4.90
16949.377	608.00	1.22	-6.47	17590.162	108.00	1.01	-4.88
16972.361	608.00	1.35	-6.44	17598.971	108.00	1.01	-4.88
16984.863	608.00	2.44	-5.19	17632.443	608.00	1.77	-6.28
17050.076	108.00	1.10	-4.60	17679.334	108.00	1.41	-4.47
17083.104	608.00	1.15	-7.32	17686.682	608.00	1.91	-5.93
17096.391	108.00	0.96	-4.64	17818.473	108.00	1.31	-4.39
17104.721	108.00	0.96	-4.61	17830.695	108.00	1.30	-4.36
17146.822	608.00	1.81	-6.12	23358.329	109.00	0.23	-3.96

List of Figures

List of Tables

Bibliography

Alexeeva, S. A., & Mashonkina, L. I. 2015, MNRAS, 453, 1619, doi: 10.1093/mnras/stv1668

Alexeeva, S. A., Pakhomov, Y. V., & Mashonkina, L. I. 2014, Astronomy Letters, 40, 406, doi: 10.1134/S1063773714070019

Alvarez, R., & Plez, B. 1998, A&A, 330, 1109. https://arxiv.org/abs/astro-ph/9710157

Alves-Brito, A., Meléndez, J., Asplund, M., Ramírez, I., & Yong, D. 2010, A&A, 513, A35, doi: 10.1051/0004-6361/200913444

Asplund, M., Grevesse, N., Sauval, A. J., & Scott, P. 2009, ARA&A, 47, 481, doi: 10.1146/annurev.astro.46.060407.145222

Balachandran, S. C., Mallik, S. V., & Lambert, D. L. 2011, MNRAS, 410, 2526, doi: 10.1111/j.1365-2966.2010.17630.x

Ball, N. M., Brunner, R. J., Myers, A. D., & Tcheng, D. 2006, ApJ, 650, 497, doi: 10.1086/507440

Bensby, T., Feltzing, S., & Oey, M. S. 2014, A&A, 562, A71, doi: 10.1051/0004-6361/201322631

Bertelli, G., Nasi, E., Girardi, L., & Marigo, P. 2009, A&A, 508, 355, doi: 10.1051/0004-6361/200912093

Böhm, K. H. 1952, Z. Astrophys., 30, 117

Böker, T., Laine, S., van der Marel, R. P., et al. 2002, AJ, 123, 1389, doi: 10.1086/339025

Bressan, A., Marigo, P., Girardi, L., et al. 2012, MNRAS, 427, 127, doi: 10.1111/j.1365-2966.2012.21948.x

Cameron, A. G. W., & Fowler, W. A. 1971, ApJ, 164, 111, doi: 10.1086/150821

Carollo, C. M., Stiavelli, M., & Mack, J. 1998, AJ, 116, 68, doi: 10.1086/300407

Carroll, J. A. 1933, MNRAS, 93, 478, doi: 10.1093/mnras/93.7.478

Carroll, J. A., & Ingram, L. J. 1933, MNRAS, 93, 508, doi: 10.1093/mnras/93.7.508

Charbonnel, C., & Lagarde, N. 2010, A&A, 522, A10, doi: 10.1051/0004-6361/201014432

Charbonnel, C., & Primas, F. 2005, A&A, 442, 961, doi: 10.1051/0004-6361:20042491

Chieffi, A., & Limongi, M. 2013, ApJ, 764, 21, doi: 10.1088/0004-637X/764/1/21

Choi, J., Dotter, A., Conroy, C., et al. 2016, ApJ, 823, 102, doi: 10.3847/0004-637X/823/2/102

Claudi, R., Benatti, S., Carleo, I., et al. 2017, European Physical Journal Plus, 132, 364, doi: 10.1140/epjp/i2017-11647-9

Collins, George W., I., & Truax, R. J. 1995a, ApJ, 439, 860, doi: 10.1086/175225

—. 1995b, ApJ, 439, 860, doi: 10.1086/175225

Cosentino, R., Lovis, C., Pepe, F., et al. 2014, in Society of Photo-Optical Instrumentation Engineers (SPIE) Conference Series, Vol. 9147, Ground-based and Airborne Instrumentation for Astronomy V, ed. S. K. Ramsay, I. S. McLean, & H. Takami, 91478C, doi: 10.1117/12.2055813

Cretignier, M., Francfort, J., Dumusque, X., Allart, R., & Pepe, F. 2020, A&A, 640, A42, doi: 10.1051/0004-6361/202037722

Cunha, K., Smith, V. V., Hasselquist, S., et al. 2017, ApJ, 844, 145, doi: 10.3847/1538-4357/aa7beb

Currie, T., Hernandez, J., Irwin, J., et al. 2010, ApJS, 186, 191, doi: 10.1088/0067-0049/186/2/191

Cyburt, R. H., Fields, B. D., & Olive, K. A. 2008, J. Cosmology Astropart. Phys., 2008, 012, doi: 10.1088/1475-7516/2008/11/012

Dalessandro, E., Varri, A. L., Tiongco, M., et al. 2021, ApJ, 909, 90, doi: 10.3847/1538-4357/abda43

Danks, A. C., & Lambert, D. L. 1985, A&A, 148, 293

Davies, B., & Dessart, L. 2019, MNRAS, 483, 887, doi: 10.1093/mnras/sty3138

de Burgos, A., Simon-Díaz, S., Lennon, D. J., et al. 2020, A&A, 643, A116, doi: 10.1051/0004-6361/202039019

Díaz, C. G., González, J. F., Levato, H., & Grosso, M. 2011, A&A, 531, A143, doi: 10.1051/0004-6361/201016386

D'Orazi, V., Gratton, R. G., Pancino, E., et al. 2011, A&A, 534, A29, doi: 10.1051/0004-6361/201117630

Dotter, A., Chaboyer, B., Jevremović, D., et al. 2008, ApJS, 178, 89, doi: 10.1086/589654

Dravins, D., Lindegren, L., & Torkelsson, U. 1990, A&A, 237, 137

Dufton, P. L., Fitzsimmons, A., & Rolleston, W. R. J. 1994, A&A, 286, 449

Dunkley, J., Komatsu, E., Nolta, M. R., et al. 2009, ApJS, 180, 306, doi: 10.1088/0067-0049/180/2/306

Eggen, O. J. 1971, PASP, 83, 271, doi: 10.1086/129120

Ekström, S., Georgy, C., Eggenberger, P., et al. 2012, A&A, 537, A146, doi: 10.1051/0004-6361/201117751

Elmegreen, B. G., & Hunter, D. A. 2010, ApJ, 712, 604, doi: 10.1088/0004-637X/712/1/604

Fabbian, D., Asplund, M., Carlsson, M., & Kiselman, D. 2006, A&A, 458, 899, doi: 10.1051/0004-6361:20065763

Fanelli, C., Origlia, L., Oliva, E., et al. 2022, A&A, 660, A7, doi: 10.1051/0004-6361/202142492

—. 2021, A&A, 645, A19, doi: 10.1051/0004-6361/202039397

Frischknecht, U., Hirschi, R., Meynet, G., et al. 2010, A&A, 522, A39, doi: 10.1051/0004-6361/201014340

Fulbright, J. P., McWilliam, A., & Rich, R. M. 2006, ApJ, 636, 821, doi: 10.1086/498205

Gahm, G. F., & Hultqvist, L. 1976, A&A, 50, 153

Gaia Collaboration, Prusti, T., de Bruijne, J. H. J., et al. 2016, A&A, 595, A1, doi: 10.1051/0004-6361/201629272

Gaia Collaboration, Brown, A. G. A., Vallenari, A., et al. 2021, A&A, 649, A1, doi: 10.1051/0004-6361/202039657

Gazak, J. Z., Davies, B., Kudritzki, R., Bergemann, M., & Plez, B. 2014, ApJ, 788, 58, doi: 10.1088/0004-637X/788/1/58

Genovali, K., Lemasle, B., Bono, G., et al. 2014, A&A, 566, A37, doi: 10.1051/0004-6361/201323198

Georgy, C., Ekström, S., Granada, A., et al. 2013, A&A, 553, A24, doi: 10.1051/0004-6361/201220558

Golob, A., Sawicki, M., Goulding, A. D., & Coupon, J. 2021, MNRAS, 503, 4136, doi: 10.1093/mnras/stab719

Gray, D. F. 1976, The observation and analysis of stellar photospheres

—. 1981, ApJ, 245, 992, doi: 10.1086/158876

Grevesse, N., & Sauval, A. J. 1998, Space Sci. Rev., 85, 161, doi: 10.1023/A:1005161325181

Grisoni, V., Matteucci, F., Romano, D., & Fu, X. 2019, MNRAS, 489, 3539, doi: `10.1093/mnras/stz2428`

Grisoni, V., Romano, D., Spitoni, E., et al. 2020, MNRAS, doi: `10.1093/mnras/staa2316`

Groh, J. H., Meynet, G., Georgy, C., & Ekström, S. 2013, A&A, 558, A131, doi: `10.1051/0004-6361/201321906`

Gustafsson, B., Edvardsson, B., Eriksson, K., et al. 2008, A&A, 486, 951, doi: `10.1051/0004-6361:200809724`

Hasselquist, S., Shetrone, M., Cunha, K., et al. 2016, ApJ, 833, 81, doi: `10.3847/1538-4357/833/1/81`

Hayden, M. R., Holtzman, J. A., Bovy, J., et al. 2014, AJ, 147, 116, doi: `10.1088/0004-6256/147/5/116`

Hinkle, K., & Wallace, L. 2005, in Astronomical Society of the Pacific Conference Series, Vol. 336, Cosmic Abundances as Records of Stellar Evolution and Nucleosynthesis, ed. I. Barnes, Thomas G. & F. N. Bash, 321

Hinkle, K., Wallace, L., Harmer, D., Ayres, T., & Valenti, J. 2000, in IAU Joint Discussion, Vol. 24, 26

Hinkle, K. H., & Lambert, D. L. 1975, MNRAS, 170, 447, doi: `10.1093/mnras/170.3.447`

Holtzman, J. A., Shetrone, M., Johnson, J. A., et al. 2015, AJ, 150, 148, doi: `10.1088/0004-6256/150/5/148`

Humphreys, R. M., & Davidson, K. 1979, ApJ, 232, 409, doi: `10.1086/157301`

Humphreys, R. M., Davidson, K., Ruch, G., & Wallerstein, G. 2005, AJ, 129, 492, doi: `10.1086/426565`

Jönsson, H., Ryde, N., Harper, G. M., et al. 2014, A&A, 564, A122, doi: `10.1051/0004-6361/201423597`

Kondo, S., Fukue, K., Matsunaga, N., et al. 2019, ApJ, 875, 129, doi: `10.3847/1538-4357/ab0ec4`

Kovtyukh, V., Lemasle, B., Bono, G., et al. 2022, MNRAS, 510, 1894, doi: `10.1093/mnras/stab3530`

Lada, C. J., & Lada, E. A. 2003, ARA&A, 41, 57, doi: `10.1146/annurev.astro.41.011802.094844`

Levesque, E. M. 2010, New Astron. Rev., 54, 1, doi: `10.1016/j.newar.2009.10.002`

Levesque, E. M., Massey, P., Olsen, K. A. G., et al. 2005, ApJ, 628, 973, doi: 10.1086/430901

Lind, K., Asplund, M., & Barklem, P. S. 2009, A&A, 503, 541, doi: 10.1051/0004-6361/200912221

Lind, K., Asplund, M., Barklem, P. S., & Belyaev, A. K. 2011, A&A, 528, A103, doi: 10.1051/0004-6361/201016095

Livingston, W., & Wallace, L. 1991, An atlas of the solar spectrum in the infrared from 1850 to 9000 cm-1 (1.1 to 5.4 micrometer)

Lyubimkov, L. S., Lambert, D. L., Kaminsky, B. M., et al. 2012, MNRAS, 427, 11, doi: 10.1111/j.1365-2966.2012.21617.x

M. Kovalev, S. Brinkmann, M. Bergemann, & MPIA IT-department. 2018, NLTE MPIA web server, [Online]. Available: http://nlte.mpia.de Max Planck Institute for Astronomy, Heidelberg.

Maas, Z. G., Pilachowski, C. A., & Cescutti, G. 2017, ApJ, 841, 108, doi: 10.3847/1538-4357/aa7050

Majewski, S. R., Skrutskie, M. F., Schiavon, R. P., et al. 2007, in American Astronomical Society Meeting Abstracts, Vol. 211, 132.08

Mashonkina, L. I., Shimanskiĭ, V. V., & Sakhibullin, N. A. 2000, Astronomy Reports, 44, 790, doi: 10.1134/1.1327637

Matsunaga, N., Taniguchi, D., Jian, M., et al. 2020, ApJS, 246, 10, doi: 10.3847/1538-4365/ab5c25

Mauron, N., & Josselin, E. 2011, A&A, 526, A156, doi: 10.1051/0004-6361/201013993

McWilliam, A., & Rich, R. M. 1994, ApJS, 91, 749, doi: 10.1086/191954

Meléndez, J., & Barbuy, B. 1999, ApJS, 124, 527, doi: 10.1086/313261

Mikolaitis, Š., Hill, V., Recio-Blanco, A., et al. 2014, A&A, 572, A33, doi: 10.1051/0004-6361/201424093

Mikolaitis, Š., Drazdauskas, A., Minkevičiūtė, R., et al. 2019, A&A, 628, A49, doi: 10.1051/0004-6361/201835004

Moriya, T., Tominaga, N., Blinnikov, S. I., Baklanov, P. V., & Sorokina, E. I. 2011, MNRAS, 415, 199, doi: 10.1111/j.1365-2966.2011.18689.x

Mucciarelli, A. 2011, A&A, 528, A44, doi: 10.1051/0004-6361/201015814

Navarro, J. F., Helmi, A., & Freeman, K. C. 2004, ApJ, 601, L43, doi: 10.1086/381751

Negueruela, I., Alonso-Santiago, J., Tabernero, H. M., et al. 2020, Mem. Soc. Astron. Italiana, 91, 114

Nissen, P. E. 2004, in Origin and Evolution of the Elements, ed. A. McWilliam & M. Rauch, 154. https://arxiv.org/abs/astro-ph/0310326

Nordlander, T., & Lind, K. 2017, A&A, 607, A75, doi: 10.1051/0004-6361/201730427

Oliva, E., Biliotti, V., Baffa, C., et al. 2012a, in Society of Photo-Optical Instrumentation Engineers (SPIE) Conference Series, Vol. 8453, Proc. SPIE, 84532T, doi: 10.1117/12.925293

Oliva, E., Sanna, N., Rainer, M., et al. 2018, in Society of Photo-Optical Instrumentation Engineers (SPIE) Conference Series, Vol. 10702, Proc. SPIE, 1070274, doi: 10.1117/12.2309927

Oliva, E., Origlia, L., Maiolino, R., et al. 2012b, in Society of Photo-Optical Instrumentation Engineers (SPIE) Conference Series, Vol. 8446, Proc. SPIE, 84463T, doi: 10.1117/12.925274

Origlia, L., Oliva, E., Baffa, C., et al. 2014, in Society of Photo-Optical Instrumentation Engineers (SPIE) Conference Series, Vol. 9147, Ground-based and Airborne Instrumentation for Astronomy V, 91471E, doi: 10.1117/12.2054743

Origlia, L., Dalessandro, E., Sanna, N., et al. 2019, A&A, 629, A117, doi: 10.1051/0004-6361/201936283

Osorio, Y., Allende Prieto, C., Hubeny, I., Mészáros, S., & Shetrone, M. 2020, A&A, 637, A80, doi: 10.1051/0004-6361/201937054

Overbeek, J. C., Friel, E. D., & Jacobson, H. R. 2016, ApJ, 824, 75, doi: 10.3847/0004-637X/824/2/75

Plez, B. 2012, Turbospectrum: Code for spectral synthesis. http://ascl.net/1205.004

Portegies Zwart, S. F., McMillan, S. L. W., & Gieles, M. 2010, ARA&A, 48, 431, doi: 10.1146/annurev-astro-081309-130834

Rainer, M., Harutyunyan, A., Carleo, I., et al. 2018, in Society of Photo-Optical Instrumentation Engineers (SPIE) Conference Series, Vol. 10702, Proc. SPIE, 1070266, doi: 10.1117/12.2312130

Ramírez, I., & Allende Prieto, C. 2011, ApJ, 743, 135, doi: 10.1088/0004-637X/743/2/135

Randich, S. 2010, in Light Elements in the Universe, ed. C. Charbonnel, M. Tosi,

F. Primas, & C. Chiappini, Vol. 268, 275–283, doi: `10.1017/S1743921310004242`

Reddy, B. E., Lambert, D. L., & Allende Prieto, C. 2006, MNRAS, 367, 1329, doi: `10.1111/j.1365-2966.2006.10148.x`

Reddy, B. E., Tomkin, J., Lambert, D. L., & Allende Prieto, C. 2003, MNRAS, 340, 304, doi: `10.1046/j.1365-8711.2003.06305.x`

Reiners, A., & Schmitt, J. H. M. M. 2002, A&A, 384, 155, doi: `10.1051/0004-6361:20011801`

Rich, R. M., Ryde, N., Thorsbro, B., et al. 2017, AJ, 154, 239, doi: `10.3847/1538-3881/aa970a`

Royer, F., Gerbaldi, M., Faraggiana, R., & Gómez, A. E. 2002, A&A, 381, 105, doi: `10.1051/0004-6361:20011422`

Ryabchikova, T., & Pakhomov, Y. 2015, Baltic Astronomy, 24, 453, doi: `10.1515/astro-2017-0249`

Ryde, N., Edvardsson, B., Gustafsson, B., et al. 2009, A&A, 496, 701, doi: `10.1051/0004-6361/200811070`

Ryde, N., Fritz, T. K., Rich, R. M., et al. 2016, ApJ, 831, 40, doi: `10.3847/0004-637X/831/1/40`

Sackmann, I. J., & Boothroyd, A. I. 1992, ApJ, 392, L71, doi: `10.1086/186428`

Saito, R. K., Hempel, M., Minniti, D., et al. 2012, A&A, 537, A107, doi: `10.1051/0004-6361/201118407`

Schlafly, E. F., & Finkbeiner, D. P. 2011, ApJ, 737, 103, doi: `10.1088/0004-637X/737/2/103`

Schlegel, D. J., Finkbeiner, D. P., & Davis, M. 1998, ApJ, 500, 525, doi: `10.1086/305772`

Shcherbakov, A. G., Shcherbakova, Z. A., Tuominen, I., & Jetsu, L. 1996, A&A, 309, 655

Shetrone, M., Bizyaev, D., Lawler, J. E., et al. 2015, ApJS, 221, 24, doi: `10.1088/0067-0049/221/2/24`

Siess, L. 2010, A&A, 512, A10, doi: `10.1051/0004-6361/200913556`

Skrutskie, M. F., Cutri, R. M., Stiening, R., et al. 2006, AJ, 131, 1163, doi: `10.1086/498708`

Smartt, S. J. 2015, Publ. Astron. Soc. Australia, 32, e016, doi: `10.1017/pasa.2015.17`

Smith, N., Hinkle, K. H., & Ryde, N. 2009, AJ, 137, 3558, doi: `10.1088/0004-6256/137/3/3558`

Smith, V. V., Cunha, K., Shetrone, M. D., et al. 2013, ApJ, 765, 16, doi: `10.1088/0004-637X/765/1/16`

Spite, M., & Spite, F. 1982, Nature, 297, 483, doi: `10.1038/297483a0`

Strom, S. E., Wolff, S. C., & Dror, D. H. A. 2005, AJ, 129, 809, doi: `10.1086/426748`

Takeda, Y. 1992, A&A, 253, 487

Takeda, Y., Omiya, M., Harakawa, H., & Sato, B. 2016, PASJ, 68, 81, doi: `10.1093/pasj/psw071`

Takeda, Y., & Takada-Hidai, M. 2013, PASJ, 65, 65, doi: `10.1093/pasj/65.3.65`

Taylor, W., Cirasuolo, M., Afonso, J., et al. 2018, in Society of Photo-Optical Instrumentation Engineers (SPIE) Conference Series, Vol. 10702, Ground-based and Airborne Instrumentation for Astronomy VII, ed. C. J. Evans, L. Simard, & H. Takami, 107021G, doi: `10.1117/12.2313403`

Thorsbro, B., Ryde, N., Rich, R. M., et al. 2020, ApJ, 894, 26, doi: `10.3847/1538-4357/ab8226`

Tonry, J., & Davis, M. 1979, AJ, 84, 1511, doi: `10.1086/112569`

Tozzi, A., Oliva, E., Iuzzolino, M., et al. 2016, in Society of Photo-Optical Instrumentation Engineers (SPIE) Conference Series, Vol. 9908, Proc. SPIE, 99086C, doi: `10.1117/12.2231898`

Vasconcellos, E. C., de Carvalho, R. R., Gal, R. R., et al. 2011, AJ, 141, 189, doi: `10.1088/0004-6256/141/6/189`

Ventura, P., Carini, R., & D'Antona, F. 2011, MNRAS, 415, 3865, doi: `10.1111/j.1365-2966.2011.18997.x`

Ventura, P., & D'Antona, F. 2010, MNRAS, 402, L72, doi: `10.1111/j.1745-3933.2010.00805.x`

—. 2011, MNRAS, 410, 2760, doi: `10.1111/j.1365-2966.2010.17651.x`

Ventura, P., Di Criscienzo, M., Carini, R., & D'Antona, F. 2013, MNRAS, 431, 3642, doi: `10.1093/mnras/stt444`

Warren, P. R. 1973, MNRAS, 163, 337, doi: `10.1093/mnras/163.3.337`

Worley, C. C., Cottrell, P. L., Freeman, K. C., & Wylie-de Boer, E. C. 2009, MNRAS, 400, 1039, doi: `10.1111/j.1365-2966.2009.15520.x`

Zhang, H. W., Gehren, T., Butler, K., Shi, J. R., & Zhao, G. 2006, A&A, 457, 645,

doi: 10.1051/0004-6361:20064909

Zhang, J., Shi, J., Pan, K., Allende Prieto, C., & Liu, C. 2017, ApJ, 835, 90, doi: 10.3847/1538-4357/835/1/90

Quando ti vedo mi prostro davanti a te e alle tue parole,
vedendo la casa astrale della Vergine,
infatti verso il cielo è rivolto ogni tuo atto
Ipazia sacra, bellezza delle parole,
astro incontaminato della sapiente cultura.

Pallada d'Alessandria, IV sec. d.C.